1969

Mössbauer Effect studies of ferroelectric phase transitions in the $PbZrO_3$ - $PbTiO_3$ - $BiFeO_3$ ternary system

James P. Canner

MOSSBAUER EFFECT STUDIES

OF

FERROELECTRIC PHASE TRANSITIONS

IN THE

$PbZrO_3$ - $PbTiO_3$ - $BiFeO_3$ TERNARY SYSTEM

by

JAMES PHILIP CANNER 1941

A DISSERTATION

Presented to the Faculty of the Graduate School of the

UNIVERSITY OF MISSOURI - ROLLA

In Partial Fulfillment of the Requirements for the Degree

DOCTOR OF PHILOSOPHY

IN

PHYSICS

1969

Robert Gerson per AGF
Advisor

W. J. James

Wayne E. Tefft

James Paul Wesley

John T. Park

Horace L. Davies

MOSSBAUER EFFECT STUDIES

OF

FERROELECTRIC PHASE TRANSITIONS

IN THE

$PbZrO_3$ - $PbTiO_3$ - $BiFeO_3$ TERNARY SYSTEM

An abstract of a dissertation

presented to

the Faculty of the Graduate School

University of Missouri - Rolla

In partial fulfillment of

the requirements for the degree

Doctor of Philosophy

---

by

James Philip Canner

May 1969

ABSTRACT

The Mossbauer Effect was used to measure the phase transitions in the following ferroelectric compounds:

$$95\%\ PbZr_{0.8}Ti_{0.2}O_3 - 5\%\ BiFeO_3$$

$$95\%\ PbZr_{0.7}Ti_{0.3}O_3 - 5\%\ BiFeO_3$$

and in the antiferroelectric compound:

$$95\%\ PbZrO_3 - 5\%\ BiFeO_3.$$

The parameters obtained were the area under the resonance peak, the isomer shift, and the electric quadrupole splitting, all as a function of temperature. The ionicity, electric field gradient, and Debye temperature were determined for room temperature.

The data are discussed in terms of the lattice vibration model of ferroelectrics and antiferroelectrics, and the structural phase transitions as recently defined for these compounds. The ionicity is determined and discussed in relation to crystal distortion and Curie temperature. The electric field gradient is related to the relative polarizations of the different samples. A discussion of the mixture of charge states in the A and the B ion sites of the perovskite structure, and the oxygen defect problem in these compounds, completes the discussion.

ACKNOWLEDGMENTS

The author wishes to express his appreciation to Dr. R. Gerson, Professor of Physics, for the suggestion of the problem, patient guidance, and helpful advice in the preparation of this dissertation. He would also like to thank Dr. W. James, Professor of Chemistry, for many helpful discussions, Drs. C. Michel and J. Moreau for many discussions about the crystal structure and phase transitions, Dr. C. M. Yagnik for discussions on the Mossbauer Effect and assistance in obtaining data, and W. Denno, T. Willis, and J. Hemmann for assistance in developing the velocity drive system.

The author would like to thank the Nuclear Reactor Facility for the loan of the data tape punch, and the UMR Computer Center for computer time and assistance in transferring the data from tapes to cards.

The author is indebted to the Atomic Energy Commission and the National Aeronautics and Space Administration for financial support in the past five years.

The author would like to dedicate this dissertation to his parents, Mr. and Mrs. Ronald M. Canner.

TABLE OF CONTENTS

LIST OF TABLES

LIST OF FIGURES

Page

Page

I. INTRODUCTION

The current theory of ferroelectricity requires an anomalous lowering of the frequency of certain lattice modes near the phase change from the paraelectric to the ferroelectric region of crystal symmetry. The experimental determination of these lattice modes and their behavior with temperature usually requires large single crystals for neutron scattering or infrared measurements. Significant data of this sort are available only for a few ferroelectrics such as barium titanate ($BaTiO_3$), and strontium titanate ($SrTiO_3$).

It has been suggested that the Mossbauer effect should be able to determine the presence of temperature dependent lattice modes in ferroelectrics by displaying a decreased recoilless absorption at the Curie temperature due to the lattice mode softening at the Brillouin zone center [k = (000)]. The suggested effect has been observed in barium titanate and a few other compounds with varying success. It was also suggested that antiferroelectrics should resemble ferroelectrics in displaying decreased recoilless absorption at the Curie temperature, but that the decrease could be much larger in magnitude. The lattice mode should soften at the edge of the Brillouin zone, but may be quite low for the whole zone.

The object of this experiment was to study the Mossbauer effect in an antiferroelectric and in related ferroelectrics.

A set of three compounds of high lead zirconate content in the lead zirconate-lead titanate-bismuth ferrate ternary system were chosen to compare the ferroelectric rhombohedral-cubic phase transition and the antiferroelectric orthorhombic-cubic phase transition,using Mossbauer spectroscopy as a diagnostic tool.

The literature survey discusses the basics of the Mossbauer effect, ferroelectricity, antiferroelectricity, the perovskite structure, the above ternary system, and the Mossbauer effect in ferroelectrics.

The experimental section discusses the parameters obtained in Mossbauer effect studies and the apparatus needed to perform the experiment. The data are presented and discussed with conclusions in the final section.

II. LITERATURE SURVEY

A. THE MOSSBAUER EFFECT.

Rudolf Mossbauer[1,2] discovered in 1958 that the resonance absorption in iridium 191 apparently increased at low temperatures. This was contrary to the expectation that the resonance overlap should decrease as the thermal broadening of the linewidth decreased. Mossbauer's explanation, based on the results of Lamb[3] for neutron capture in crystals, was that the gamma rays were being resonantly absorbed and emitted without recoil by the nucleus. This process allows the energy of the emitted gamma ray to overlap the absorption energy level without the need for thermal broadening or large Doppler shifts.[4]

The Nobel prize in Physics was awarded to Mossbauer in 1962 for this discovery, which vastly improved the state of the art in the nuclear resonance absorption of gamma rays. The effect is capable of resolving energy to one part in 10^{11}, and measures hyperfine interactions of the nuclear spin to an accuracy of 10^{-6} electron volts (ev), using gamma rays of energies between 10 and 100 kev. The correct explanation of the effect requires quantum theory, but semi-classical models are often used to explain the basic details of the effect. Lipkin[5] has derived a sum rule for the interaction of a gamma ray with a quantized crystal lattice:

$$\sum_{n_f} [E(n_f) - E(n_i)].P(n_f,n_i) = \frac{\hbar^2 k^2}{2M} = R \qquad (1)$$

where n_f, n_i represent the final and initial states of the

lattice,

$E(n)$ is the energy of the nth state,

$P(n_f,n_i)$ is the probability of transition between the states,

$\hbar$ is Planck's constant divided by 2π,

k is the wave vector for the gamma ray,

M is the mass of the absorbing nucleus,

R is the recoil energy imparted to the lattice.

Since no terms for transitionless absorption appear in the sum, the sum of the probabilities on the left side of the equation can be less then unity. The difference from unity determines the probability for a recoilless process. The total probability must be unity. Recoilless emission, in general, can be achieved if the gamma ray energy lies in a range where the recoil energy, R, is comparable to the lattice vibration energy levels.

The conservation of energy requirement is satisfied by the above rule, but it is not immediately apparent how the conservation of momentum occurs. It is found that the recoil momentum is capable of being transferred to the whole lattice, rather than being taken up by a single atom. The probability of such a transfer is given by:

$$P(n_f,n_i) = [\langle n_f|\exp(-i\vec{K}\cdot\vec{X})|n_i\rangle]^2 \qquad (2)$$

where X is the displacement of the atom. This expression can be evaluated to give the Lamb - Mossbauer factor, f, given as:

$$f = e^{-2W}. \tag{3}$$

Here $$W = k^2\langle x^2\rangle \tag{4}$$

and is the Debye-Waller factor, common in X-ray diffraction. A more elaborate evaluation, using the Debye model,[6] gives:

$$W = \frac{3\ R}{k_B\ \theta_D}\left(\frac{1}{4} + \left(\frac{T}{\theta_D}\right)^2\ \Phi\ \left(\frac{T}{\theta_D}\right)\right) \tag{5}$$

where k_B is Boltzmann's constant,

θ_D is the Debye temperature,

T is the absolute temperature,

Φ is the Debye integral related to the Riemann Zeta functions.[7] From this relationship, we can see that the recoil free fraction, f, will increase with θ_D. The variation of f with temperature for different Debye temperatures is given in figure 1.

The linewidth of the resonance line is unaffected by usual broadenings and is usually quite close to the natural linewidth. The Heisenberg uncertainty principle can be used to find the natural linewidth as follows:

$$\Gamma = \frac{\hbar}{\tau} \tag{6}$$

where Γ is the full linewidth at half maximum,

τ is the mean life of the excited state of the nucleus.

The mean life is related to the half life by:

$$\tau = \frac{t_{\frac{1}{2}}}{\ln 2} \tag{7}$$

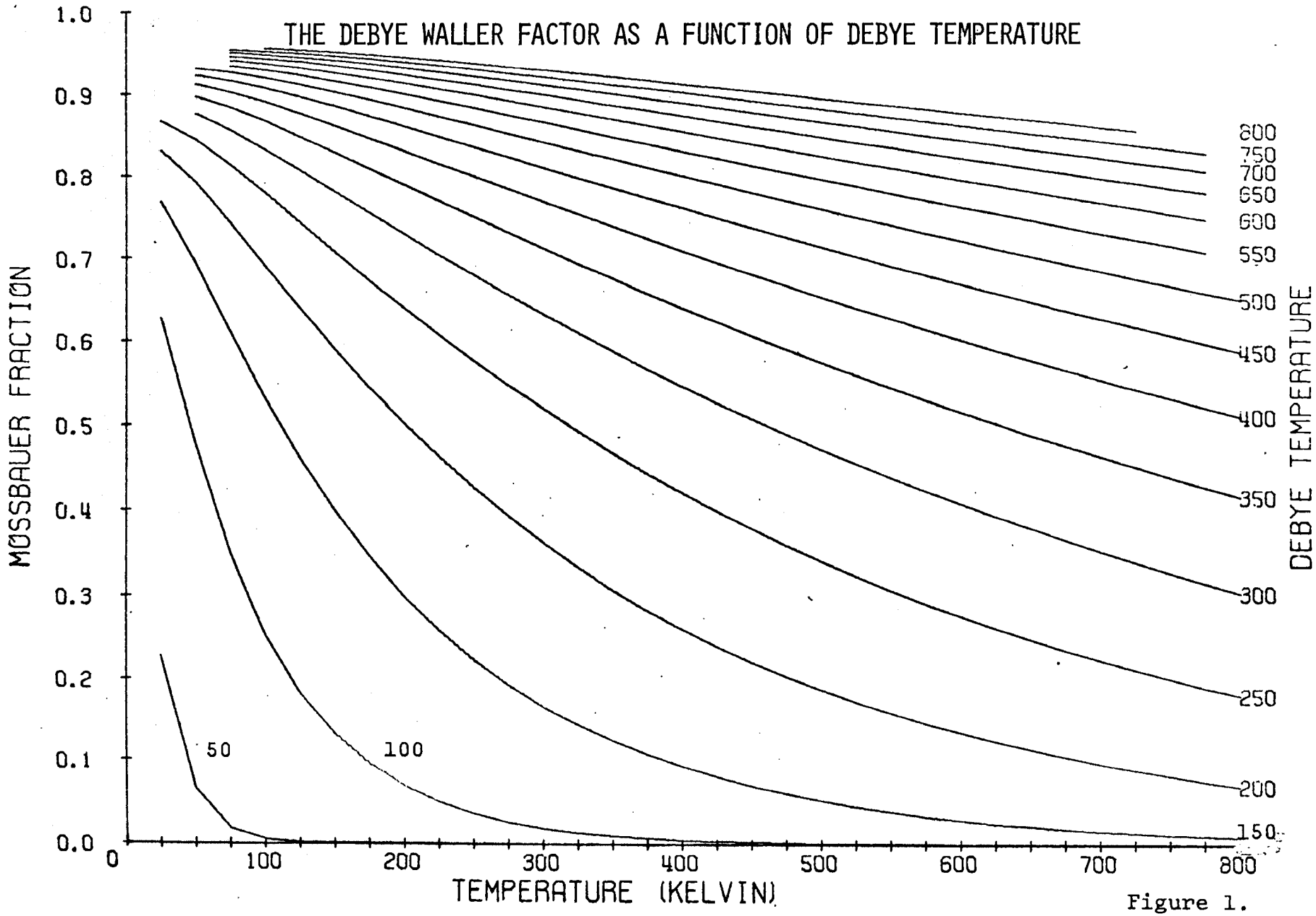
THE DEBYE WALLER FACTOR AS A FUNCTION OF DEBYE TEMPERATURE
MOSSBAUER FRACTION
1.0
0.9
0.8
0.7
0.6
0.5
0.4
0.3
0.2
0.1
0.0
0
100
200
300
400
500
600
700
800
TEMPERATURE (KELVIN)
DEBYE TEMPERATURE
800
750
700
650
600
550
500
450
400
350
300
250
200
150
50
100

Figure 1.

The cross section for the transition is given by

$$\sigma_o = 2\pi\lambda\!\!\!^{-2} \frac{(2I_B+1)}{(2I_A+1)} \frac{\Gamma_\gamma}{\Gamma} \tag{8}$$

where $\lambda\!\!\!^{-} = \frac{\hbar c}{E}$, is the wavelength of the radiation,

σ_o is the cross section,

I_B, I_A are the nuclear spins for the excited and ground states,

Γ_γ is the linewidth for gamma ray absorption, and

Γ is the linewidth for the total transition.

For resonance absorption, the cross-section is multiplied by the line shape function, given by the Breit-Wigner or Lorentzian form:

$$\sigma_M = f\sigma_o \frac{1}{1+\left(\frac{E - E_o}{\Gamma/2}\right)^2} \tag{9}$$

where E_o is the transition energy,

σ_M is the Mossbauer cross section.

The theory is developed by Abragam[8] (in French), Boyle and Hall,[9] and Danon.[10]

The Mossbauer effect gives us three basic parameters: the energy E, linewidth Γ, and intensity f. The energy level resonant with the γ-ray of energy E_o can be shifted and/or split into several different levels due to hyperfine interactions, and relativistic effects. The hyperfine interactions will be discussed later. The relativistic effects include the gravitational red shift of the

γ-ray,[11] and the thermal motion of the atoms (considered as a second order Doppler shift).

The linewidth, besides being a measure of the lifetime of the nuclear states, is affected by relaxation effects resulting from phase transitions, spin exchange and atomic motion. These cause a broadening of the linewidth. The linewidth has been narrowed by using coincidence Mossbauer spectroscopy.[12] The apparent life time of the excited state is increased by discriminating against the gamma rays emitted within the first few lifetimes.

The intensity of absorption, or the Mossbauer fraction f, has been shown to be dependent on the vibrational energy of the lattice through the Debye-Waller Factor. It can be affected by the lattice symmetry.

Gonser[13] has reviewed experimental examples of many of these effects observed in solid state materials. The interactions that apply to the interpretation of the results of this experiment and to the consideration of ferroelectricity, will be discussed later.

B. FERROELECTRICITY

A ferroelectric crystal may be defined as having reversible electric polarization. This can be demonstrated by generating hysteresis loops, using a Sawyer-Tower Circuit.[14] Since the polarization is due to position of ionic charges within the crystal lattice, symmetry conditions can be imposed for ferroelectricity. The crystal must be

polar and noncentrosymmetric to show a dipole moment along a specific direction* but the presence of a moment does not imply reversibility.

Ferroelectrics are characterized by a large dielectric constant, which becomes anomalously high near a phase transition between states having different polarizations. The transition has been called the "polarization catastrophe", and is the result of the elastic forces in the crystal being balanced out by the polarization forces, so that the crystal can distort appreciably under the influence of a very small electric field. The Clausius-Mossotti equation gives a simplified reason for this occurrence. The equation is:[15]

$$\varepsilon = \frac{1+\frac{8\pi}{3}\Sigma N_i\alpha_i}{1-\frac{4\pi}{3}\Sigma N_i\alpha_i} \qquad (10)$$

Where ε is the dielectric constant, and

N_i is the number of ions having polarizability α_i.

When the denominator becomes zero, ε becomes very large, while the lattice becomes "soft" and a phase transition takes place. If the denominator is assumed to behave linearly with temperature above the phase transition, the

---

* Of the 32 point groups, 21 are noncentrosymmetric. Only 10 of the 20 can be shown to be polar, and therefore capable of being ferroelectric.

dielectric constant behaves according to the Curie-Weiss law:

$$\varepsilon = \frac{C}{T-T_c} \tag{11}$$

where T_c is the Curie temperature,

C is a proportionality constant.

Devonshire[16,17,18] has developed a phenomenological thermodynamic theory for ferroelectrics which uses the Maxwell relations for the Gibbs free energy function, as defined by:

$$dG = -SdT - xdX + EdP \tag{12}$$

where S is the entropy,

T is the temperature,

x is the strain,

X is the stress,

E is the electric field,

P is the polarization.

The free energy function G is expanded in terms of the polarization as follows:

$$G = G_o + \frac{1}{2}\beta P^2 + \frac{1}{4}\gamma P^4 + \frac{1}{6}\delta P^6 + \cdots \tag{13}$$

where G_o is the non-ferroelectric free energy,

β, γ, δ are constants to be determined from the experimental data using the Maxwell relations. The first constant, β, gives the temperature behavior of the dielectric constant;

$$\beta = C' (T - T_o) \tag{14}$$

where C' is a proportionality constant,

T_o is the transition temperature.

For a first order transition, the second constant, γ, must be negative to allow the equality of G across the phase boundary for non-zero polarization. The γ is positive for second order phase transitions (the third constant becomes negligible) for which the polarization in both phases goes continuously to zero at the transition temperature.

Early attempts at explaining ferroelectricity were limited to interpretation of dielectric data in terms of Devonshire's constants. A more fundamental approach, proposed simultaneously by Cochran[19] and Anderson,[20] was based on consideration of the temperature dependence of the lattice modes. The importance of the mode relationships to the dielectric constant is shown by the Lyddane-Sachs-Teller (LST) equation[21]:

$$\frac{\omega_T^2}{\omega_L^2} = \frac{\varepsilon(\infty)}{\varepsilon(0)} \tag{15}$$

where ω_T^2 is the frequency of the transverse optic lattice mode,

ω_L^2 is the frequency of the longitudinal optic lattice mode,

$\varepsilon(\infty)$ is the high frequency dielectric constant, and

$\varepsilon(0)$ is the static dielectric constant.

It was demonstrated using simplified lattice models that the transverse mode could give the required temperature dependence to the dielectric constant, $\varepsilon(0)$.

Barker[22] gives a derivation for the mode frequencies of a simple diatomic cubic lattice in which the Z-axis becomes a preferred axis. The acoustic modes are not considered because they have no effect upon the polarization of the lattice. The frequencies of the long wavelength, k = 0, modes with zero applied electric field are:

$$\omega_T^2 = \frac{1}{\mu}\left[2A + 4B - \frac{4\pi\frac{e_1^2}{3v}}{1 - 4\pi\alpha/3v}\right] \tag{16}$$

$$\omega_L^2 = \frac{1}{\mu}\left[2A + 4B + \frac{8\pi\frac{e_1^2}{3v}}{1 + 8\pi\alpha/3v}\right] \tag{17}$$

where μ is the reduced mass ($\mu = m_1 m_2 / (m_1 + m_2)$),

A, B are the nearest neighbor inter-ionic potentials along z and perpendicular to z, respectively,

e_1 is the electronic charge on ion 1, $e_2 = -e_1$,

α is the polarizability of the ions,

v is the volume of the cell.

The local field and polarization for the two cases are shown in figure 2. In the longitudinal mode, no cancellation of the local fields with the inter-ionic forces is possible. However, in the transverse mode, the last term may cancel the first two terms to give zero frequency, causing the lattice to become unstable and to seek a stable lower

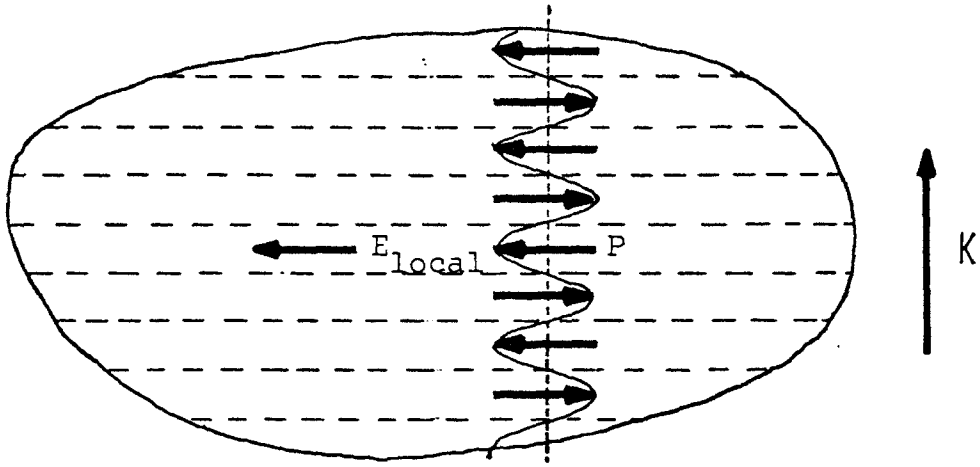

TRANSVERSE OPTICAL PHONONS: $E_{local} = \frac{4\pi}{3} P$

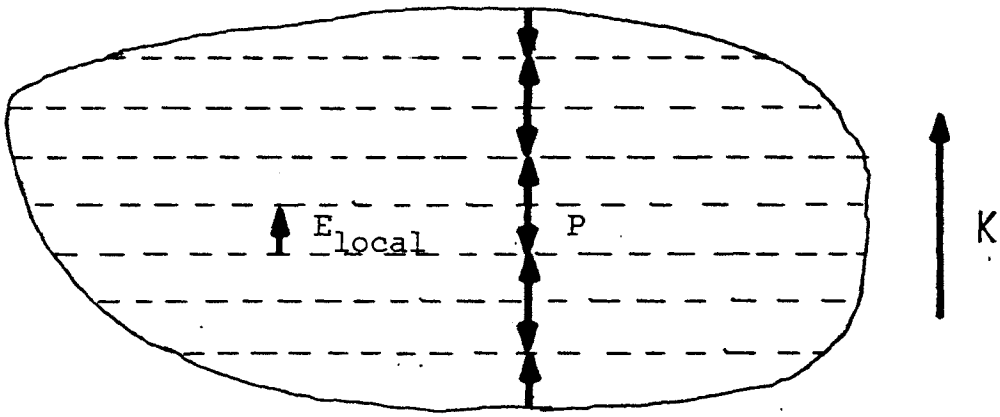

LONGITUDINAL OPTICAL PHONONS: $E_{local} = (-4\pi + \frac{4\pi}{3})P$

$= -\frac{8\pi}{3} P$

Figure 2. THE LOCAL ELECTRIC FIELDS DUE TO TRANSVERSE AND LONGITUDINAL OPTICAL PHONONS. The local electric field (long range interaction) tends to assist the lattice distortion associated with the transverse optical phonon, but tends to resist the distortion associated with the longitudinal optical phonon. The horizontal dashed lines depict the wave nodes.

symmetry state. When this happens, it is possible to give the temperature dependence near the instability by:

$$\omega_T^2 = C'' (T - T_o)^{\frac{1}{2}} \tag{18}$$

which leads to the Curie-Weiss law (11) for the dielectric constant, through the application of the LST relation (15). The last term in (16) varies with temperature because the cell volume is temperature dependent. As the temperature decreased, the volume decreases, until the term is large enough to balance the short range inter-ionic forces, A and B. The resulting phase transition is then studied using a power series expansion of G in terms of the polarization, P. The success of Devonshire's model for macroscopic phenomena is carried over into this theory.

The simplified microscopic model given above has been expanded to give a more exact explanation of ferroelectricity. Many attempts have been made since Ginzburg[23,24] first made his calculations of optical frequencies required to explain the high dielectric constant at the ferroelectric phase transition in 1949. Cochran[19] and Anderson[20] made various approximations of the atomic potentials to demonstrate the temperature dependence of the transverse optic modes. Vaks, Galitskii and Larkin[26] applied a self-consistent field method to calculate the damping of collective excitations near a phase transition. Vaks[27] continued this effort, using a much improved free energy expansion derived by Kwok and

Miller.[28] Cowley[29,30] has developed a theory of lattice dynamics using thermodynamical Green's functions to calculate the effects of anharmonicity on the lattice. Silverman[31] used an augmented Hamiltonian to balance out the majority of the anharmonic effects, so that perturbation theory could be used to obtain the lattice vibrations. Doniach[32] outlined a variational approach to find the free energy of a ferroelectric lattice. These attempts have not been too successful because of the large number of parameters to be considered. A recent attempt to reduce the number of parameters was made by Lines,[33,34,35] using a cluster model to approximate the surroundings of ions beyond the nearest neighbor sites. A self-consistent result was obtained, which was applied to lithium tantalate ($LiTaO_3$).

Other models have been proposed, including a tunneling model by Brout et al.,[36] which suggests that above the transition temperature the polar ion is able to tunnel between the wells of the multiple-well potential. This suggests the possibility of psuedo-Jahn-Teller[37] effect as an alternative explanation of ferroelectricity. This effect, which induces an asymmetry in the lattice due to unfilled electronic shell configurations, has been suggested to account for the electron-phonon interaction resulting from the partially covalent bonding that exists in ferroelectrics. The lattice mode theories assume ionic bonding alone. This idea was proposed by Fridkin[38] to complete the theory for the semiconducting ferroelectric SbSI. Sinha and Sinha[39]

proposed the Jahn-Teller effect[37] to explain the existence of the multiple well potential in $BaTiO_3$. This was developed further by Shukla and Sinha[40] to include the electron-phonon interaction. A similar idea was proposed by Bersucker.[41] Jones[42] discussed some of the qualitative effects on the dielectric constant, using a Jahn-Teller potential well. Birman[43] discussed the possibility of the effect from a group-theoretical viewpoint in the proposed metallic ferroelectrics of Anderson and Blount,[44] as well as for conventional ferroelectrics that are dielectrics. Recent work by Yamada et al.[45] at the phase transition of $BaTiO_3$ suggests that the observed fluctuations can be explained equally well using the tunneling model or an overdamped phonon model such as the anharmonic models of Cowley.[30]

Group theoretical methods have been used to define the possible ferroelectric phase transitions[25] that can occur for a particular symmetry, and to make predictions as to what modes will be temperature dependent and interesting in infrared and Raman spectra, and in neutron and x-ray inelastic scattering experiments. The basic work in this area was done by Haas,[46] Goldrich and Birman[47] and Cochran and Zia.[48] Experimental work has been done by Cowley[49] with $SrTiO_3$ and Barker and coworkers in $SrTiO_3$,[50,51] $BaTiO_3$,[50,51] $KTaO_3$[51] and $LiNbO_3$.[52] An excellent survey of the experimental work in the study of ferroelectric modes was given by Murzin,

Pasynkov and Solov'ev.[53]

C. ANTIFERROELECTRICITY

As the name may suggest (in a qualified analogy with antiferromagnetism), antiferroelectrics are ferroelectrics in which the polarization of one subcell is oppositely directed to the polarization of a second adjacent cell. This gives a net zero polarization under normal conditions. A model of two interlacing lattices was used by Kittel[54] to predict antiferroelectricity on the basis of the ferroelectric model in Devonshire's theory. Cross[55] modified this to include the three dimensional Lorentz correction introduced by Slater[56] for $BaTiO_3$, to explain the results obtained for $NaNbO_3$.

The lattice dynamical theories[19] differ only in the suggestion that the soft mode has wave numbers corresponding to the Brillouin zone boundary, $k = \frac{\pi}{a}$, instead of the zone center, $k = 0$. This is necessary to allow the adjacent cells to have opposite polarizations.

Silverman[57] has developed a harmonic model for antiferroelectricity which gives the frequency behaviour of the temperature dependent mode as:

$$\omega_T(k)^2 = K[T - (T_c + \Delta T_k)] \qquad (19)$$

where $T_c + \Delta T_k$ is the transition temperature for the k mode,

K is a proportionality constant.

In this model, Silverman assumed that the temperature dependent mode causing the cubic to antiferroelectric phase transition was the same one that explained the Curie law behavior, with the Curie point much less than the transition temperature. The ΔT_k is an increasing function of k for this particular mode.

Barker[22] developed a linear chain model without making the above assumption and found a temperature dependence near the zone boundary only. Cochran and Zia[48] have shown that at least two lattice modes are necessary to explain phase transitions of the perovskite antiferroelectrics. The temperature dependence of the dielectric constant can be explained using the second mode.

Miller and Kwok[58] have also developed a theory of microscopic free energy for antiferroelectrics. Haas[46] has discussed the symmetry changes in several antiferroelectric phase transitions. Cochran and Zia[48] examined the lattice modes which might be temperature dependent at the zone boundary in various multiple cell structures.

D. STRUCTURE OF PEROVSKITES

Of the class of displacive ferroelectrics, a large number belong to a structure family called perovskites. The prototype is the mineral perovskite having the composition $CaTiO_3$. The structure for the ABO_3 materials is based on the cubic form, with the large oxygen atoms in cubic close-packed configuration, the A atom in the 12

coordinated site, and the B atom in the 6 coordinated (or octahedral) site. The structure is depicted in figure 3 in two representations to show the symmetry of the A and B atoms. Goldschmidt[59] has given a criterion for atoms in an oxygen lattice:

$$R_a + R_x = \sqrt{2}t(R_b + R_x) \tag{20}$$

where R_a, R_x, R_b are the radii of A, O, and B ions.

For perovskites, t is between 0.8 and 1.0, as can be seen in table I.

The common ferroelectrics of this structure are $BaTiO_3$, $PbTiO_3$, $KTaO_3$, $KNbO_3$, and probably $LiNbO_3$ and $BiFeO_3$, which are highly distorted. The compound $NaNbO_3$ displays both ferroelectricity and antiferroelectricity at different temperatures. A well known antiferroelectric is $PbZrO_3$.

A number of interesting solid solutions exist having the same basic structure. These may be of the type $(A,A')BO_3$, $A(B,B')O_3$ or $(A,A')(B,B')O_3$. The first two cases are often only possible for specific proportions of the A or B ions, necessary to balance the charges in the structure. A few examples are Pb $(Fe_{\frac{1}{2}}Nb_{\frac{1}{2}})O_3$, $(K_{\frac{1}{2}}La_{\frac{1}{2}})TiO_3$, and Pb $(Fe_{2/3}W_{1/3})O_3$. If the A and A' (or the B and B') ions have the same formal valency, then continuous solid solutions are often possible, although they may or may not be ferroelectric in all compositional ranges, due to changing crystal symmetry. The most common solution of this type is the $PbTiO_3$-$PbZrO_3$ solid solution, which has four different

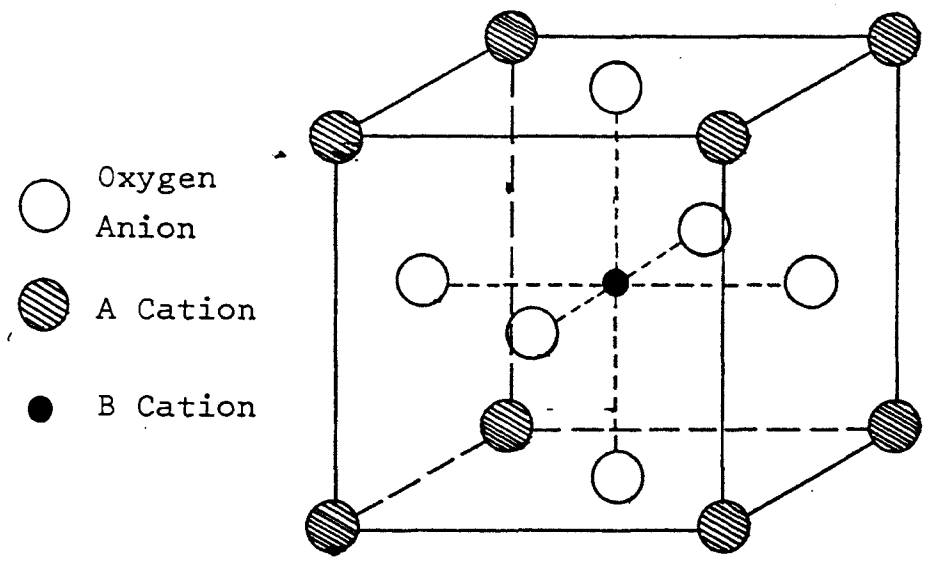

B CATION AT BODY CENTER SITE

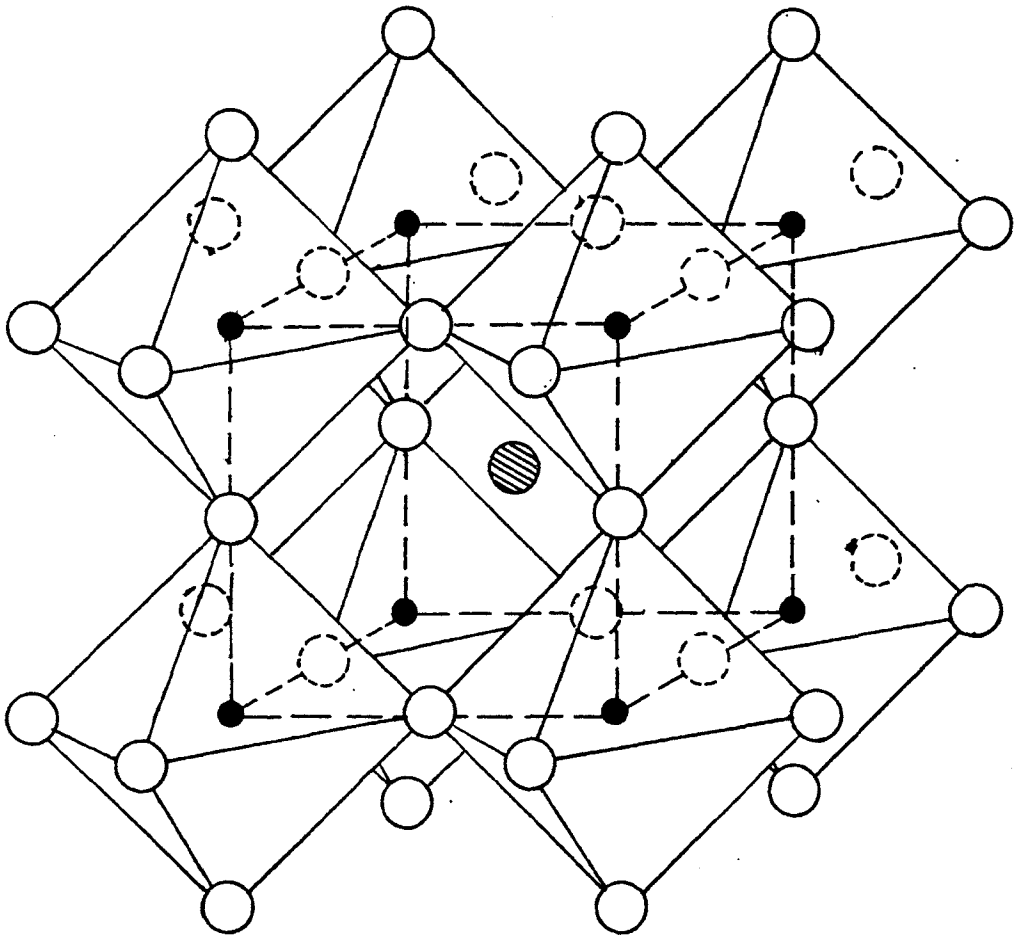

A CATION AT BODY CENTER SITE

Fig. 3. The Perovskite Cell

phases at room temperature. The enhancement of the materials' piezoelectric properties near a phase boundary formed the basis for a group of commercial transducers, with good temperature stability. A modification of this solution is the system $BiFeO_3$-$PbTiO_3$, which has been under study by our group and is considered in this experiment. More about this system will be given in a following section. Listings of some of the common perovskites and their properties are contained in the reviews of Kanzig,[60] Jona and Shirane,[61] and Megaw.[62]

The lattice vibration model for perovskites require that there be 15 modes (5 atoms with 3 degrees of freedom). Some of these may be degenerate, or there may be more if the crystal has superstructure, i.e. requires more than one unit cell to make a repeating cell. Of these modes, three are acoustic, one longitudinal and two transverse. The remainder are made up of optic modes which may be degenerate, depending on the translational symmetry in the crystal.

E. THE $PbTiO_3$-$PbZrO_3$-$BiFeO_3$ SYSTEM

This system has been under study by our laboratory since 1964. The literature has been surveyed in the following theses: Chou studied the structure of the $PbZrO_3$-$BiFeO_3$ system;[63,64] the phase diagram for the whole system was given by Clarida,[65] with a later clarification by Achenbach[66] using neutron diffraction results. The dielectric properties were reported by Smith,[67,68] and the magnetic properties by Latham.[69] The phase diagrams are

TABLE I.

IONIC RADII FOR PEROVSKITES

	$PbZrO_3$	$PbTiO_3$	$BiFeO_3$	$LiNbO_3$	$BaTiO_3$
A	1.20 Å	1.20 Å	0.96 Å	0.68 Å	1.34 Å
B	0.79	0.68	0.64	0.69	0.68
O	1.32	1.32	1.32	1.32	1.32
t	0.85	0.89	0.82	0.70	0.94

The Goldschmidt tolerance factor t is given in equation 20.

TABLE II.

CRYSTALLOGRAPHIC DATA FOR THE $BiFeO_3$-$PbZrO_3$-$PbTiO_3$ SYSTEM

Sample	Space Group	Lattice Parameters a	b	c	α or $\frac{c}{a}$	T_{Curie}	T_{Neel}
$BiFeO_3$	R3c	5.62 Å	-	-	59°41'	850°C	642°K
(psuedo-cubic;		3.96	-	-	89°30')		
$PbTiO_3$	P4mm	3.90	-	4.15	1.06	490°C	---
$PbZrO_3$	Pbam	5.88	11.77	8.22	---	230°C	---

TABLE III.

ATOMIC DISPLACEMENTS FOR R3c PEROVSKITES

	$PbZr_{0.9}Ti_{0.1}O_3$	$BiFeO_3$	$LiNbO_3$
A	0.32 Å	0.62 Å	0.71 Å
B	0.10	0.23	0.26
O	0.22	0.30	0.60
T_{Curie}	270°C	850°C	1210°C

KEY

R_M - Rhombohedral Multiple Cell
C_P - Pseudocubic Cell
T_S - Tetragonal single Cell
R_s - Rhombohedral Single Cell
O_M - Orthorhombic Multiple Cell
Crosslining - Two Phase Region
Crosshatching - Multiphase or Uncertain Region
Dashed Line - Undefined Phase Boundary

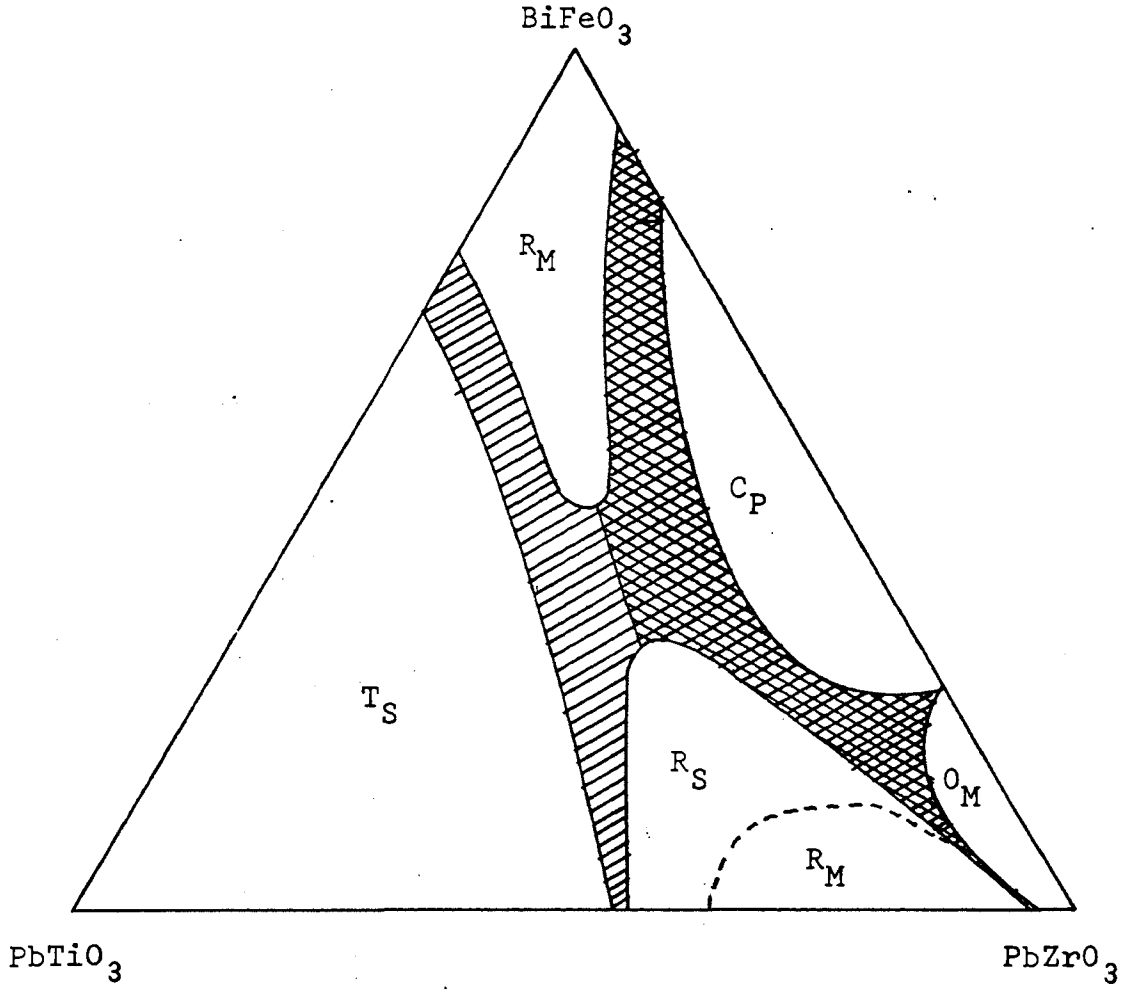

Fig. 4. Ternary Phase diagram of the $PbTiO_3$-$PbZrO_3$-$BiFeO_3$ system (From Achenbach[66]).

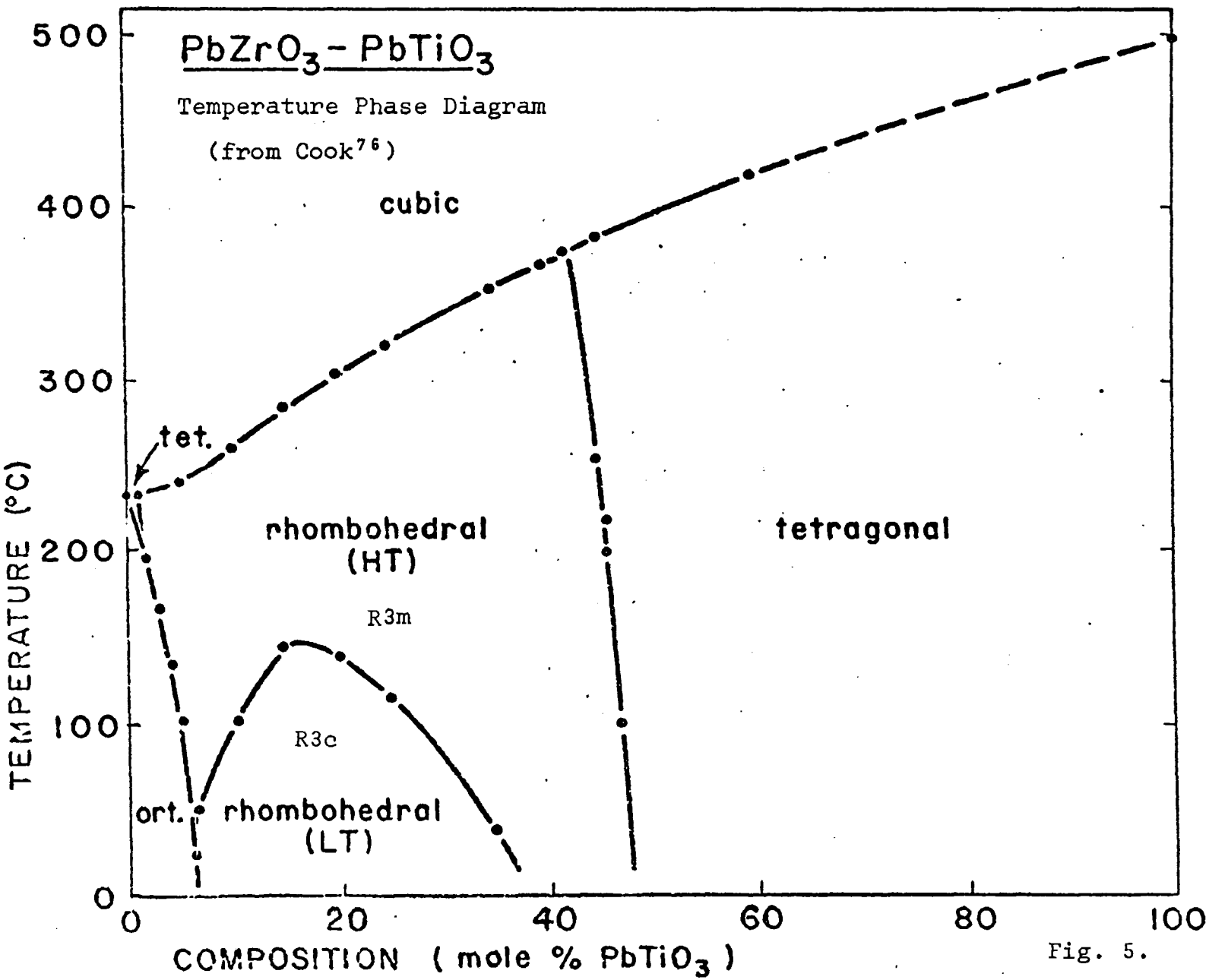
PbZrO3 - PbTiO3
Temperature Phase Diagram
(from Cook76)
cubic
tet.
rhombohedral
(HT)
R3m
tetragonal
R3c
ort.
rhombohedral
(LT)
TEMPERATURE (°C)
COMPOSITION (mole % PbTiO3)
0
100
200
300
400
500
0
20
40
60
80
100

Fig. 5.

given in figs. 4 and 5. The ferroelectric transitions temperatures are given in table II, along with the crystal space groups and magnetic transition temperatures.

Recent work in our lab by Michel and Moreau[70,71,72] with $BiFeO_3$ $PbZr_{.9}Ti_{.1}O_3$ and $PbZr_{.58}Ti_{.42}O_3$, using neutron diffraction on powders and X-rays on single crystals, have clarified the rhombohedral phase regions of this system. Two of these compounds are found to have the same symmetry, R3c. The atomic displacements from ideal perovskite cubic structure are shown in figure 6 and are listed in table III. The structure is isomorphous to the very high Curie temperature compound, $LiNbO_3$ (T_c = 1210 C). As can be seen in the table III, the distortion is much greater for higher Curie temperatures. Megaw[73] has shown that the structures appear to represent a nearly continuous change from hexagonal close-packed to cubic close-packed as the Curie temperature of the compound decreases. As the oxygen rotate, the A and B atoms are displaced to accomodate themselves in the changing void shape. Projections of the different layers along the [111] cubic axis (the [001] axis in the hexagonal system) for this change are shown in figure 7. The symmetry changes in $PbZr_{.9}Ti_{.1}O_3$, suggested by the results of Michel and Moreau,[72] are from multiple-cell ferroelectric,R3c, to single-cell ferroelectric,R3m, and then to cubic,Pm3m. The sequence may depend on the size of the A and B ions,since Abrahams et al.[74]have suggested that $LiNbO_3$ goes to either $R\bar{3}$ or $R\bar{3}c$,both of which are centrosymmetric. No details are

Magnitude of Ion Shifts:

Pb: 0.32 Å along [111]
Zr,Ti: 0.10 Å along [111]
O : 0.22 Å rotating about [111]

All values ± .02 Å

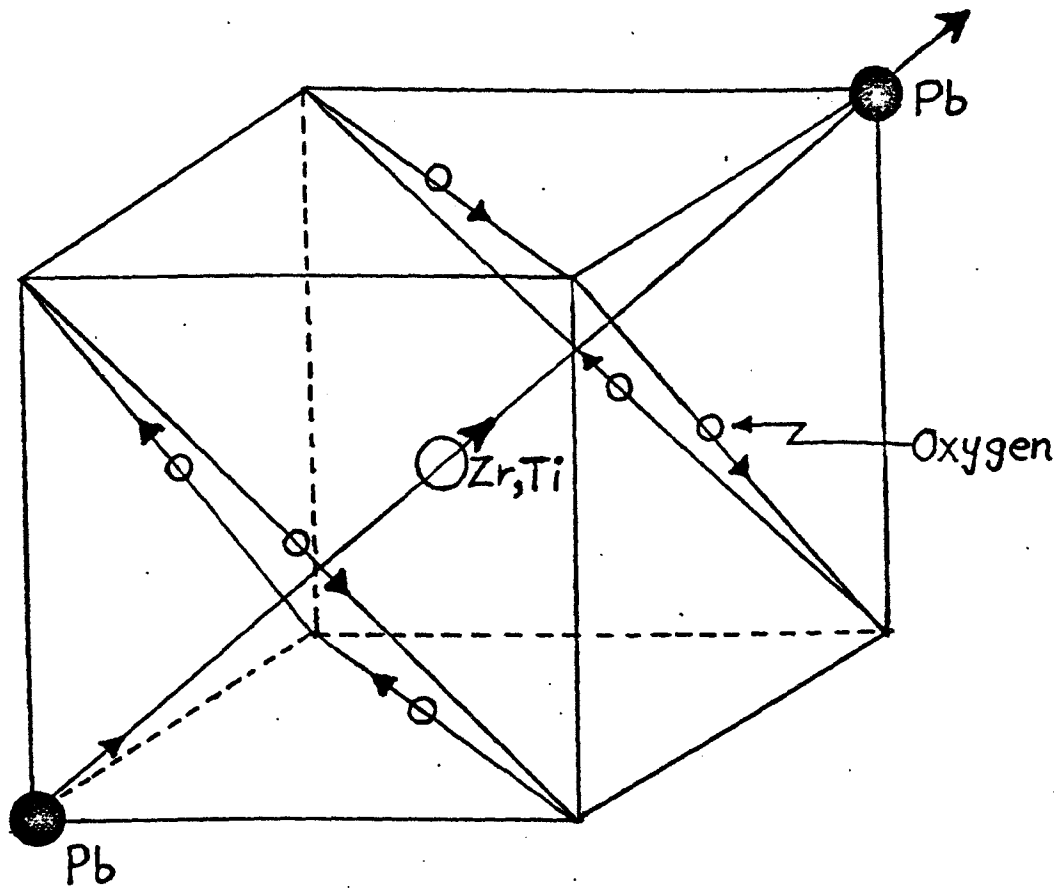

Fig. 6. Atomic Displacements in $PbZr_{0.9}Ti_{0.1}O_3$.

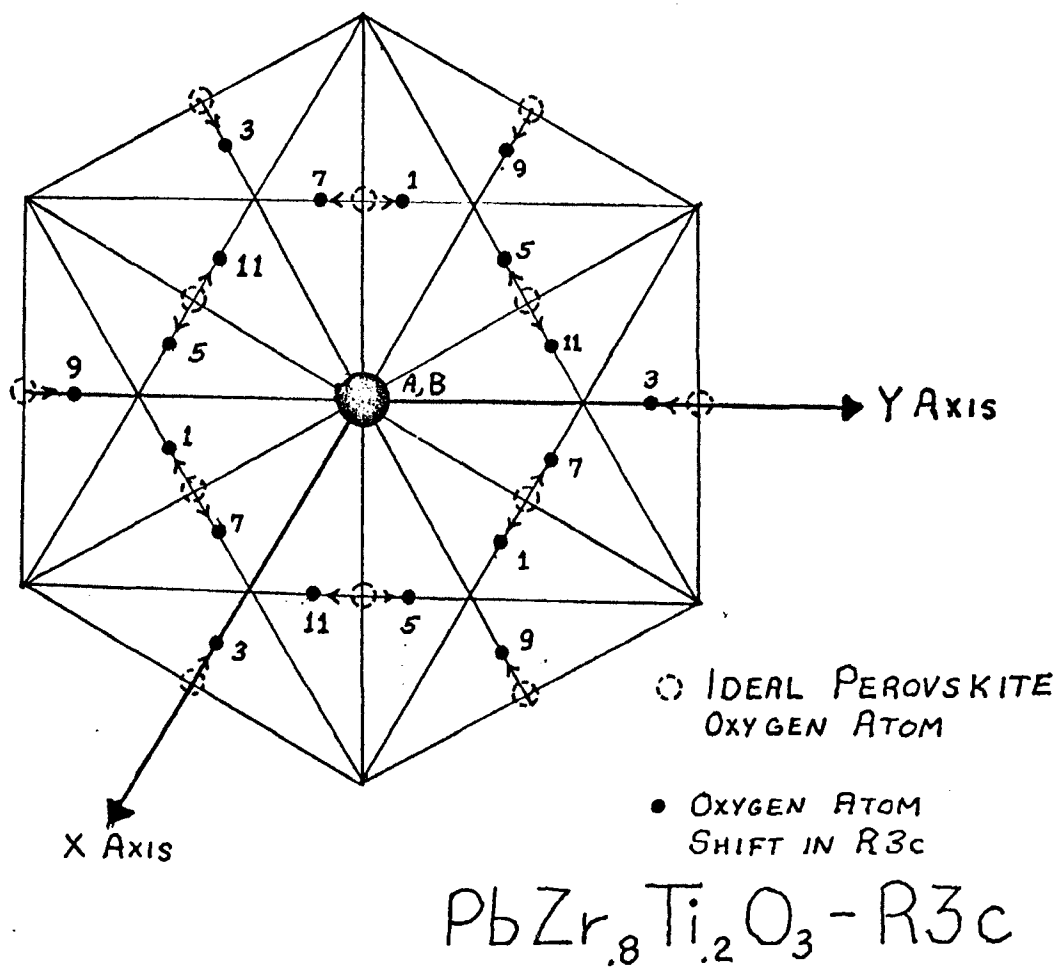

Fig. 7. Projection of oxygen atoms on (001) plane for R3c perovskites. The numbers give distance above plane in twelfths.

available for $BiFeO_3$, which melts just above its Curie point. No model has been worked out for possible geometrical relationships which might determine the symmetry changes in the phase transition, or the order of the phase transition. A linear relation exists for the A and B ion displacements. It is given as $\delta(A) = 2.92\ \delta(B)$.[72] Abrahams, Kurtz, and Jamieson[74] have experimentally related the shift of the B ion to the Curie temperature and the spontaneous polarization, which has been substantiated by the statistical theory of Lines.[34]

The unit cell of $PbZrO_3$ found by Jona et al.[76] is shown in fig. 8. This shows one layer of the structure, containing 4 formula units, and bounded by planes normal to the c axis. The antisymmetry can be seen by observing that two Pb atoms are shifted in a positive direction, and two in a negative direction, from the symmetric positions. The oxygen shifts have been analyzed by Cochran and Zia,[48] and shown to be due to two lattice modes. The Γ_{25} mode with wave vector $(\frac{1}{2}\ \frac{1}{2}\ \frac{1}{2})$ shifts the atoms as shown in fig. 9b. The Γ_{15} mode with wave vector (000) shifts the atoms as shown in fig. 9c. The composite gives fig. 9a, which is the displacement for one formula unit of $PbZrO_3$. The Γ_{25} mode at $(\frac{1}{2}\ \frac{1}{2}\ \frac{1}{2})$ is the same mode which explains the oxygen shift in $LaA\ell O_3$, $LiNbO_3$, $BiFeO_3$, $PbZr_{0.9}Ti_{0.1}O_3$ and $SrTiO_3$. Cochran and Zia[48] comment that the two-lattice models of Kittel[54] and Cross[55] are not completely valid for $PbZrO_3$. They find little weight for or against the suggestion that

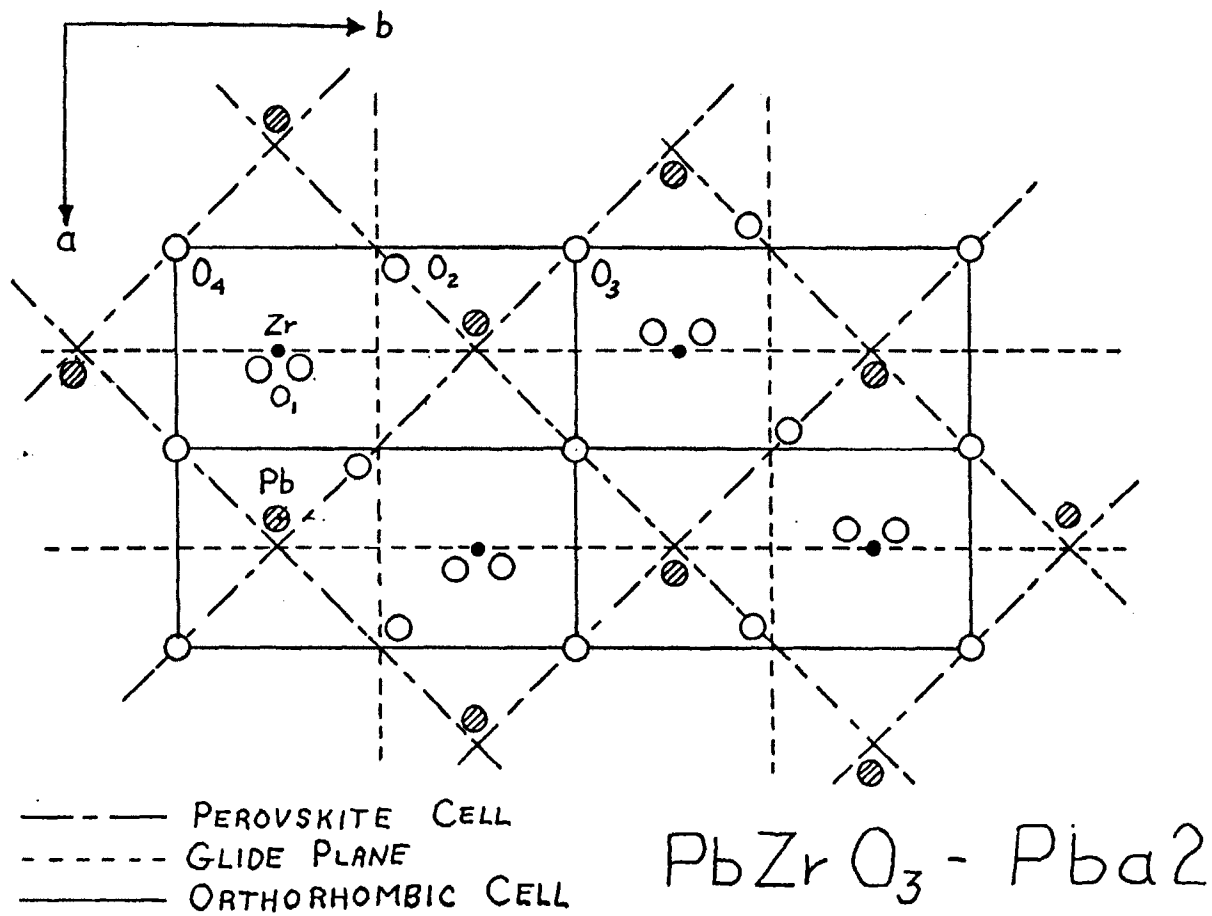

Fig. 8. Projection of atoms on (001) plane for Pba2 perovskites.

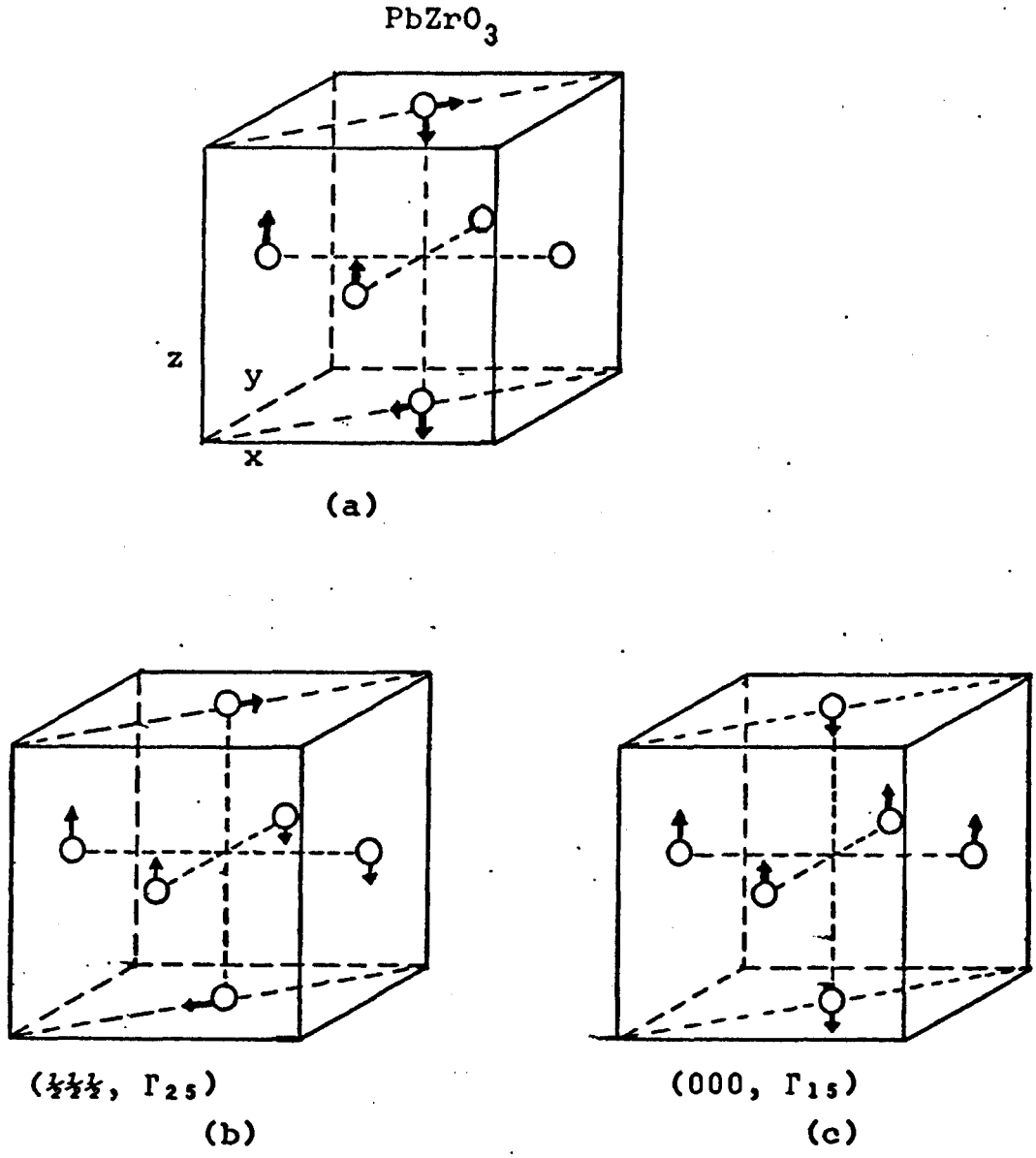

Fig. 9. Displacements of oxygen atoms in $PbZrO_3$ and their decomposition into two lattice modes.

Γ_{25} is the mode that causes the antiferroelectric phase transition and state that any one of the other modes, $(\frac{1}{2}\frac{1}{2}0,\Sigma_3)$ and $(\frac{1}{2}\frac{1}{2}0,M_5')$, are just as likely to be temperature dependent near the phase transition.

The addition of up to 20% $BiFeO_3$ to $PbZrO_3$ has shown that the antiferroelectric phase remains with a decrease in Curie temperature.[64] It is likely that, near the Curie temperature, a ferroelectric phase exists, with rhombohedral symmetry. This phase has been observed with the addition of $BaZrO_3$,[77] $PbTiO_3$[78] and possibly 0.5% Nb_2O_5[79] to $PbZrO_3$. The ferroelectric phase is most easily detected by the observation of double hysteresis loops. The field required to excite the double loops decreases as the temperature approaches the Curie point. X-ray lines[77] are often diffuse in the narrow temperature range (5-10°C) over which the ferroelectric phase may exist, suggesting a soft lattice.

The rotation of the oxygen octahedra also takes place in the low temperature phase ($T \leq 110°K$) of $SrTiO_3$. This was confirmed using EPR experiments by Unoki and Sakudo.[80] The determination that the corresponding lattice mode is temperature dependent was made by Shirane and Yamada[81,82] and independently by Cowley, Buyers and Dolling,[83] using neutron inelastic scattering. This mode (Γ_{25}) occurs at the zone boundary and is the tetragonal analog of the phase transition of $LaAlO_3$, discussed by Cochran and Zia,[48] and observed by Axe, Shirane and Mueller,[84] and by Cochran,[85]

using neutron and X-ray scattering techniques, respectively. A theoretical treatment was given by Thomas and Mueller.[86] The latter were able to establish the conditions for either the tetragonal or trigonal rotation of the oxygen, based on anharmonic parameters. These results are general and do not imply ferroelectricity, but are often present in ferroelectric systems, so a connection must be sought.

F. THE MOSSBAUER EFFECT IN FERROELECTRICS

A brief history of the observance of the Mossbauer effect in ferroelectrics is given before examining the specific parameters that can be measured. Muzikar and Janovec and Dvorak[87] proposed that Mossbauer effect should be useful for the study of ferroelectrics in observing the effects of a soft lattice mode. It was demonstrated that the low frequency mode should have a marked effect on the fraction, f, of recoilless emission. Schmidt[88] gave a derivation to show this effect for a rigid lattice containing a ferroelectric-active B ion. Since only the interaction of the B ions with the lattice was considered, only qualitative results were obtained. A simplified demonstration of the dependence of the f factor on the soft phonon mode may be given following the derivation Abragam.[8] For each phonon mode, the energy is given as:

$$NM\omega_s^2\langle u_s^2\rangle = (\bar{n}_s + \tfrac{1}{2})\,\hbar\omega_s \qquad (21)$$

where N is the number of atoms in the lattice,

M is the mass of the A atom,

$\bar{n}_s$ is the number of phonons having frequency ω_s,

u_s is the displacement of the atom from equilibrium,

$\hbar$ is Planck's constant/2π.

Summing over all the modes:

$$k^2\langle x^2\rangle = k^2 \frac{\langle u^2\rangle}{3} = \frac{2R}{3\hbar N} \sum_s \frac{(\bar{n}_s + \frac{1}{2})}{\omega_s} \tag{22}$$

where k is the momentum vector of the gamma ray,

R is the recoil energy of the atom $\frac{(\hbar k)^2}{2M}$.

The value for $\bar{n}_s$ is given by the Bose-Einstein formula:

$$\bar{n}_s = \frac{1}{\exp(\frac{\hbar\omega_s}{k_B T})-1} \tag{23}$$

where k_B is the Boltzmann constant,

T is the absolute temperature.

After substituting this value of $\bar{n}_s$ in (22), there results:

$$k^2\langle x^2\rangle = \frac{R}{3\hbar N} \sum_s \frac{1}{\omega_s} \coth\left(\frac{\hbar\omega_s}{2k_B T}\right) \tag{24}$$

where the sum is over all the lattice modes. If one mode becomes soft, its frequency ω_i approaches zero, and that term of the sum approaches infinity. The statistical weighting (not included in the derivation) of the modes gives a finite sum, so that the large term should predominate in the sum. This means that a dip will be observed in f ($f = e^{-k^2\langle x^2\rangle}$) at the temperature at which the mode softens.

The primitiveness of the early Mossbauer Effect (ME)

measurements on ferroelectrics is shown in the report by Pham Zuy Hien, Viskov, Shpinel', and Venevtsev[89] on $BiFeO_3$-$SrSnO_3$ solid solutions. An abrupt change was observed in the peak intensity at temperatures between 300° and 700°K for the various solutions. These were mistakenly interpreted to be the ferroelectric transition points by the transposition of °K for °C. The mistake was pointed out in a paper by Mitrofanov, et al,[90] in which complete spectra were run in contrast to the single velocity data points observed previously. The abrupt transition was found to be due to the antiferromagnetic transition in $BiFeO_3$ at 642°K (369°C). The single peak spectrum decreases as the six-peak magnetic spectrum appears. It was another year before confirmation of the usefulness of the ME in ferroelectrics was made. Bhide and Multani[91] observed the anomalous dip in f for the 120°C transition in $BaTiO_3$, using Fe impurity diffused into the sample as the Mossbauer active atom. Almost simultaneously, Chekin, et al.[92] observed the ME in $BaTiO_3$ doped with Sn^{119} and found the same behaviour for f, though not as sharply defined as it was for iron, because of the larger natural linewidth of tin. The effect has been studied for solid solutions of $BaTiO_3$-$BaSnO_3$ by Bokov, et al.[93] The effect has also been observed at the lower temperature phase transitions of $BaTiO_3$ investigated by Belov and Zheludev.[94] There remains, however, some difficulty, for Plotnikova, et al.[95] have attempted

the same experiments and found negative results, although they claim that they had much better resolution than the previous experiments. They also investigated the spectrum for $Pb(Ti,Sn)O_3$ and $Pb(Zr,Sn)O_3$, and found no effects at the phase transition.

Very good results have been obtained by Sklyarevskii et al.[96] for $Pb\ Fe_{\frac{1}{2}}Nb_{\frac{1}{2}}O_3$ using enriched iron (Fe^{57}) as the Mossbauer active atom.

Work with iron in perovskites has always been plagued with valency problems because the iron assumes two or more valency states.* For $BaTiO_3$, Bhide and Multani[91,97] discussed the vacancy impurity state caused by the insertion of Fe^{3+} in a site usually occupied by Ti^{4+}. To obtain a better spectrum, they resorted to using $BaTiO_3$ as a source containing Co^{57} in the 2+ state. Similar work on $SrTiO_3$ showed the same effect.[99,100]

Some work on $Pb(NbFe)_{\frac{1}{2}}O_3$ and $Sr(TaFe)_{\frac{1}{2}}O_3$ was performed by Bell.[101] The broadness of the observed peaks were explained by the random arrangement of the iron in the B

---

* Matthias[98] has suggested that the B ion in Perovskite ferroelectrics must be noble gas structures. Fe^{3+} violates this, though it approximates the effect by having a $3d^5$ configuration. Fe^{2+} has never been shown to be ferroelectric, and its quadrupole splitting is not temperature dependent to the same extent as is that of Fe^{3+}.

sites of the perovskite cell having different environments due to charge and size differences.*

Work by Gallagher et al.[103] on the oxygen deficient system $SrFeO_x$, where x = 2.50-3.0, using the Mossbauer effect, has observed iron in the 2+, 3+, and 4+ states, all in the same compound. Similarly, Shimony and Knudsen,[104] and Gallagher and MacChesney,[105] in work on $La_{1-x}Sr_xFeO_3$ have found the tetravalent and trivalent iron occupying the same lattice position.

Dvorak[106] has extended the theory for the Mossbauer effect in ferroelectrics to antiferroelectrics by showing that the f factor should be sensitive to soft modes of all values of k, including the zone boundary. He also predicted, on the basis of the results by Silverman,[57] that the decrease in f should be much greater for antiferroelectrics than for ferroelectrics.

Multani and Mueller[107] have recently reported observing the temperature dependent lattice mode behavior in $PbZrO_3$, using Co^{57} embedded in $PbZrO_3$ as a source. No numerical results were given in the brief abstract.

Dlouha[108] has studied the implications of the first order and second order phase transitions to make a few

---

* Recent studies [102] on inhomogeneous broadening define the problem as due to point defects, either vacancies or charge differences, which introduce random strains and electric field gradients, changing the isomer shift and splitting.

predictions on the behaviour of f and of the second order Doppler shift at the transition temperature. A recent paper by Vaks, Galitskii and Larkin [109] has extended the microscopic theory of ferroelectricity by Vaks[27] to give a description of the behaviour of f at the phase transition.

The useful parameters obtained from the ME will be described in the experimental section. These include the isomer shift, electric quadrupole splitting, second order Doppler shift, and the area of the peak.

III. EXPERIMENTAL METHODS

A. MOSSBAUER EFFECT MEASUREMENTS.

1. The Isomer Shift

The isomer shift is one of several hyperfine interactions. Physically it is the interaction of the nuclear charge distribution with the electron charge density at the nucleus. This interaction is given as:

$$\delta E_{is} = \frac{2\pi}{5} Ze^2 \left(|\Psi_a^2 (0)| - |\Psi_s^2(0)| \right) [R_{ex}^2 - R_{gnd}^2] \qquad (25)$$

where Z is the atomic number,

e is the electronic charge,

Ψ_a is the s-electron wave function for the absorber,

Ψ_s is the s-electron wave function for the source,

R_{ex} is the nuclear charge radius for the excited state,

R_{gnd} is the nuclear charge radius for the ground state.

The wave functions of transition metals are difficult to calculate, so that the contribution of Ψ at the nucleus is difficult to evaluate properly. There is always some d-electron interaction with the nucleus that is hard to include. Usually correlation plots of observed values of the isomer shift with other parameters dependent on the charge state of the Mossbauer atom, such as electric quadrupole splitting, are used to make predictions for unknown charge state materials. Such a plot is that of

Spijkerman, Ruegg and May[110] for iron, shown in figure 10. A more theoretical relation was given by Walker, Wertheim and Jaccarino.[111] This related the Hartree-Fock wave functions for the 3d electrons with the 4s electron contribution due to ionicity and with the measured isomer shift for some ionic compounds. The WWJ plot failed to fit ionic compounds reasonably, so Danon[112] recalibrated the results to obtain a better fit. Some 3d-4s compounds, assumed to be ionic by WWJ, show more than 20 per cent covalency. The resulting plots are shown in figure 11.

These results are still ambiguous, so Bhide, Shenoy and Multani[113] have plotted several empirical curves of isomer shift as a function of ionicity. One of these is calibrated for Fe_2O_3 and other Fe^{3+} covalent compounds, and seems to give the most reasonable values of ionicity for the perovskite ferroelectrics. The empirical plot is given in figure 12. Bhide and Multani[91] were able to derive the ionicity from the charge required to give the observed quadrupole splitting. They obtained a value of 60% ionicity for $BaTiO_3$, which was close to the 50% predicted on the basis of isomer shift plot. X-ray spectroscopic investigations of Blokhin and Shuvaev,[114] gave estimated values of covalency greater than 35% for p electrons, and greater than 60% for p and d electron contribution.[115] The s contribution was small. This would indicate that the WWJ[111] plot is an invalid indicator of covalency. Erickson[116] has presented a discussion of the difficulties in relating the

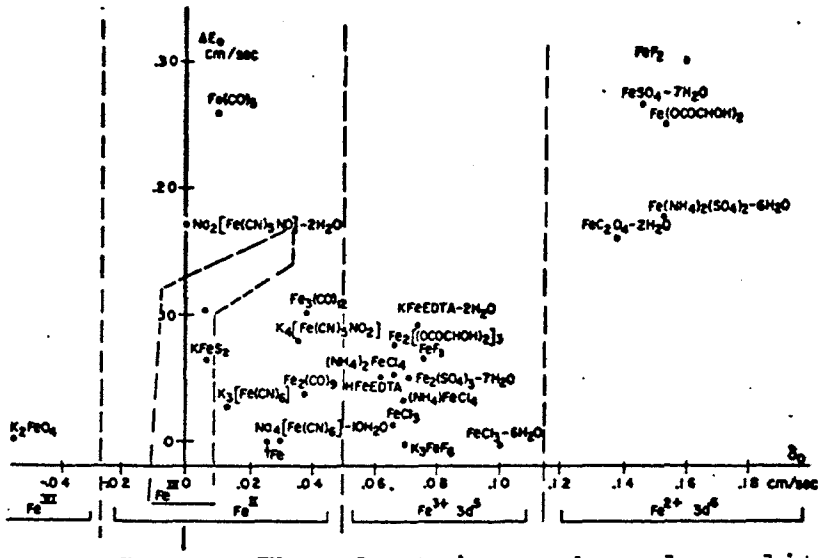

Fig. 10. Scatter Plot. The electric quadrupole splitting and isomer shift measured with respect to sodium nitroprusside are correlated. (from May et al.[110])

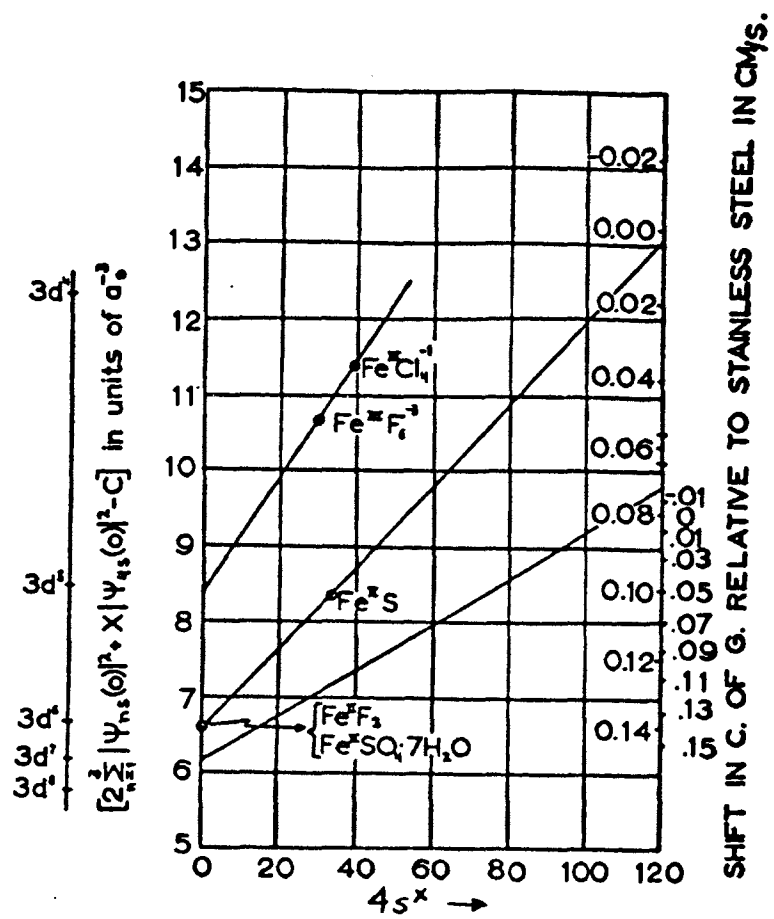

Fig. 11. Calculated electron density aththe nucleus in terms of the per cent 4s electron contribution and isomer shift. Calculation and outer scale on right due to Walker et al.[111] Inner scale on right due to recalibration by Danon.[10]

EMPIRICAL RELATIONSHIP OF THE IONICITY TO THE ISOMER SHIFT FOR Fe^{3+}.

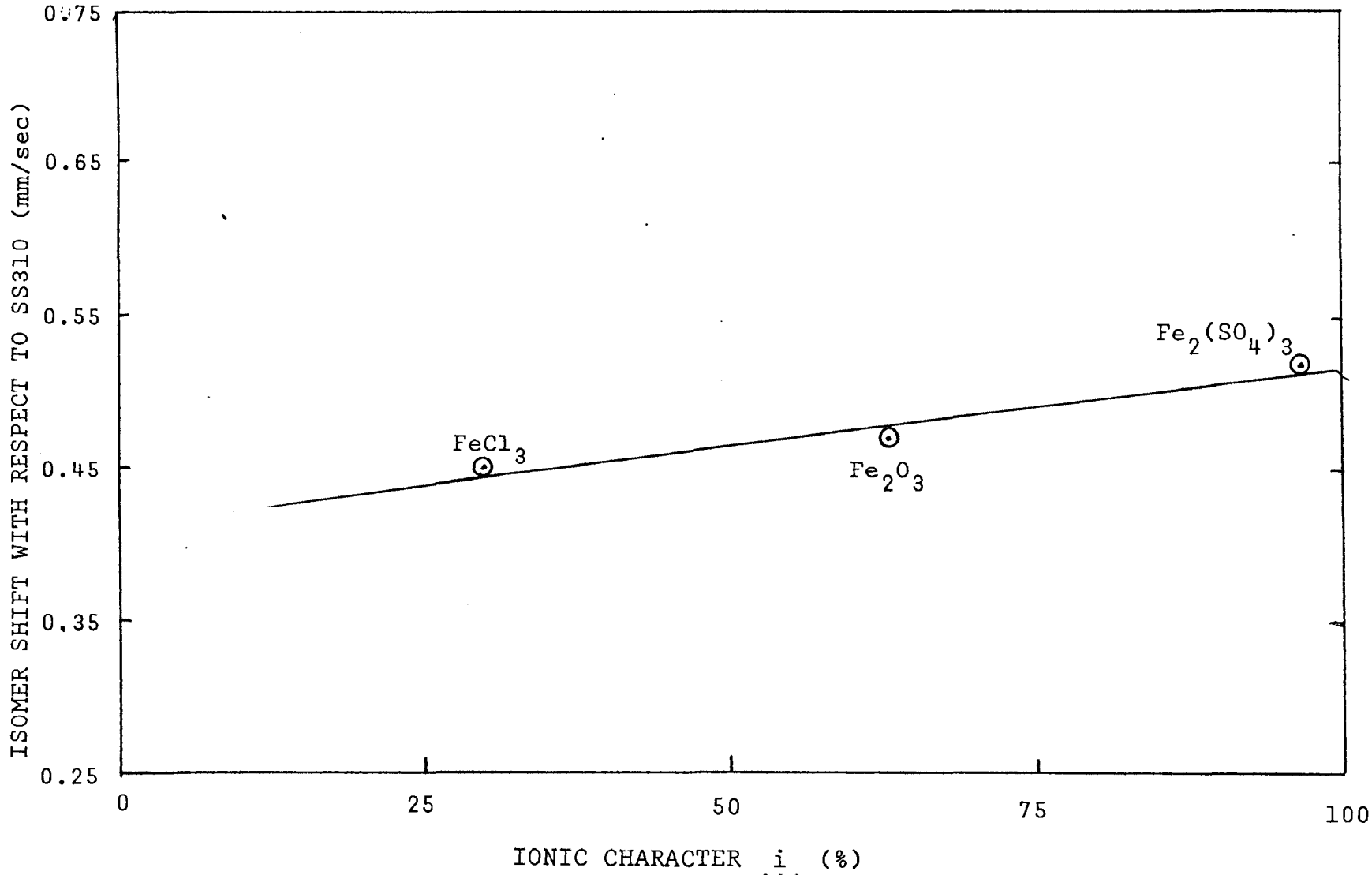

Fig. 12. (From Bhide, Shenoy and Multani[113]).

isomer shift with the ionicity, and proposed a system to give relative covalency only.

2. The Second Order Doppler Shift

The isomer shift can be shown to display a dependence on temperature or pressure, due to the second order Doppler shift of the nucleus. The first order effect is absent due to the lack of recoil in the resonance process. However, the lattice vibrations contribute to the motion of the nucleus and this is detectable in the slope of the isomer shift versus temperature (or pressure) curve. It can be shown that this slope is:

$$\frac{1}{E}\frac{dE}{dT} = -\frac{C_L}{2Mc^2} \tag{26}$$

where E is the energy measured as the isomer shift,

T is the temperature,

C_L is the lattice specific heat,

M is the mass of the atom,

c is the speed of light.

The specific heat is usually given by the Debye Approximation as:[6]

$$C_L = 3Nk\left(\frac{T}{\theta}\right)^3 \int_0^{\theta/T} \frac{z^4 e^z}{(e^z-1)^2}\,dz \tag{27}$$

where N is the number of atoms in the system,

k is Boltzmann's constant,

θ is the Debye temperature.

At low temperatures:

$$C_L = \frac{12\pi^4}{5} Nk\left(\frac{T}{\theta}\right)^3 \tag{28}$$

while at high temperatures, the Dulong Petit law holds:

$$C_L = 3Nk. \tag{29}$$

The order of the phase transition should determine what kind of discontinuity there will be in the isomer shift versus temperature curve. Dlouha[108] stated that for a first order transition that there should be a jump in the curve. For a second order transition there should also be a discontinuity, which should just be a change of slope in the isomer shift-temperature curve.

The jump has been observed in $BaTiO_3$[91] and $Pb(Fe_{\frac{1}{2}}Nb_{\frac{1}{2}})O_3$[96] which probably are first order transitions. The slope of the curve seems to fall just short of the Dulong-Petit law for high temperatures in $BaTiO_3$. Unless this is measured very far above the phase transition, there may be an effect due to the hyperfine interaction or the volume change, which adds an additional term to the slope.

3. The Electric Quadrupole Splitting.

This splitting is due to the interaction of the crystal's electric field gradient with the nuclear quadrupole moment of the atom undergoing a recoilless transition. The nuclear energy levels are split by the amount:

$$E_Q = \frac{e^2qQ}{4I(2I-1)}[3m_I^2 - I(I+1)](1+\frac{1}{3}\eta^2)^{\frac{1}{2}} \tag{30}$$

where e is the electronic charge,

eq is the major term of the diagonalized electric gradient, V_{zz},

Q is the nuclear quadrupole moment, ($Q_{ij} = \int \rho(r) x_i x_j d\vec{r}$),

I is the nuclear spin quantum number,

m_I is the magnetic quantum number,

η is the assymmetry parameter of the electric field gradient, $\frac{V_{xx}-V_{yy}}{V_{zz}}$.

The electric field gradient is the second derivative tensor of the electric potential or the gradient of the electric field vector. It is diagonalized by a suitable choice of axes and arranged so that the dominant term is the V_{zz} term. From the above equation, for iron with I = 3/2 and 1/2 for the excited and ground states respectively, we see that only the excited state can be split by this interaction, and hence only two lines will be observed in a spectrum. The energy level diagram is given in figure 13. This gives the value for the splitting as:

$$\Delta E_Q = \tfrac{1}{2}\, e^2 qQ(1-\gamma_\infty)(1+\eta^2/3)^{\frac{1}{2}}, \qquad (31)$$

where an additional factor has been introduced to account for the contribution of the Mossbauer atom's electrons to the electric field gradient of its surroundings. This is called the Sternheimer[117] antishielding factor, γ_∞, because

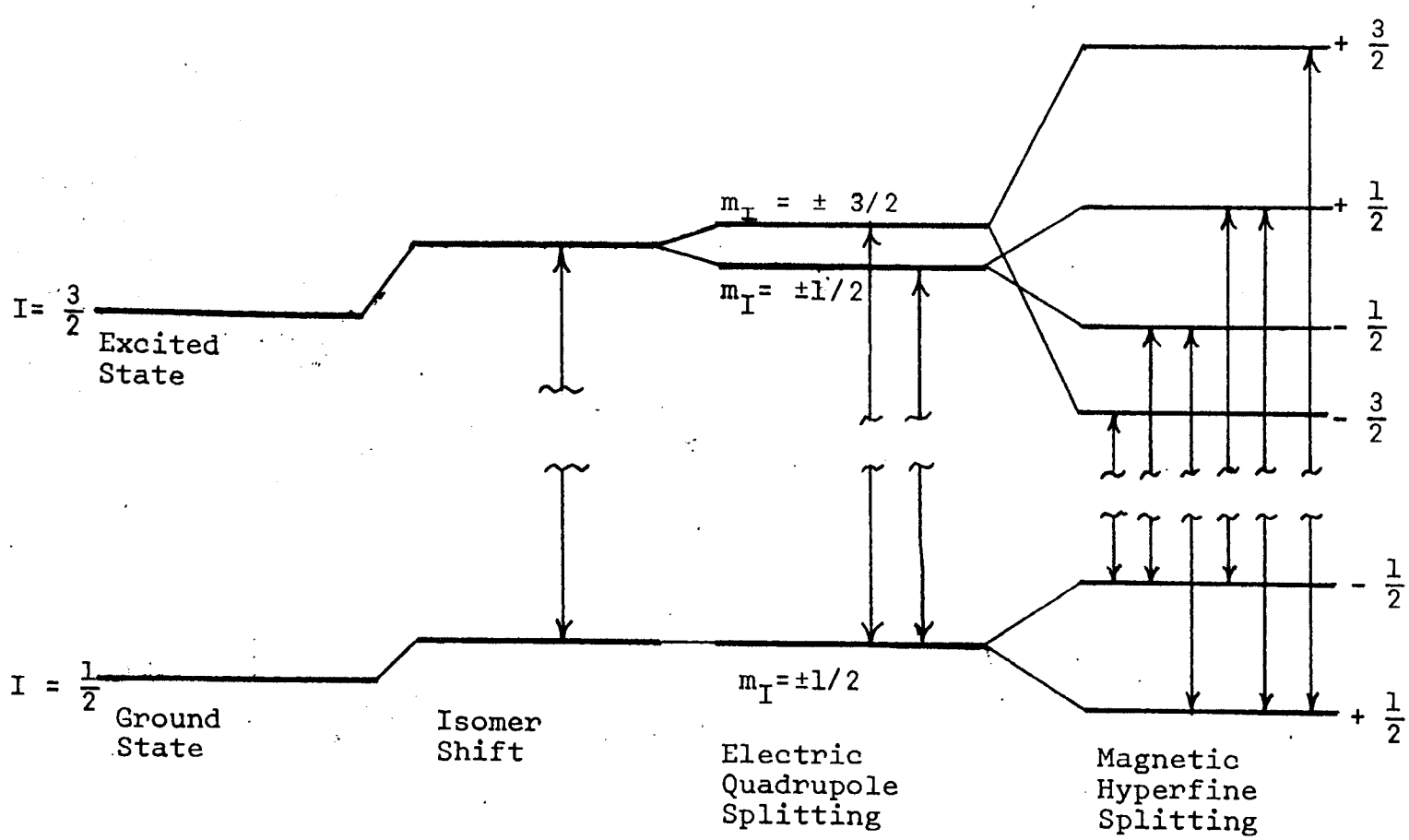

Fig.13 Nuclear Hyperfine Interactions for Iron 57.

the outer electrons of the atom seem to enhance the field gradient at the nucleus. For Iron 57, its value is given as -9.16.

The value of Q for Iron 57 is not known exactly, but has been estimated to be between 0.19 and 0.32 barns (10^{-24} cm). The difficulty is that the measurements of this factor usually include the electric field gradient term, eq, so that a good estimate of this term must be available before Q can be determined. A recent paper by Chappert, et al.[118] summarizes the results obtained in other recent papers and includes a new determination of Q as 0.21 ± 0.03 barns.

The electric field gradient calculation requires summation over discrete charges in the surrounding cells of the Mossbauer ion. Methods for making these calculations are discussed by Bersohn,[119] and a series of Russian papers have appeared dealing with electric field calculations in perovskites.[120,121] These were extended to perovskites having superstructure[122,123] and, in particular, to antiferroelectrics such as $PbZrO_3$.[124,125] Electric field gradients have been estimated for $BiFeO_3$ to be between 2 and 6 x 10^{16} V/cm^2. While the structure is now known to be slightly different, order of magnitude agreement with measured values was found.

Bhide and Multani[91] made a calculation determining the ionicity of $BaTiO_3$ from their experimental results.

TABLE V.

ABSORPTION FACTORS FOR VARIOUS MATERIALS

MATERIAL	THICKNESS RANGE (cm.)	ENERGY OF RADIATION (kev)	ABSORPTION COEFFICIENT μ (cm^{-1})	HALF THICKNESS (cm.)
ALUMINUM	0.004 - 0.084	14.4	18.18	0.04
		6.3	190.	0.06
BERYLLIUM	0.004 - 0.14	14.4	1.124	0.17
		6.3	4.190	0.62
CELLOPHANE TAPE	0.006 - 0.051	14.4	1.297	0.53
		6.3	13.985	0.05
FUSED QUARTZ	0.006 - 0.47	14.4	13.	----
		6.3	40.	0.10
MYLAR	0.008 - 0.009	14.4	7.4	0.09
		6.3	11.52	0.06
PLEXIGLASS	0.16 - 0.97	14.4	0.9	0.69
		6.3	15.	0.08
POLYETHYLENE	0.014 - 0.21	14.4	0.829	0.84
		6.3	6.0	0.11
POLYPROPYLENE	0.16 - 0.79	14.4	0.5124	1.34
		6.3	5.5	0.14
TEFLON	0.008 - 0.42	14.4	3.79	0.19
		6.3	39.	0.05

From L. May and D. K. Snediker, Nuclear Instrum. and Methods, 55, 183-188 (1967).

RANDOM B SITE OCCUPATION OF DIFFERENTLY CHARGED ATOMS

ATOMIC ARRANGEMENT ● B(+4), ○ B'(+3)	PROBABILITY $\times \frac{1}{64}$	ELECTRIC FIELD GRADIENT $\times \frac{1}{4\pi\epsilon_0} \frac{\Delta e}{a^3}$	QUADRUPOLE SPLITTING $\times \frac{eQ}{8\pi\epsilon_0}(1-\gamma_\infty)\frac{\Delta e}{a^3}$
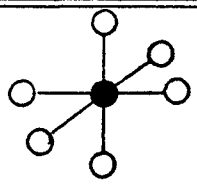	2	$V_{zz} = 0$ $V_{xx} - V_{yy} = 0$	$\Delta E = 0$
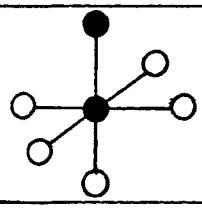	12	$V_{zz} = 2$ $V_{xx} - V_{yy} = 0$	$\Delta E = 1$
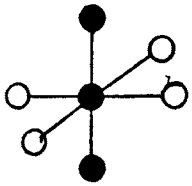	6	$V_{zz} = 4$ $V_{xx} - V_{yy} = 0$	$\Delta E = 2$
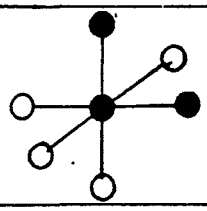	24	$V_{zz} = 1$ $V_{xx} - V_{yy} = 3$	$\Delta E = 1$
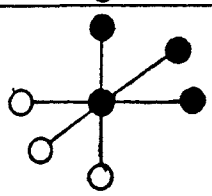	8	$V_{zz} = 0$ $V_{xx} - V_{yy} = 0$	$\Delta E = 0$
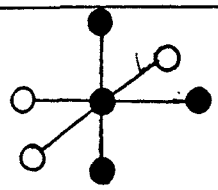	12	$V_{zz} = 3$ $V_{xx} - V_{yy} = 3$	$\Delta E = \sqrt{3}$

IN DIAGONALIZED FORM, $\Delta E = \frac{eQ}{2} V_{zz}\left(1 + \frac{(V_{xx}-V_{yy})^2}{3V_{zz}^2}\right)^{\frac{1}{2}}$

WHERE $V_{zz} \propto (1-\gamma_\infty)\frac{\Delta e}{a^3}$ for splitting due to charge difference $e_B - e_{B'}$.

$\Delta E = 0$	$P = 10/64$	$\Delta E = \sqrt{3}$	$P = 12/64$
$\Delta E = 1$	$P = 36/64$	$\Delta E = 2$	$P = 6/64$

TABLE 4

which also show antiferromagnetic ordering. These include $BiFeO_3$, and $Pb\ Fe_{\frac{1}{2}}Nb_{\frac{1}{2}}O_3$. The interaction is between the electronic spin and the nuclear spin, I. It is given by

$$E_M = -g\mu_N\ H\ m_I, \text{ where } m_I = I,\ I-1,\ldots,-I, \qquad (32)$$

where g is the gyromagnetic ratio for the nucleus,

μ_N is the nuclear magneton,

H is the magnetic field at the nucleus,

m_I is the nuclear magnetic quantum number.

The allowed transitions are given by the selection rule for magnetic dipole transitions:

$$\Delta m_I = 0,\ \pm 1. \qquad (33)$$

In the case of iron, the transitions are between states for which I = 3/2 and 1/2. This means that there are four levels in the excited state which can decay to two levels in the ground state. This is shown in fig. 13.

In magnetic materials of low symmetry, one would expect an electric quadrupole splitting along with the magnetic splitting. Often this is hard to detect, as the effect depends on the angular relationship between the electric field gradient and the magnetic field. One example is that of Fe_2O_3, which has its electric field gradient tensor diagonalized along its magnetic field above the Morin transition (spin flip), but perpendicular below the Morin transition. The energy level diagram is given in fig. 13.

5. The Area of the Resonance Peak

The variation of the f factor in the temperature range of a phase transition has been discussed. The experimental determination of f follows from the measurement of the count rate. A measurement is made of the fraction effect $\varepsilon(E_o)$:

$$\varepsilon(E_o) = \frac{N(\infty) - N(E_o)}{N(\infty) - N(B)} \qquad (34)$$

where $N(\infty)$ is the total count rate off resonance,

$N(E_o)$ is the total count rate at resonance E_o,

$N(B)$ is the contribution to the total count rate of non-resonant radiation (other gamma rays). The background contribution $N(B)$, is due to secondary gamma rays from interactions of the higher energy gamma rays also emitted by the source. The above equation is valid only if the linewidth of the source and the absorber are the same. This is because broadening of the one with respect to the other would cause a reduction in relative height.

The area of the peak (in the count rate-velocity spectrum) is a more exact measure of resonant absorption. The height is normalized in the same way, but now the area is used:

$$A = \pi \Gamma \varepsilon(E_o). \qquad (35)$$

where $\varepsilon(E_o)$ is relative height of peak of E_o,

Γ is the total linewidth (FWHM).

The theoretical expression for this area is given as a

function of the absorber and source thickness. This has been determined in analogy with neutron resonance absorption experiments, the results being given by Preston, Hanna, and Heberle,[127] using numerical results derived by Havens and Rainwater.[128] The final results were:

$$A = \tfrac{1}{2}\pi\, n\sigma_o f_s f_a \Gamma\, G(n\sigma_o f_a) \text{ for thin absorbers} \qquad (36)$$

and

$$A^2 = \pi\, n\sigma_o f_a f_s^2 \Gamma^2 F(n\sigma_o f_a) \text{ for thick absorbers} \qquad (37)$$

where n is the number of resonant nuclei per cm^2,

σ_o is the resonant cross-section for absorption,

f_a is the absorber Mossbauer fraction,

f_s is the source Mossbauer fraction,

Γ is the total linewidth (FWHM), and

F and G are thickness corrections given in figure 14.

A number of other numerical calculations have been made to correct for the thickness of the absorber. The most important ones are those of Shirley, Kaplan, and Axel,[129] Lang,[130] Marguilles and Ehrman[131] and Bykov and Pham Zuy Hien.[132] A new method for measuring the f factor was used by Housley, Erickson and Dash,[133] in which a black absorber, ammonium lithium fluoferrate, was used to provide a broad flat absorption as a standard with which to compare the unknown.

6. The Linewidth

The observed linewidth is due to the overlap of both the source and absorber linewidths to give a sum of the two.

THICKNESS CORRECTION FACTORS FOR CALCULATION OF MOSSBAUER FRACTIONS

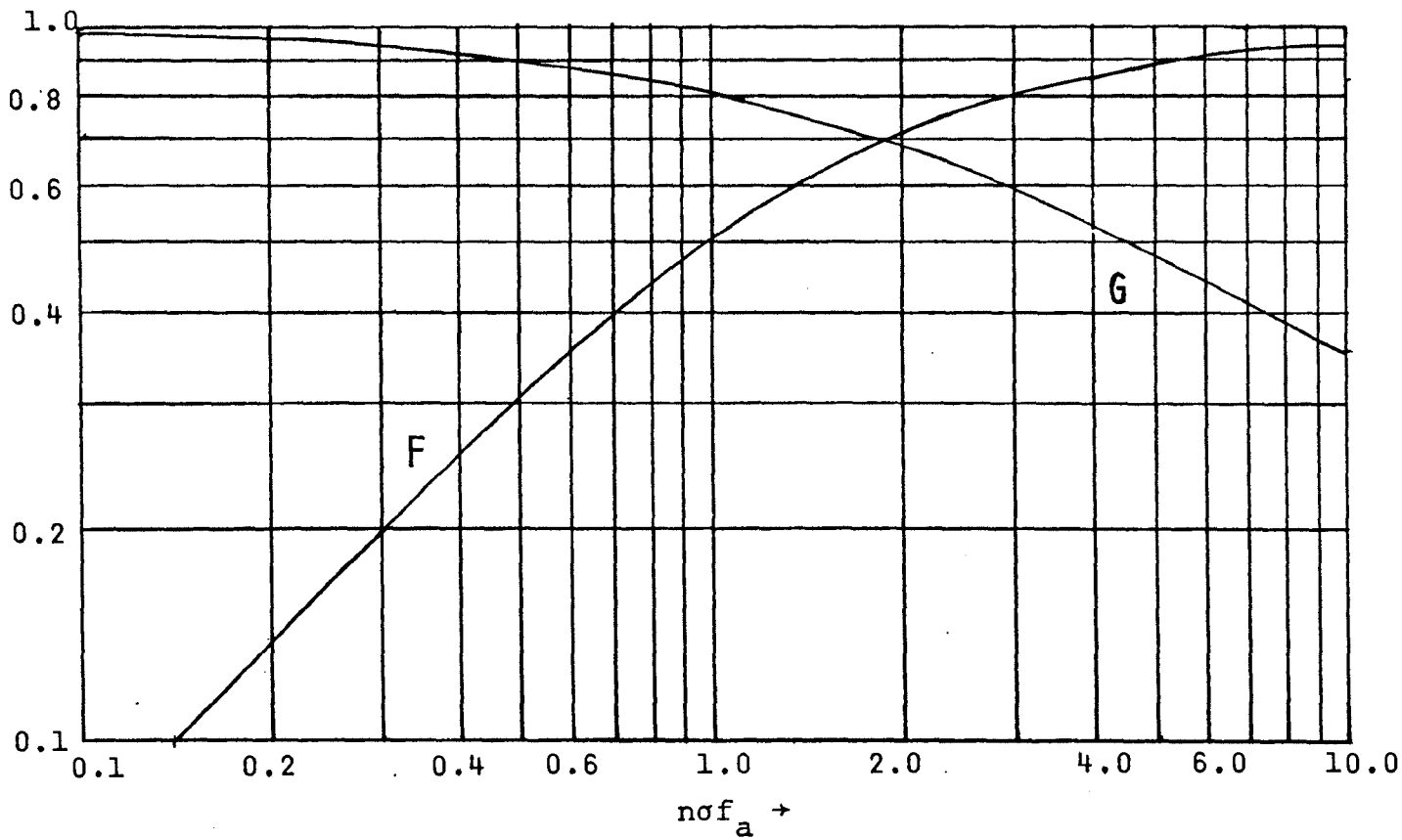

Fig. 14. (From Havens and Rainwater[128]).

The linewidth of either the source or absorber can be broadened due to relaxations, fluctuations and inhomogeneous broadening. The fluctuations and relaxations which occur near phase transitions are of most importance in this experiment. If a fluctuation is slow enough so that the period is longer than the life time of the excited state, then the Mossbauer effect is capable of detecting its effect on the crystal environment. The existence of such states in ferroelectrics was discussed by Fritsberg[134] in terms of microphases of volumes of the order of $10^{-18}cm^3$. Shur[135] has suggested a possible thermal instability in ferroelectrics due to conductivity, which should be small for $BaTiO_3$ but larger for SbSI and the more conductive ferroelectrics. This could give rise to relaxation effects.

7. Miscellaneous Effects

In an anharmonic crystal, one might expect that the Debye model fails to fit the specific heat and lattice mode spectrum, thus leading to apparent anomalies in the measurements. Also, if the f factor can vary for different crystalline directions, one can expect that the peak intensities for electric quadrupole splitting and magnetic splitting will change with orientation. It has been suggested by Goldanskii and Karyagin[136,137] that the peaks will be unequal (even in powders) independent of orientation if the f factor is different for the two peaks. To check for this effect, the powder may be measured at several different angles of incidence. If there is any change in

intensity with angle, then preferred orientation is probably the cause.

A recent paper by Taylor and Craig[138] derived, in the harmonic approximation, a relation between the f factor and the second order Doppler shift, from which the zero-point motion and the Debye temperature could be found quite easily. This is because the two effects measure the mean square displacement and velocity of the atom. The Debye temperature was calculated as:

$$\theta_D = \frac{E}{k_B}\left(\frac{2}{S_t}\right)^{\frac{1}{2}} \tag{38}$$

where

$$S_t = \frac{\ln(f_t)}{(\delta v/c)_t}\text{, and} \tag{39}$$

E is the gamma ray energy,

k_B is Boltzmann's constant,

f_t is the Mossbauer-Lamb factor at temperature T,

$(\frac{\delta v}{c})_t$ is the second order Doppler shift at temperature T.

8. The Source

The source is selected on the basis of its activity, clean spectrum, and lack of hyperfine interactions and line broadening effects. The Iron 57 sources use a natural decay scheme involving the parent Cobalt 57, as shown in figure 15. The source is usually diffused into metal foils such as copper, palladium, stainless steel, platinum, or chromium. The copper source is the simplest, because of its diamagnetic cubic structure and the lack of any secondary X-rays which

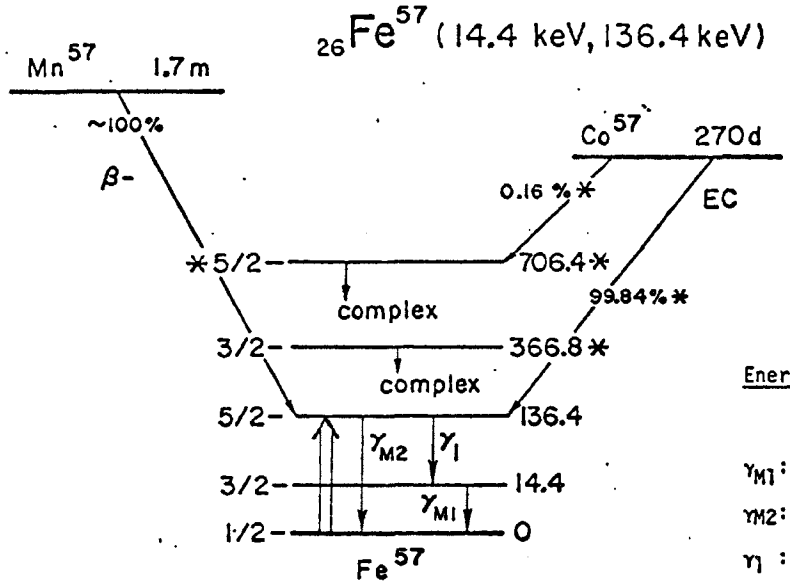

Energies and Intensities

	E_γ		I_{Co} (2)
γ_{M1}:	14.4125	keV (a)	| 9.8|
γ_{M2}:	136.4	keV	|12.6|
γ_1 :	122.0	keV	| 100 |
$K_{\alpha\beta}$:	6.5	keV	| 55 | (b)

Fig. 15. Decay scheme for iron 57. (from Muir et al.[151])

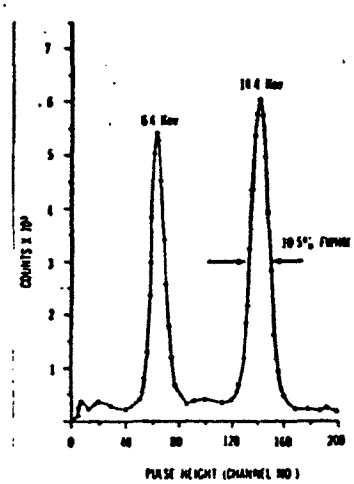

Fig.16. Typical pulse height spectrum for Fe^{57}.

might overlap the gamma ray. It is, however, affected by the atmosphere, forming an oxide which changes the linewidth and isomer shift. The other sources have extra X-rays and/ or the possibility of magnetic broadening at low temperatures. The harder lattices such as chromium give slightly higher f factors. A new source made from CoO has been used because of its uniformity, high activity and high f, but it is in powder form. High temperatures are not possible because of sample holder and decomposition problems, while low temperatures are forbidden because of a magnetic transition. A gamma ray spectrum for Cobalt 57 is given in figure 16.

9. The Absorbers and Filters.

The absorber thickness can be optimized to give the maximum signal-to-noise ratio. This calculation was done by Banks[139] for perovskites like $BiFeO_3$ and $PbTiO_3$. The optimum varies a little with these compounds, but is about 20 mg/cm^2 of sample. This corresponds to about 0.16 mg/cm^2 of Fe^{57}. The results are given in the Appendix III.

There are various filters which can be used to reduce the x-ray count rate for the 6.3 kev x-ray, and these are also used as windows for low temperature dewars and furnaces. A list of some common ones appears in table V, along with their absorption coefficients. Beryllium is also used as a window because of its high transparency to low energy x-rays, but both beryllium and aluminum filters have to be checked for iron impurity which can affect the spectrum.[141]

TABLE V.

ABSORPTION FACTORS FOR VARIOUS MATERIALS

MATERIAL	THICKNESS RANGE (cm.)	ENERGY OF RADIATION (kev)	ABSORPTION COEFFICIENT μ (cm^{-1})	HALF THICKNESS (cm.)
ALUMINUM	0.004 - 0.084	14.4	18.18	0.04
		6.3	190.	0.06
BERYLLIUM	0.004 - 0.14	14.4	1.124	0.17
		6.3	4.190	0.62
CELLOPHANE TAPE	0.006 - 0.051	14.4	1.297	0.53
		6.3	13.985	0.05
FUSED QUARTZ	0.006 - 0.47	14.4	13.	----
		6.3	40.	0.10
MYLAR	0.008 - 0.009	14.4	7.4	0.09
		6.3	11.52	0.06
PLEXIGLASS	0.16 - 0.97	14.4	0.9	0.69
		6.3	15.	0.08
POLYETHYLENE	0.014 - 0.21	14.4	0.829	0.84
		6.3	6.0	0.11
POLYPROPYLENE	0.16 - 0.79	14.4	0.5124	1.34
		6.3	5.5	0.14
TEFLON	0.008 - 0.42	14.4	3.79	0.19
		6.3	39.	0.05

From L. May and D. K. Snediker, Nuclear Instrum. and Methods, 55, 183-188 (1967).

A particularly valuable filter of about .005 inches of brass or copper can be used to filter out almost all of the 14.4 Kev gamma ray and x-rays, so that the background contribution to the spectrum can be measured. A graded shield of aluminum, brass and lead is often used to protect the counter tube from stray radiation that might get in through the aluminum casing rather than the thin window.

10. Detectors.

Gamma rays can be detected using thin crystal scintillation counters, gas filled proportional counters, or lithium-drifted germanium detectors. The thin crystal requirement for scintillation counters is often too stringent and costly to permit the optimum use of this detector. The solid state detectors are very inefficient and are useful only for energy resolution. The gas filled proportional counters are the easiest to use. For Iron 57, the use of a krypton-methane fill gas gives a counter with a very high efficiency for 14.4 Kev gamma rays, because of the proximity of an absorption edge near 14.4 Kev. Other gases are xenon and argon. A thin beryllium window, about 0.010 inches thick and one inch in diameter, determines the detection area.

B. APPARATUS

A diagram of the apparatus is given in figure 17a with a photograph in fig. 17b. Each component of importance will be discussed in terms of design and operation. Before

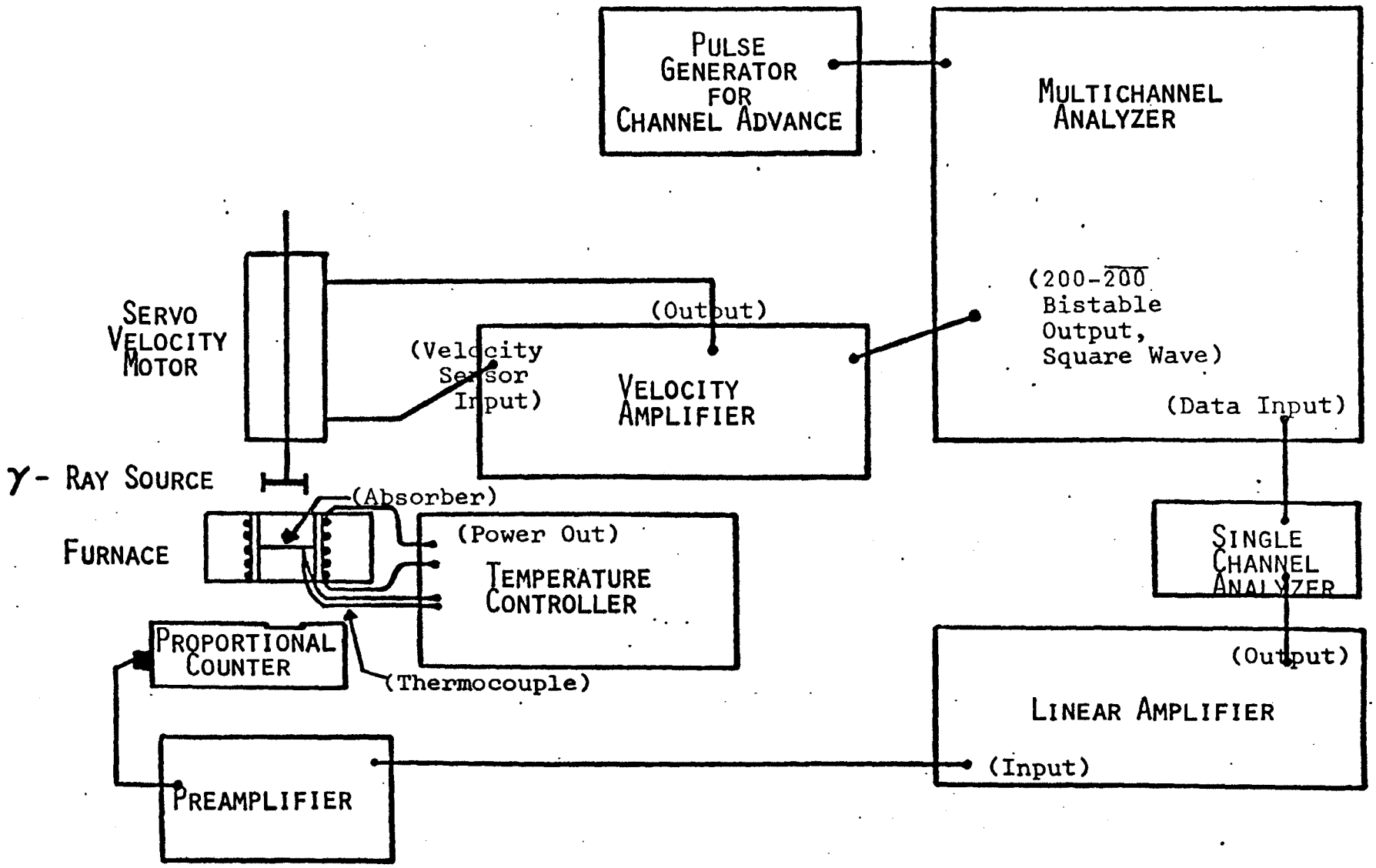

FIGURE 17A. BLOCK DIAGRAM OF MÖSSBAUER SPECTROMETER

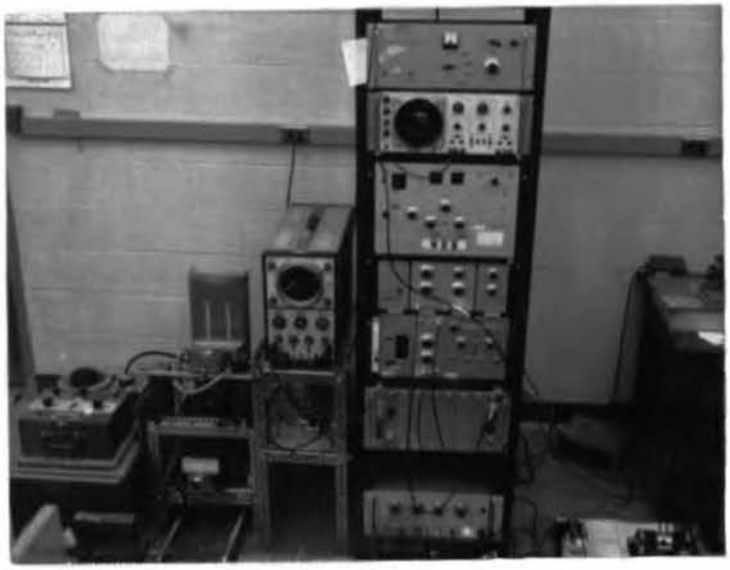

FIG. 17B. PHOTOGRAPH OF MOSSBAUER SPECTROMETER

doing this, it should be mentioned that there are several alternatives to this type of system. The Mossbauer effect is usually observed in what are called the constant velocity, constant acceleration, and cyclic velocity modes, depending on the method used to cause the Doppler shift of the gamma radiation. The constant velocity mode is usually the cheapest to set up, since it requires only a motor, detector, and scaler. The constant velocity is provided by such instruments as lathes, turntables, and gated counting on oscillatory systems such as pendulums, cams, and electromechanical transducers. This mode has the advantage that it requires only a scaler for data accumulation, but the disadvantage of requiring very stable electronics. The other systems use a multichannel analyzer (MCA) to store the data versus velocity. The constant acceleration mode gives a linear scale for the velocity. The synchronization is accomplished by using the last bistable in the channel counting circuit (which can represent a constant acceleration plot) and integrating it to give the corresponding triangular velocity waveform. This is then used to generate a drive signal to an electromechanical transducer.

The other velocity waveforms can be generated in similar fashion, or independently. A method of presenting the data on a linear velocity scale requires that the velocity signal be added to the counts and then stored, using the pulse height analysis feature of the MCA. The

counts are thus stored in channels corresponding to a particular increment of velocity. The problem with this system is that if the velocity is nonlinear, more counts are stored in the channels where the acceleration is low, giving a distorted spectrum. This leads to difficulties in separating irregularities in the velocity from small peaks or splittings in the peaks.

1. The Multichannel Analyzer (MCA).

This miniature computer occupies a central position in the apparatus. A 400 channel RIDL model 24-2 analyzer, with 10^6 memory per channel, is used for data storage. For data accumulation we use the time sequenced scaler mode, which is driven externally by a 3000 cps pulse from a General Radio Pulse Generator (GR 1217c). The analyzer generates a 7.5 cps square wave called the 200-$\overline{200}$ bistable, which is used to generate the drive signal. The pulse height analysis mode of the MCA is used to determine the gamma ray spectrum of the source, and to set the detection system. The analog to digital converter can be operated in coincidence with an independent single channel analyzer. The choice of a separate single channel analyzer allows faster selection of the Mossbauer pulses to be stored and also allows higher intensity sources.

2. The Drive System

This part of the apparatus consists of a signal integrator, summing servo amplifier and electromechanical

motor. The integrator, described in figure 18, consists of a diode clipping circuit, to eliminate the ripple present on the MCA bistable signal, and an operational amplifier with a negative feedback loop, consisting of the integrating capacitor and DC compensating resistors to prevent large drifts in the circuit. The operation of this circuit requires bias adjustment for the inequality of the two clipping diodes and a zero balancing of the inputs of the operational amplifier.

The servo amplifier circuit is based on that given by Wertheim.[142] The circuit is given in figure 19. It contains a summing point, A, and two operational amplifiers with feedback parameters adjusted to give low and high frequency cutoffs to prevent the system from oscillating due to mechanical resonances in the drive motor. The final stage is a unity-gain power amplifier used to give the drive signal enough current for the loudspeaker type motor. A DC feedback loop from the output to the input is used to cut down drift in the summing amplifiers. The theory for the circuit is given by Kankeleit.[143] The adjustment of the circuit requires adjusting of the power amplifier power supplies to compensate for bias inequality in the transistors with zero input. The first operational amplifier must also be adjusted for a slight DC offset, necessary because the motor is operated in a vertical position, to compensate for gravitational forces. The

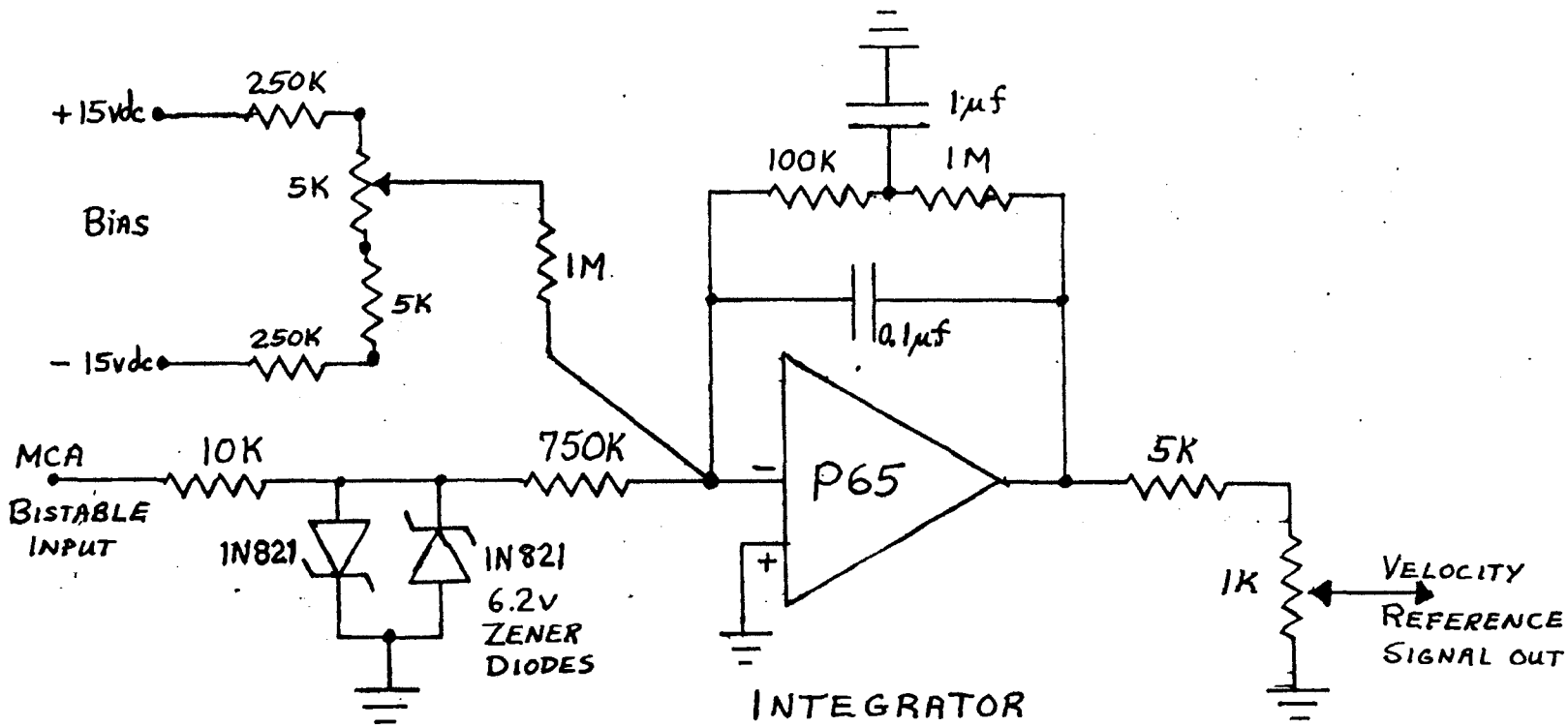

Fig. 18. Velocity Reference Signal Generator Circuit.

(P65 is model number for Operational Amplifier made by Philbrick.)

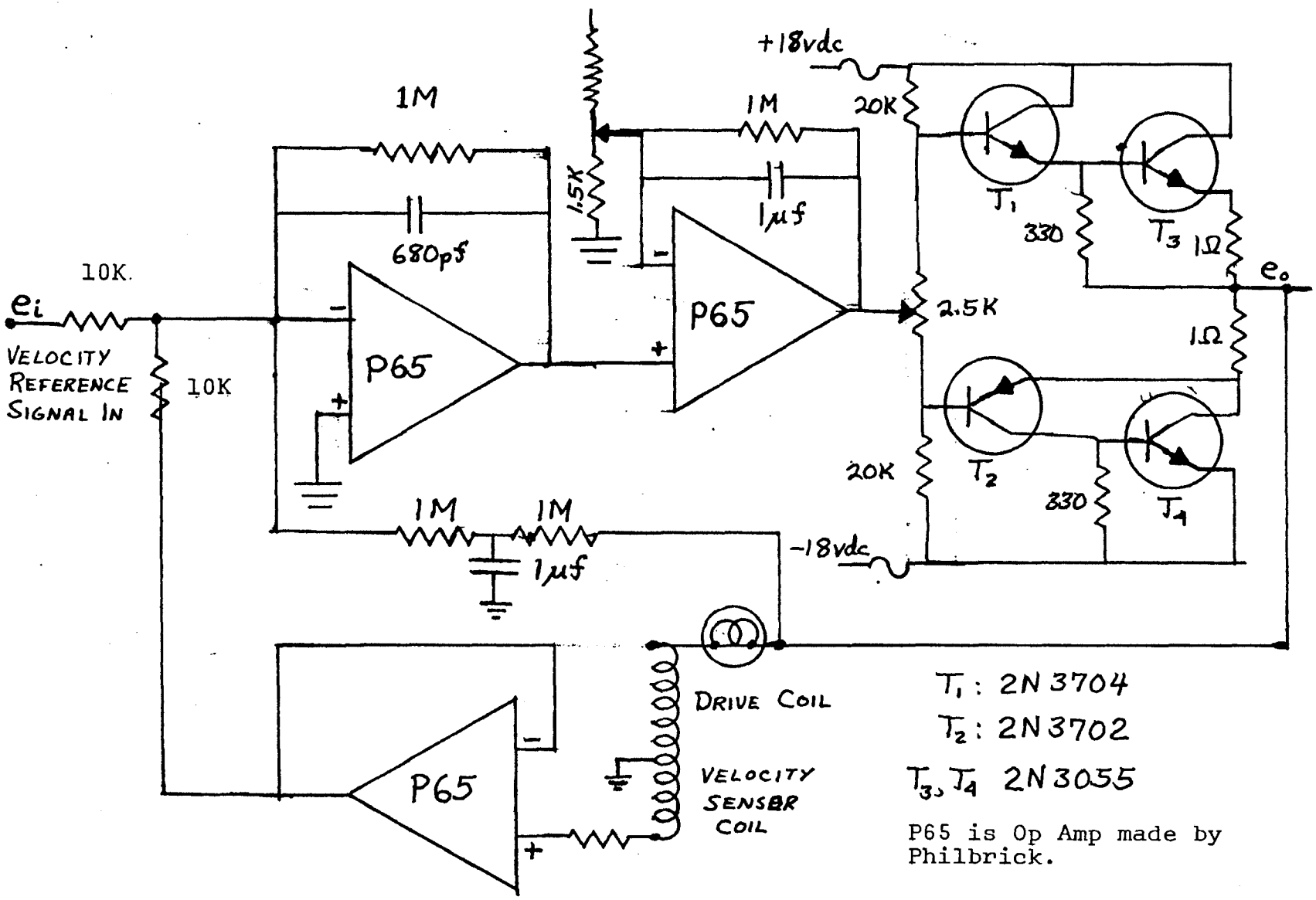

Fig. 19. Summing Amplifier, Power Amplifier and Drive Motor Feedback Circuit.

circuit is not optimized, however, and the gain adjustment would require improvement if high drive levels were needed. Our experiments required only small velocity ranges (from 1 mm/sec to 1 cm/sec), and these do not put large demands on the power amplifier or the feedback circuit to get good linearity. The velocity signals were linear to less than ±4% with slope differences for the up and down sides of the triangle wave of about ±0.6 per cent.

The motor is based on Kankeleit's design and was built by Austin Science Associates. A light bulb is included in the output circuit as a current limiter during periods of overloads to protect the motor coils from burnout. A diagram of the construction is shown in figure 20. The two coils provide the driving force and the velocity feedback signal required in this system. The springs are designed to provide rigid centering of the coils with as light a spring force as possible. The center shaft of the motor is kept light, to reduce the mass mounted on the spring, and the source is mounted on the end of this shaft.

3. The Absorber and Furnace

The absorber consisted of powder placed on a thin foil, mounted horizontally between the source and the detector, in a furnace capable of temperatures up to 700°C. The design of the furnace was based on the requirements for sample size and geometry with respect to the source and detector. The furnace was about two inches thick, with

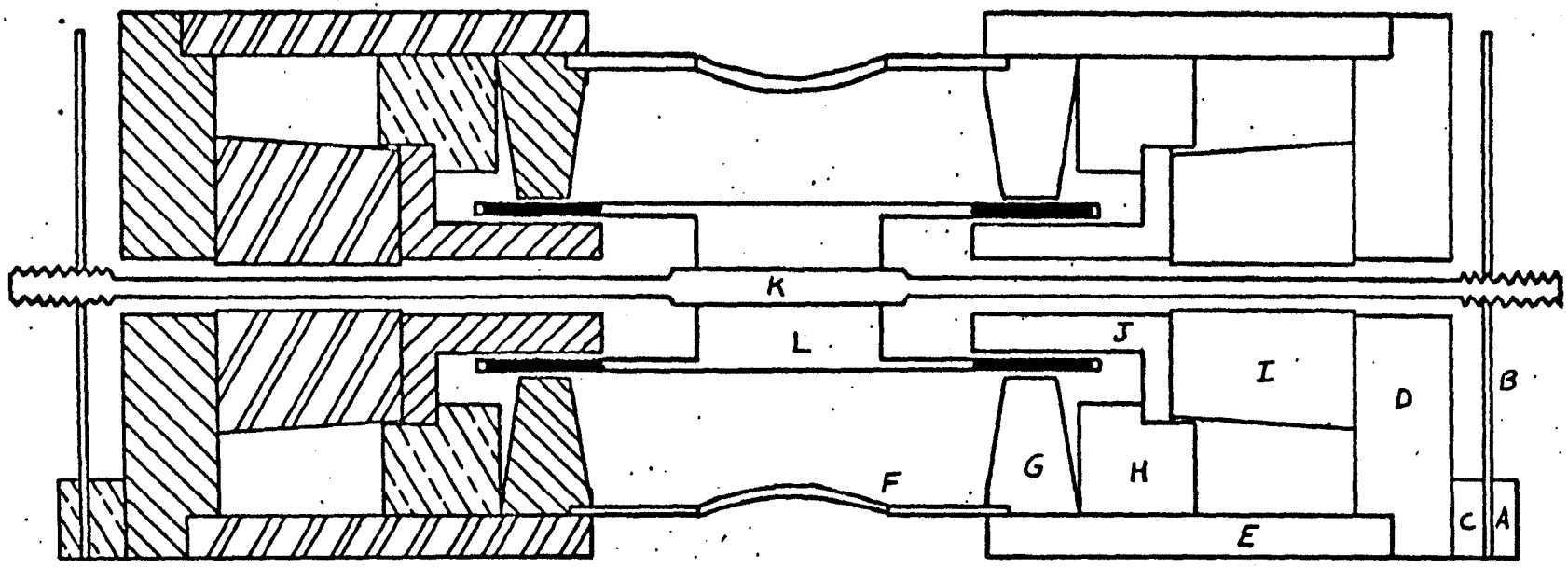

I,E	Alnico V castings
D,G,J	Armco iron
A,C,F,H,K	Aluminum
B	Phosphor bronze
L	Phenolic plastic, reinforced

Fig, 20. Cross-section of Drive Motor (Austin Science Associates, Model K-3).

water cooled copper plates on the top and bottom. There are thin windows of beryllium (.001 in thick, less than 0.14% Fe) in line with the gamma ray path between the source and detector. This keeps the source and detector at room temperature. The furnace is a wire wound ceramic core of about one inch in diameter and two inches in length, contained in a box four inches square. The insulation, about two inches thick, is quartz wool. The furnace is controlled by an API optical meter relay with proportional SCR* driver, and an SCR* control circuit to provide power control proportional to the deviation from the setpoint. It is capable of maintaining ±1°C for 24 hours or more. This circuit is given in figure 21 along with the furnace and sample holder in figure 22. The sample holder is made of Monel metal (66% Ni, 32% Cu), which has high heat conductivity, low oxidation, and low iron content (less than 1.40%). This makes it useful to give even temperature distribution in a small space without chemical reaction or Mossbauer absorption. The foil holding the sample is beryllium foil (.003 in thick, less than 0.14% Fe). The sample holder is suspended inside the furnace from three ceramic standoffs to provide thermal insulation from the outside. The sample temperature was monitored with a Chromel-Alumel thermocouple measured with a potentiometer. The sample size was restricted to about

---

* Silicon Controlled Rectifier.

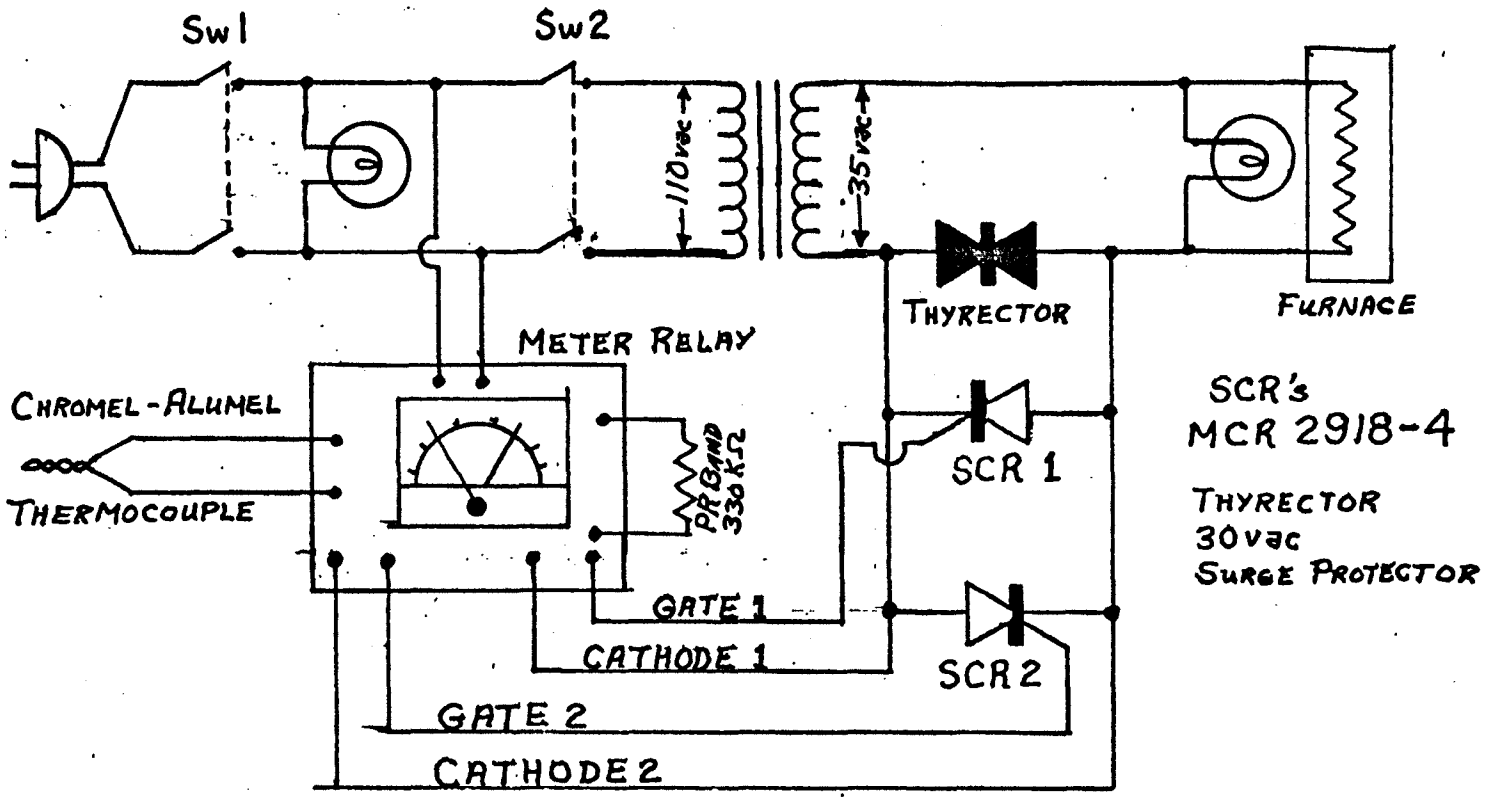

Fig. 21. Furnace Temperature Controller Circuit (Meter Relay is API 603K SCR driver).

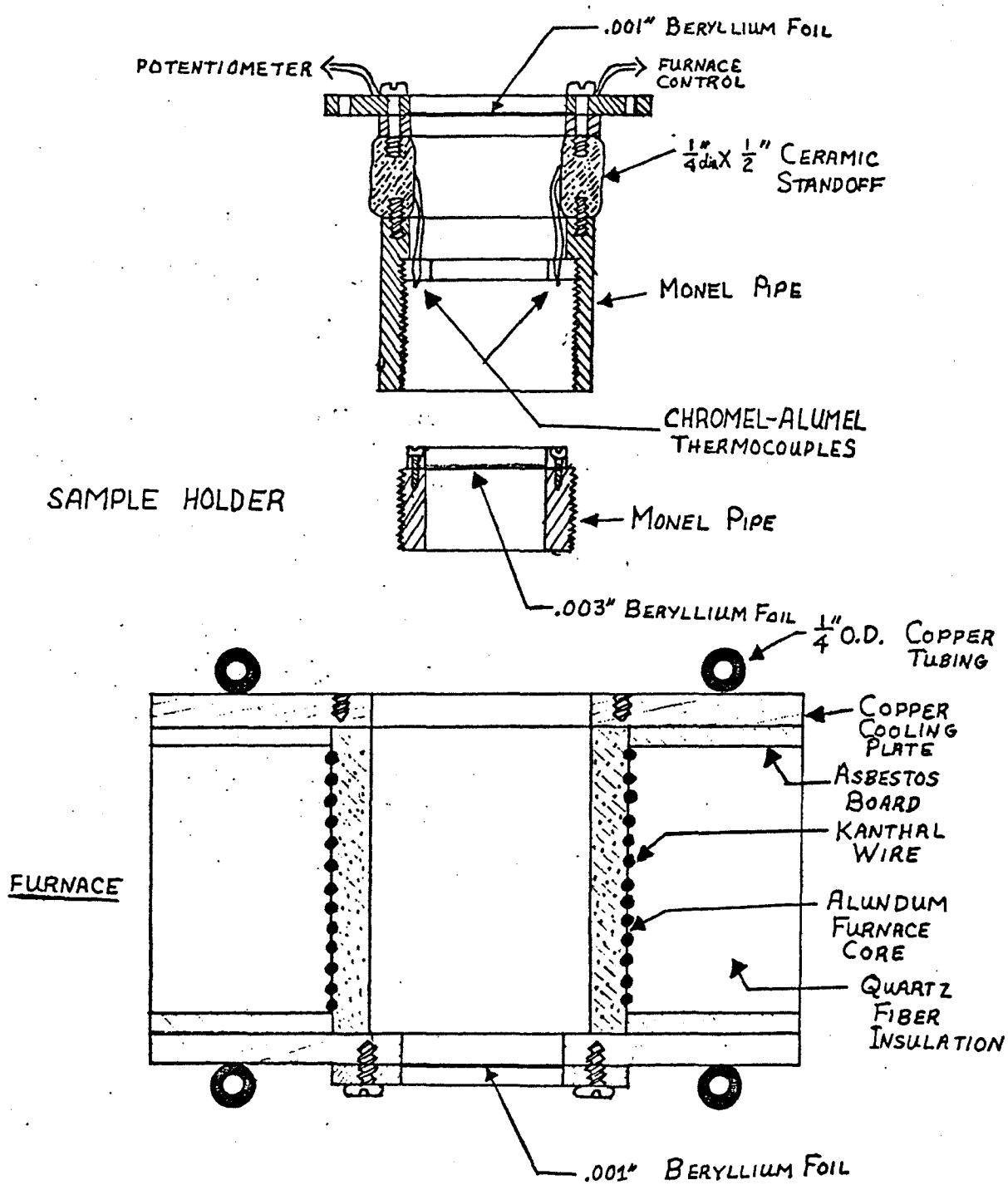

Fig. 22. Diagram of the Furnace and Sample Holder.

three-quarters of an inch in diameter, giving about 6° angle deviation from the normal. The source-sample-detector geometry, chosen to minimize cosine broadening, is shown in figure 23. Cosine broadening due to the spread of velocities obtained from finite source and absorber size has been discussed by Banks[139] and by Spijkermann, et al.[146] It is given by:

$$\Delta V = V(1-\cos\theta) = \frac{\Gamma}{n} \qquad (40)$$

where V is the velocity of motion,

θ is the gamma ray with respect to the direction of motion,

$\frac{\Gamma}{n}$ is fractional broadening of Γ.

The smaller the angle, the smaller the effect, but the count rate is also reduced. Another effect is due to the larger solid angle when the source is closer to the detector, which means that more counts will be observed on one half of the spectrum. In the triangular wave mode, this can be corrected by adding the two spectra to get a cancellation of the effect. With our small velocity this was not a problem.

4. The Detector System

The detector was a xenon-methane gas-filled proportional counter with a one inch diameter, .010 inch thick, beryllium window. The detector electronics used a Hamner N375A preamplifier and either an RIDL 30-19 RC pulse-shaping

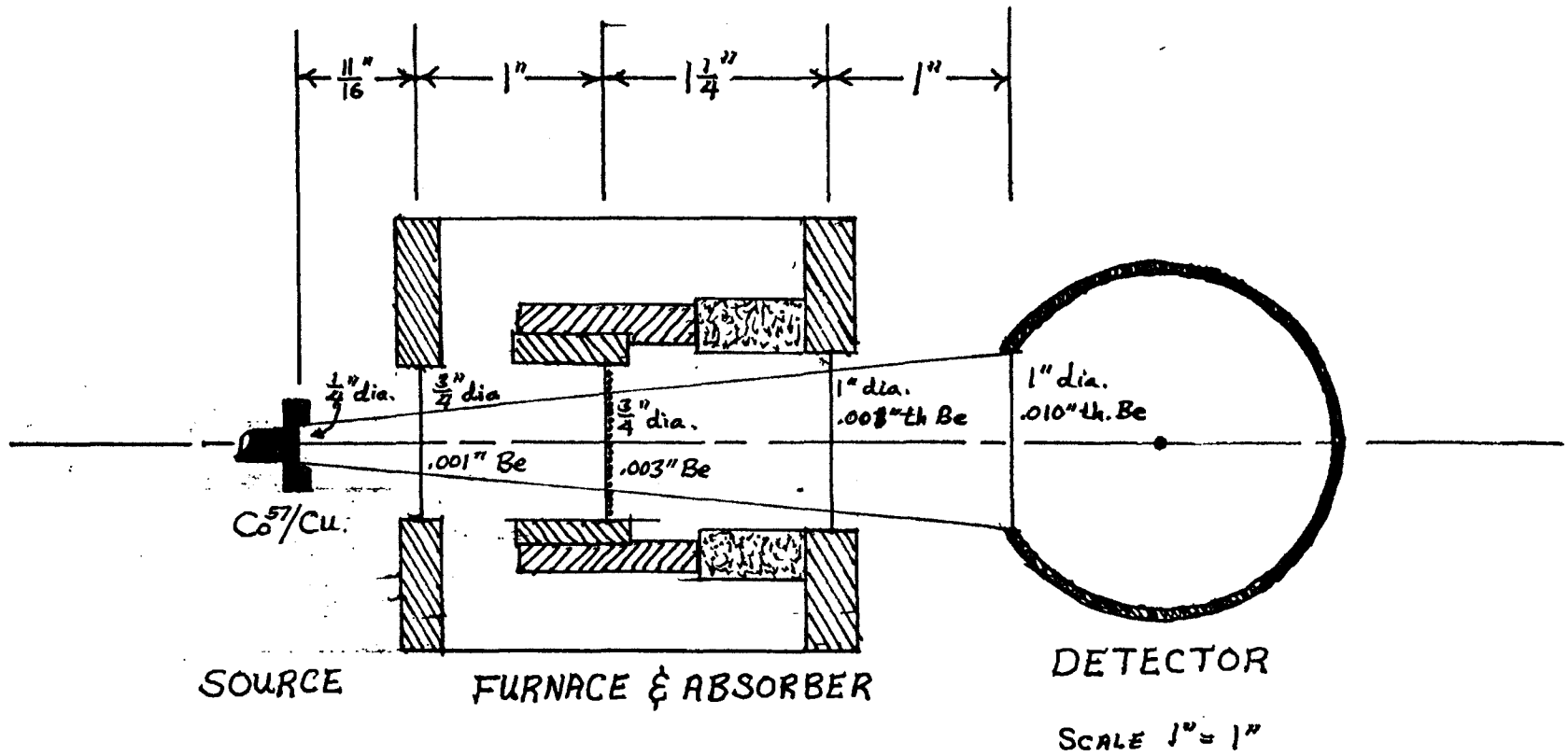

Figure 23. Gamma-ray Geometry for the source, absorber in furnace and detector.

Linear Amplifier or a Detectolab Al-D Delay line pulse-shaping Linear Amplifier.

The pulses were selected using the pulse-height discriminators of either the MCA's analog-to-digital converter, or a separate RIDL 33-14A single channel analyzer, operating in delayed coincidence with the analog-to-digital converter. The latter set-up allowed higher count rates and more accurate pulse selection. The windows for the gamma ray peak were set using the pulse height analysis mode of operation of the MCA to observe the whole spectrum, and then setting the upper and lower levels of the discriminator of the analog-to-digital converter to bracket the desired peak. In the delayed coincidence set up, the pulse height spectrum was run in anticoincidence. Then the window and threshold of the single channel analyzer were set to bracket the desired peak, using the coincidence circuit to prevent counts from storing that were not passed by the single channel analyzer. Once the windows were set, the pulses were directed to the data input for the timed sequence scaler mode of operation of the MCA.

The detector tube used a potential of 2050 volts dc supplied by a Keithley 242 high voltage power supply. A 10^7 count capacity RIDL 49-30A scaler with a 0-60 minute timer was used to measure the total count rate being stored in all 400 channels of the MCA. This was used to determine drifts in SCA settings, absorber thicknesses, and background

counting rates (using a .005 inch piece of brass foil).

5. Data Readout

The data stored in the MCA was read out on one inch wide paper tape using a Tally 420PR perforator. This tape contained the channel number (0-399 channels) and a six digit number representing the number of counts in that channel. Ordinarily these tapes were converted to punched cards compatible with the UMR IBM 360-model 50 computer. The data could then be processed by computer curve fitting programs.

6. Data Processing.

A computer program provided by NBS called PARLORS (for parabola-Lorentzian) was used to give a least-squares fit to a linear approximation of the Lorentzian line shape. The program was capable of fitting up to 20 separate peaks, and resolving peaks that were separated by about three-fourths of the half width at half maximum. A background parabola was also fitted to account for nonlinearities and the inverse cosine effect. The program (described in NBS publications),[147] is described and listed in appendix I. The data and the computed fit are plotted on one plot for comparison. A residual error plot could be used to show any missed peaks or bad fits. This program takes about 30 seconds for each data set of 200 channels with two peaks to be fitted.

A "beryllium" correction was added to the program after

it was noticed that there was an iron impurity peak, causing about 1% dip, which was present with just a source and detector. It was later found that the cause was an impure aluminum foil filter between the detector and furnace. The correction consisted of subtracting a peak of the magnitude of the impurity effect. It was found that the experimental magnitude was not easily determined and that the magnitude affected the relative intensity of the peaks in the normal pattern.

Another program provided by Bell[148] called LORLSF has constraints for equal linewidths and peak height, and it has been used when lack of resolution caused PARLORS to fail to converge. LORLSF uses iteration of a Taylor's series expansion of the Lorentzian, where the parameters are adjusted with reference to their calculated errors. The program is listed in appendix II.

7. Velocity Calibration.

The velocity scale of the spectrum was determined by using the inner peaks of a soft iron foil which have a separation of 1.67 mm/sec. The center of gravity and relative separations of the two mirror spectra were used to determine the linearity and relative slopes of the triangle wave, and were used to correct the isomer shifts of the data to iron. See figs. 24 and 25.

8. The Experiment.

The experiment consisted of a 6 to 8 hour run,

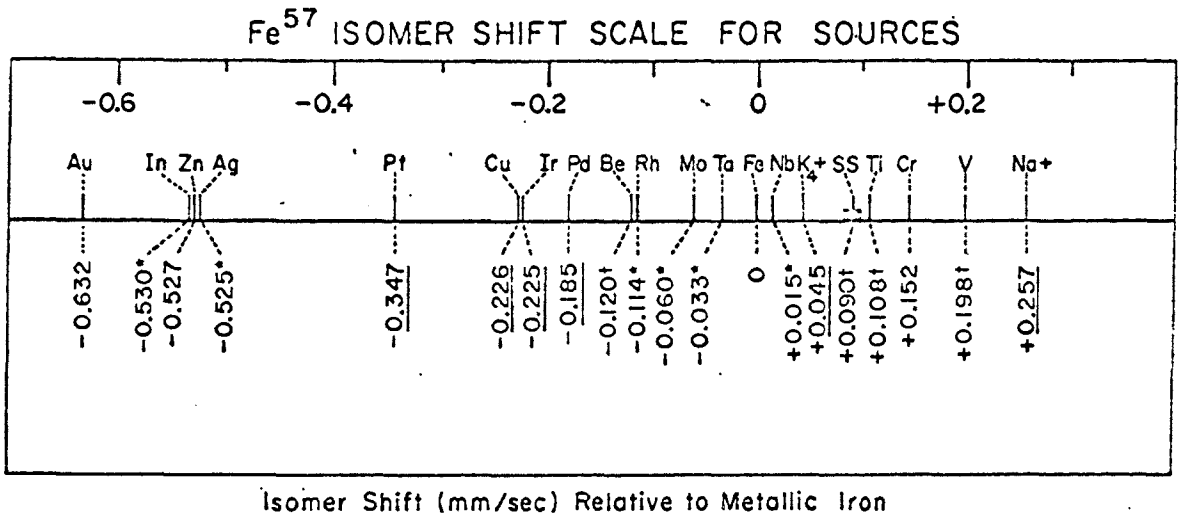

Fig. 24. (from Muir et al.[151])

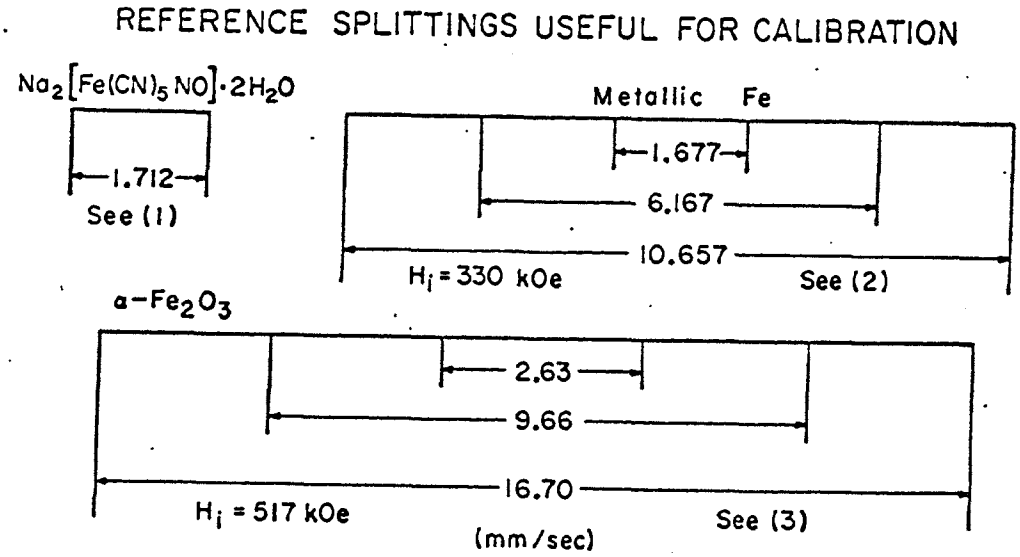

Fig. 25. (from Muir et al.[151])

accumulating about 300,000 counts per channel. The count rate was checked before and after each run, with a check of the background count rate between each run. The temperature was changed in increments of 3 to 5 degrees except near room temperature, where 10 to 20 degree increments were used. The furnace was allowed to stablize over a period of a half hour, during which the previous data were read out. The gamma ray energy pulse height spectrum was checked periodically, especially if drift was indicated by the count rate. Changes were avoided as much as possible because of the unknown effect on the area of the spectrum. For this reason, the window was set to include as much of the 14.4 gamma ray as possible without overlap from the x-rays, with the hope of keeping the signal to noise ratio constant. Under these conditions, slight drifts in the electronics only affected the tails of the energy distribution. Due to resolution problems with the linear amplifier and preamplifier, this situation was not always optimal.

C. THE SAMPLES

The samples were prepared using techniques developed by Mrs. Lamar of the Materials Research Center at UMR. Because enriched iron containing 80-90% Fe 57 was used, special techniques were devised to prepare small samples to conserve the enriched iron used. The oxides $Fe_2^{57}O_3$, Bi_2O_3, PbO, TiO_2, ZrO_2 were mixed in stoichiometric

proportions for several hours using a mechanical mortar and pestle. The mixtures were then wrapped in platinum foil and placed in a morganite crucible containing the natural iron mixture of the same composition and surrounded by this mixture. The covered crucible was then placed in a furnace and sintered at temperatures and times necessary for the particular compound. The resulting powders were checked using a Siemen's x-ray diffractometer for impurity phases and completion of reaction. The sample was made into slurry using acetone and spread evenly on the beryllium foil, using the vibration of a Vibromet polishing wheel and hand motions. No reaction with the beryllium foil was noticed. The beryllium did discolor slightly on both the sample and the opposite side of the foil due to the high temperature oxidation, but the powders did not become fused to or appear to be reacting with the Be. It would not be expected that reaction could take place at temperatures below 600°C in these compounds.

IV. EXPERIMENTAL RESULTS

The results are presented here in the form of graphs and tables. The materials investigated were natural iron, and three compounds containing about 5% $BiFeO_3$ (prepared using enriched iron 57); $PbZrO_3$, 80% $PbZrO_3$-20% $PbTiO_3$, and 70% $PbZr\ O_3$-30% $PbTiO_3$. The first compound was antiferroelectric and the others ferroelectric.

A. IRON CALIBRATION

For calibration, natural iron foil supplied by the New England Nuclear Corp. was used. It was .001 inches thick with no specifications as to purity. Some foils had rust spots on them, but efforts were made to select areas without rust visible. The expected ferromagnetic six line spectrum was obtained. The intensity ratios of the peaks were not checked, but appeared to be such that the second and fifth peaks were more intense than normal for unmagnetized iron. This would indicate that the foil was at least partially magnetized. The peak intensity ratios for unmagnetized iron are 3:2:1:1:2:3, while for magnetized iron they are 3:4:1:1:4:3. Dash, et al.[149] report obtaining values of 3:3.2:1:1:3.2:3. In our best determination, the four inner peaks had ratios of 2.35:1:1:2.35. The calculation of f was made with both of the published intensity ratios, and an average value was used to establish that no appreciable losses existed in the apparatus.

Only the two innermost peaks were used to calibrate

the velocity, because the velocity range was restricted to about ±2.0 mm/sec, which included only these peaks. The spectrum is shown in fig. 26. The data are shown for three different measurements in table VI. One of these data sets was made after the source of a small iron impurity peak, an aluminum foil filter, was found and removed. This latter set of data does not include the errors introduced by making the beryllium-iron correction used to remove the effects of the iron impurity.

The linewidth of the iron spectrum peaks, obtained with data using the beryllium correction, was about 1.55 times the natural linewidth. The sample run after the iron impurity was removed had a linewidth of 1.33 times the natural linewidth. Typical values for copper source and iron foil are about 1.3 times the natural linewidth.[150]

The calibration of the iron spectrum consisted of assigning the velocity of 1.677 mm/sec to the splitting of the two peaks and the velocity of -0.226 mm/sec to the center of gravity of the two peaks. The calibration constants were found to vary between the two mirror image spectra obtained using the triangular drive waveform. These are tabulated in table VII. The discrepancy from the average, for velocity calibration using the isomer shift, gave a measure of the nonlinearity of the waveform. The result from the peak splitting gave a measure of the difference in slope between the two spectra. The 4.2%

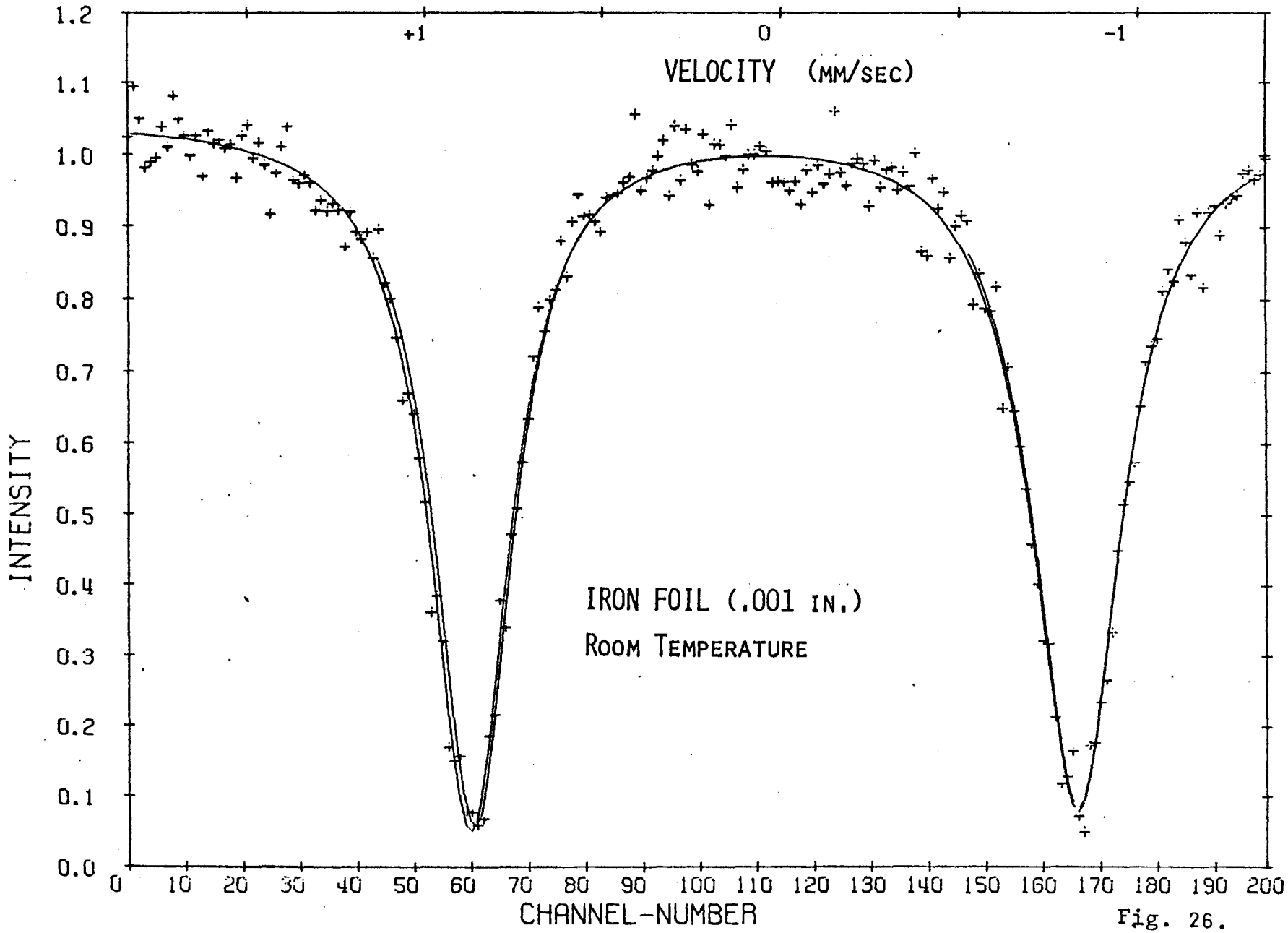
VELOCITY (MM/SEC)
+1
0
-1
INTENSITY
1.2
1.1
1.0
0.9
0.8
0.7
0.6
0.5
0.4
0.3
0.2
0.1
0.0
IRON FOIL (.001 IN.)
ROOM TEMPERATURE
0
10
20
30
40
50
60
70
80
90
100
110
120
130
140
150
160
170
180
190
200
CHANNEL-NUMBER

Fig. 26.

TABLE VI.

DATA FROM ROOM TEMPERATURE IRON SPECTRA

SAMPLE		POSITION AND LINEWIDTH				ISOMER	QUADRUPOLE	AREA	f_1	f_2	f_3
NATURAL IRON		x_1	Γ_1	x_2	Γ_2	SHIFT	SPLITTING	(arb.)	Un-Pol.	Pol.	Avg.
		(VELOCITY WITH RESPECT TO IRON IN mm/sec.)									
Be	I(L)	+.854	.131	-.823	.146	+0.015	1.680	8.335			
Corr.	(R)	+.828	.140	-.849	.140	-0.008	1.661	8.192			
									0.55	0.92	0.74
Be	II(L)	+.848	.140	-.829	.136	+0.008	1.688	8.298			
Corr.	(R)	+.827	.137	-.850	.139	-0.010	1.671	8.321			
No Be	III(L)	+.847	.127	-.830	.134	+0.006	1.697	7.080			
Corr.	(R)	+.828	.131	-.849	.128	-0.010	1.677	6.908	0.50	0.84	0.67

TABLE VII.

CALIBRATION FACTORS FROM NATURAL IRON

	ELECTRIC QUADRUPOLE SPLITTING			ISOMER SHIFT		
	K(L)	K(R)	K(Avg.)	K(L)	K(R)	K(Avg.)
I.	0.01580	0.01598	0.01589	0.01690	0.01527	0.01608
II.	0.01572	0.01589	0.01580	0.01641	0.01514	0.01587
III.	0.01564	0.01583	0.01574	0.01625	0.01514	0.01569
Avg.	0.01572	0.01590	0.01581	0.01652	0.01518	0.01585

K = 0.01583 mm/sec/channel ΔSlope = ±0.0057 ΔNonlinearity = ±0.042

variation in isomer shift velocity calibration gives the nonlinearity of the drive. The slopes were found to vary by about 0.6%. An exaggerated sketch of the distorted velocity waveform is given in fig. 27. The calibration constant K is 0.01583 mm/sec/channel.

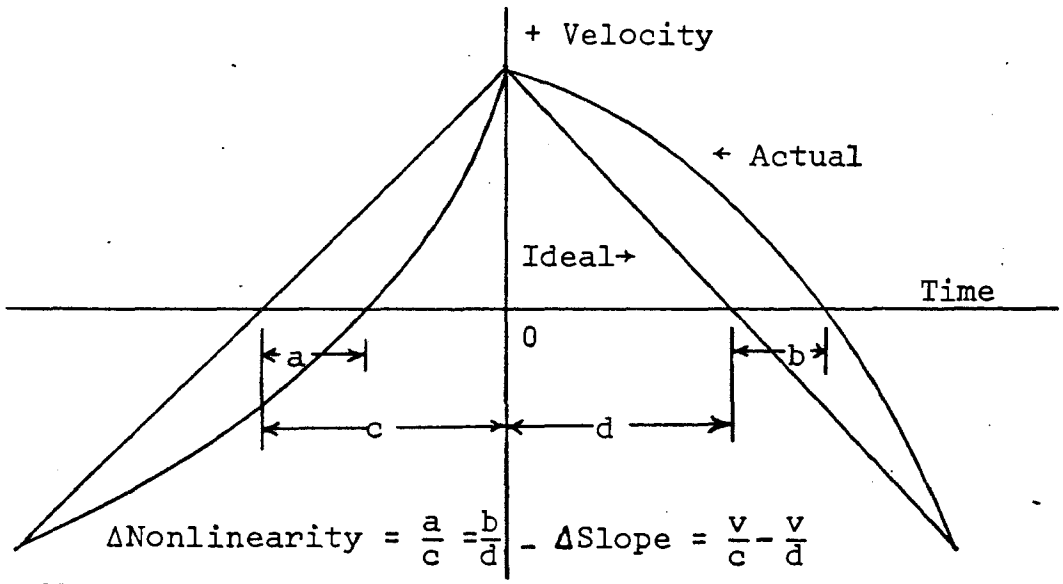

Fig. 27. Representation of errors in velocity signal.

The f factor was determined using equation 37, since the value of $n\sigma_0$ ($n\sigma_0$ = 9.57) is in the region where the G correction is larger than the F correction. This made $F(n\sigma_0 f_a)$ converge faster than $G(n\sigma_0 f_a)$. The results are summarized in table VI. An average value for f is 0.70 ±0.15, roughly equal to reported values which range from 0.6 to 0.8.

B. 95% $PbZrO_3$-5% $BiFeO_3$.

This sample was prepared using the techniques described earlier. It was sintered at 1100°C for 1.5 hours and then air-quenched. The iron was 81.55% iron 57. The resulting

TABLE VIII.

DATA FROM ROOM TEMPERATURE SPECTRA OF SAMPLES

SAMPLE COMPOSITION		POSITION AND LINEWIDTH x_1	Γ_1	x_2	Γ_2	ISOMER SHIFT	QUADRUPOLE SPLITTING	AREA (arb.)	f_1 Two Peak	f_2 Four Peak	f_3 Inhomogeneous
		(Velocity with respect to iron in mm/sec.)									
95 $PbZrO_3$ 5 $BiFeO_3$	I(L)	.627	.374	.162	.524	+0.395	0.466	7.575	.096	--	0.66
	(R)	.603	.354	.121	.440	+0.362	0.481	6.443			
	I(LA)	.519	.280	-.201	.280	+0.384	0.720	4.979	--	0.12	0.44
	(LB)	.279	.280	.039	.280		0.240				
	(RA)	.501	.282	-.219	.282	+0.376	0.719	5.034			
	(RB)	.261	.282	.021	.282		0.240				
No Be Corr.	II(L)	.640	.199	.183	.307	+0.414	0.456	3.800	.085	--	0.40
	(R)	.629	.251	.147	.418	+0.388	0.482	5.476			
$PbZr_{.8}Ti_{.2}O_3$ + 5%$BiFeO_3$	(L)	.691	.262	.119	.244	+0.405	0.572	7.570	.194	--	0.64
	(R)	.657	.252	.083	.250	+0.370	0.574	7.494			
$PbZr_{.7}Ti_{.3}O_3$ + 5%$BiFeO_3$	(L)	.702	.255	.100	.247	+0.401	0.601	2.920	.136	--	0.42
	(R)	.675	.272	.065	.243	+0.370	0.610	3.175			

spectrum for the "beryllium" correction case is shown in fig. 28, and for the no-impurity case in fig. 29. The room temperature parameters for these two runs are listed in table VIII.

The thickness of the sample was determined from the measured absorption of gamma rays and the calculated absorption coefficients (see Appendix III). The thickness of the sample was .00857 gm/cm^2. This is equivalent to $n\sigma_o$ = 1.49 for Iron 57 in the sample. The resulting f factor was 0.096 for the "beryllium" correction case, 0.085 for the no-impurity case and 0.12 for the four peak "beryllium" correction case. After considering inhomogeneous broadening the value of f is increased to .64, .40 and .44 respectively for the above cases. These gave Debye temperatures in the range of 190°-280°K.

The linewidth with Be correction was 4.4 times the natural linewidth. The factor was 3.0 without iron impurity and 2.9 with the four peaks and Be correction.

The isomer shift at room temperature gave an ionicity of 49% for the "beryllium" impurity case and 68% for the no-impurity case. The empirical relation of Bhide, et al.[113] (fig. 12) was used, so that large changes in ionicity occur for small changes in isomer shift. The results of Lyubimov, et al.[124] indicate an ionicity 43% for zirconium in $PbZrO_3$. The electric field gradient for the two peak case was $2.12 \times 10^{16} \frac{V}{cm^2}$. For the four peak case, they were 1.08×10^{16} and $3.23 \times 10^{16} \frac{V}{cm^2}$. A ratio of 1:3 was assumed for the

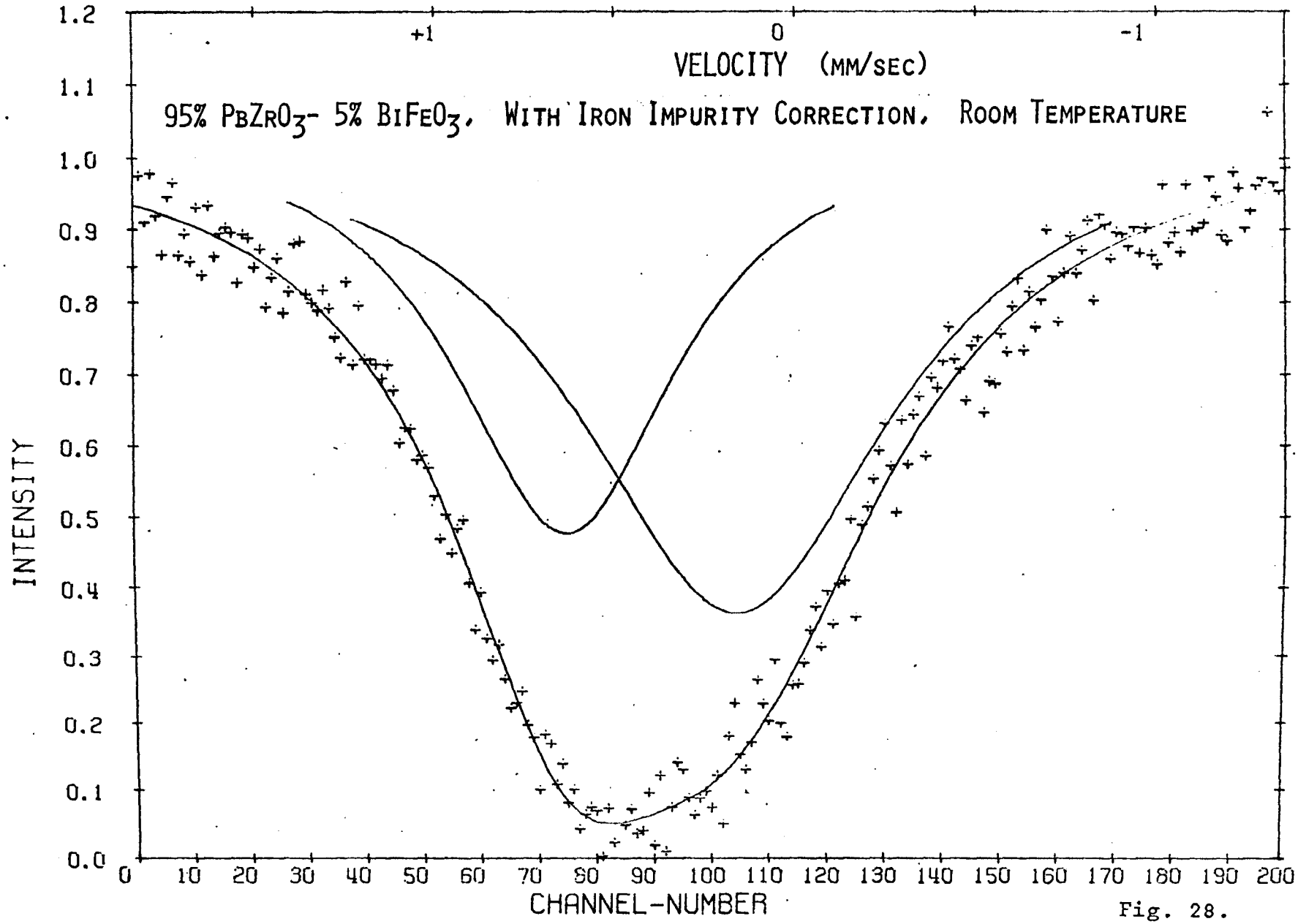
95% PbZrO3- 5% BiFeO3, With Iron Impurity Correction, Room Temperature
VELOCITY (mm/sec)
+1
0
-1
INTENSITY
1.2
1.1
1.0
0.9
0.8
0.7
0.6
0.5
0.4
0.3
0.2
0.1
0.0
0
10
20
30
40
50
60
70
80
90
100
110
120
130
140
150
160
170
180
190
200
CHANNEL-NUMBER

Fig. 28.

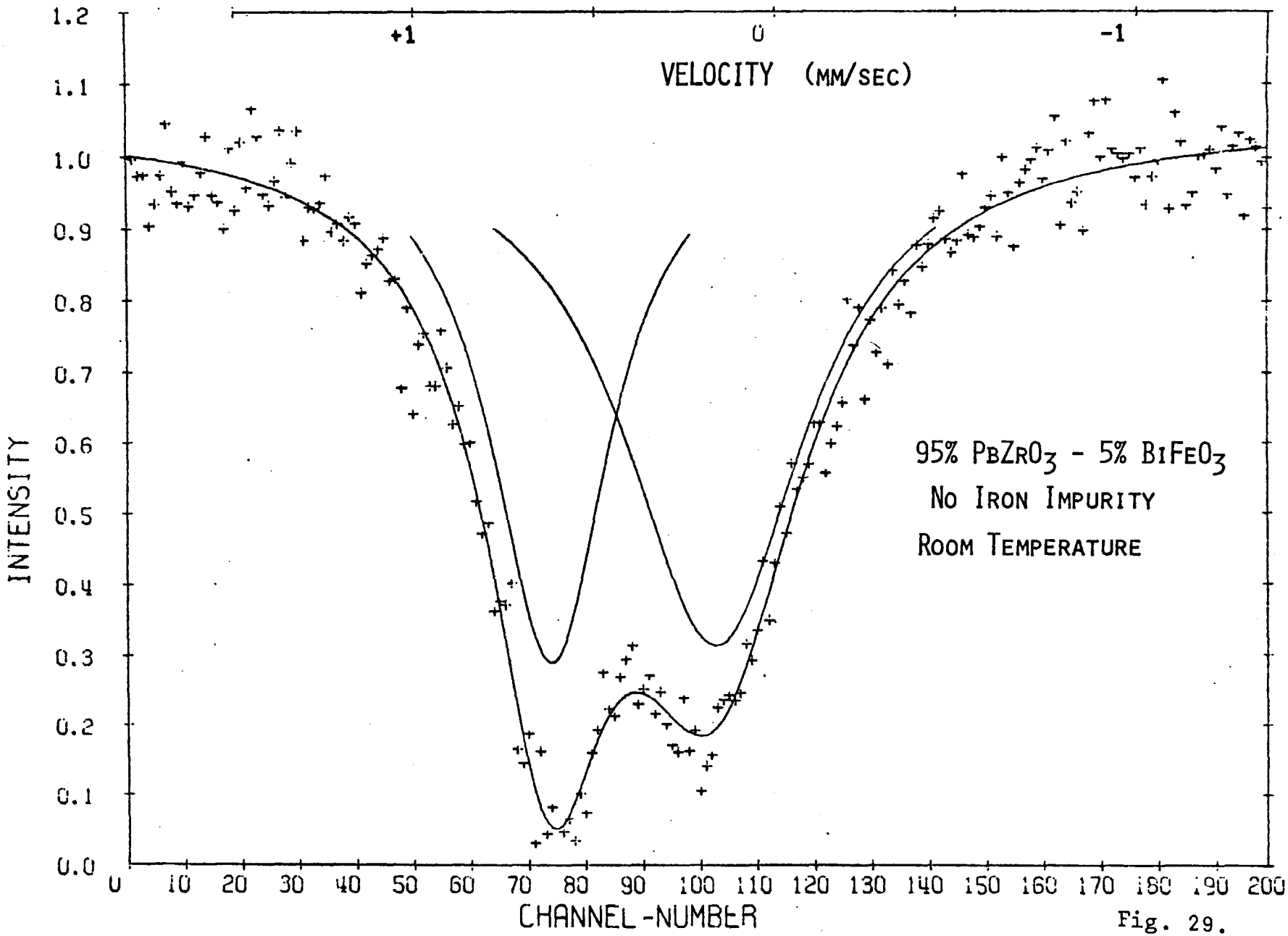
VELOCITY (MM/SEC)
+1
0
-1
INTENSITY
CHANNEL-NUMBER
95% PbZrO3 - 5% BiFeO3
No Iron Impurity
Room Temperature

Fig. 29.

splitting (see Appendix V).

The effect of temperature on the peak area in fig. 30 was to cause a broad dip between 170° and 190°C. These data were taken as the sample was cooling. A possibility of two dips in this range was indicated by the shoulder in the dip. These would correspond to the presence of two phase transitions in $PbZrO_3$. The dielectric constant as a function of temperature, in fig. 31, showed a transition at 200°±5°C, with a Curie temperature of 150°C obtained from the dielectric constant behavior above the transition temperature. There was also a slight increase in the dissipation factor at 165°C, below the effect of the 200°C transition. This could indicate the second transition from a ferroelectric to an antiferroelectric state. It occurred both upon heating and cooling of the sample, with about a 10°C hysteresis.

The electric quadrupole splitting versus temperature is shown in fig. 32. The quadrupole splitting decreased rapidly at 200°C, to indicate a phase transition from a polar to non-polar state. There was a slight irregularity at about 160°, which might be an indication of the second phase transition mentioned earlier. There was a residual splitting above 200°C, due to electric field gradients generated by the differently charged B ions randomly occupying the B sites of the lattice.

The isomer shift versus temperature is shown in fig. 33. There was a slight break at about 190°C, which may be

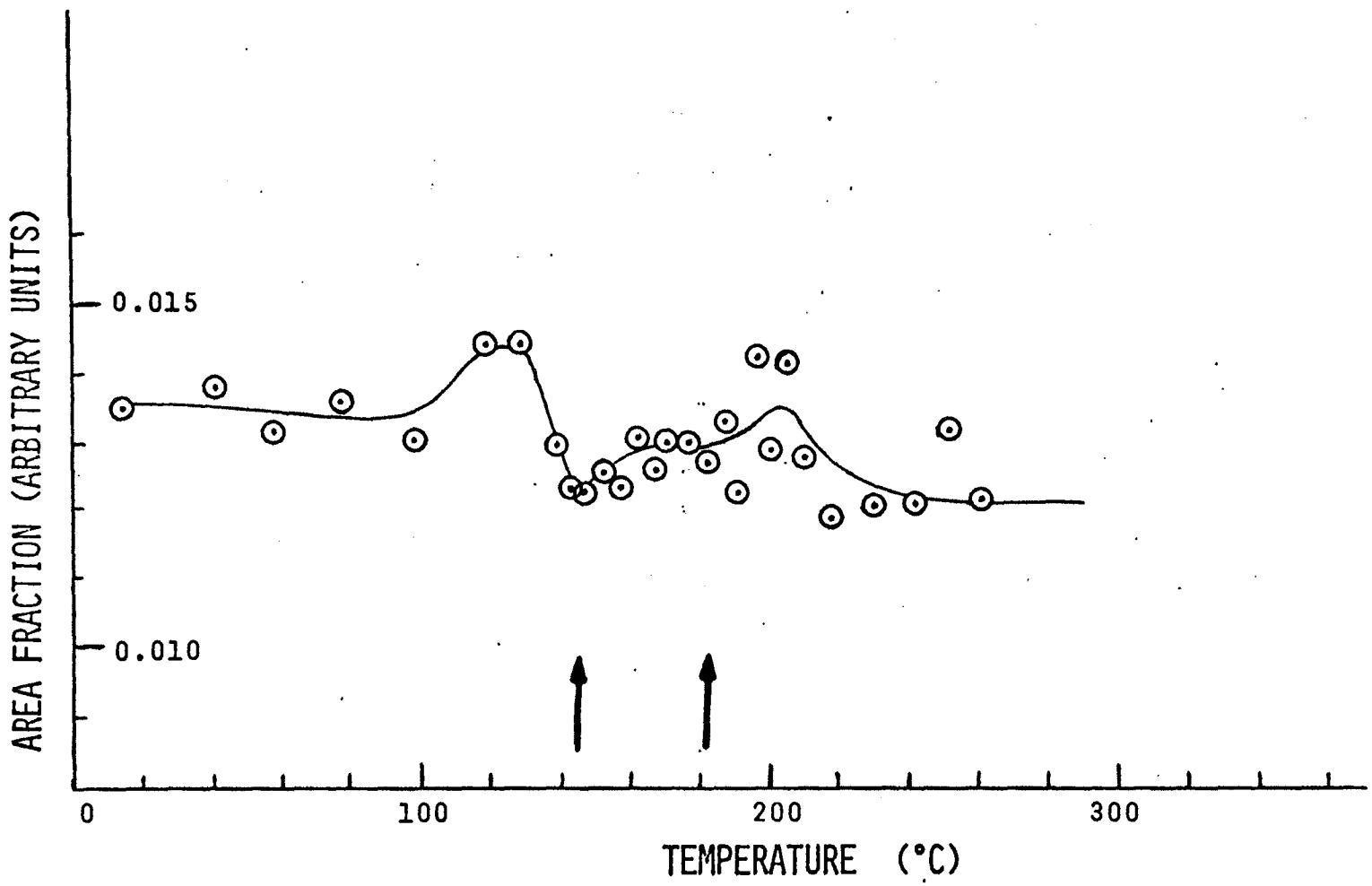

FIG.30. Area fraction as a function of temperature in Mossbauer studies of 95% $PbZrO_3$- 5% $BiFeO_3$.

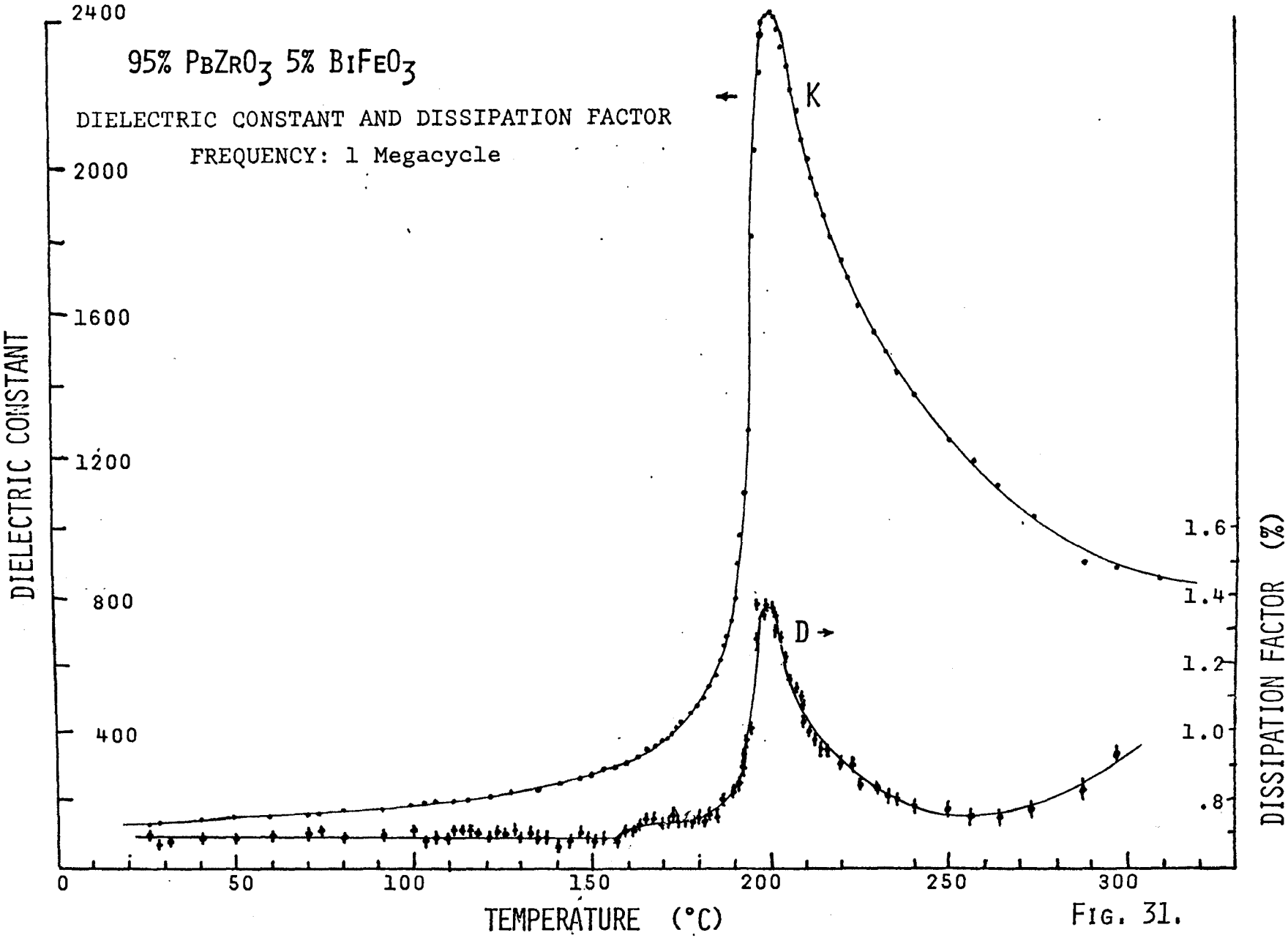
95% $PbZrO_3$ 5% $BiFeO_3$
DIELECTRIC CONSTANT AND DISSIPATION FACTOR
FREQUENCY: 1 Megacycle
K
D
DIELECTRIC CONSTANT
2400
2000
1600
1200
800
400
DISSIPATION FACTOR (%)
1.6
1.4
1.2
1.0
.8
0
50
100
150
200
250
300
TEMPERATURE (°C)

FIG. 31.

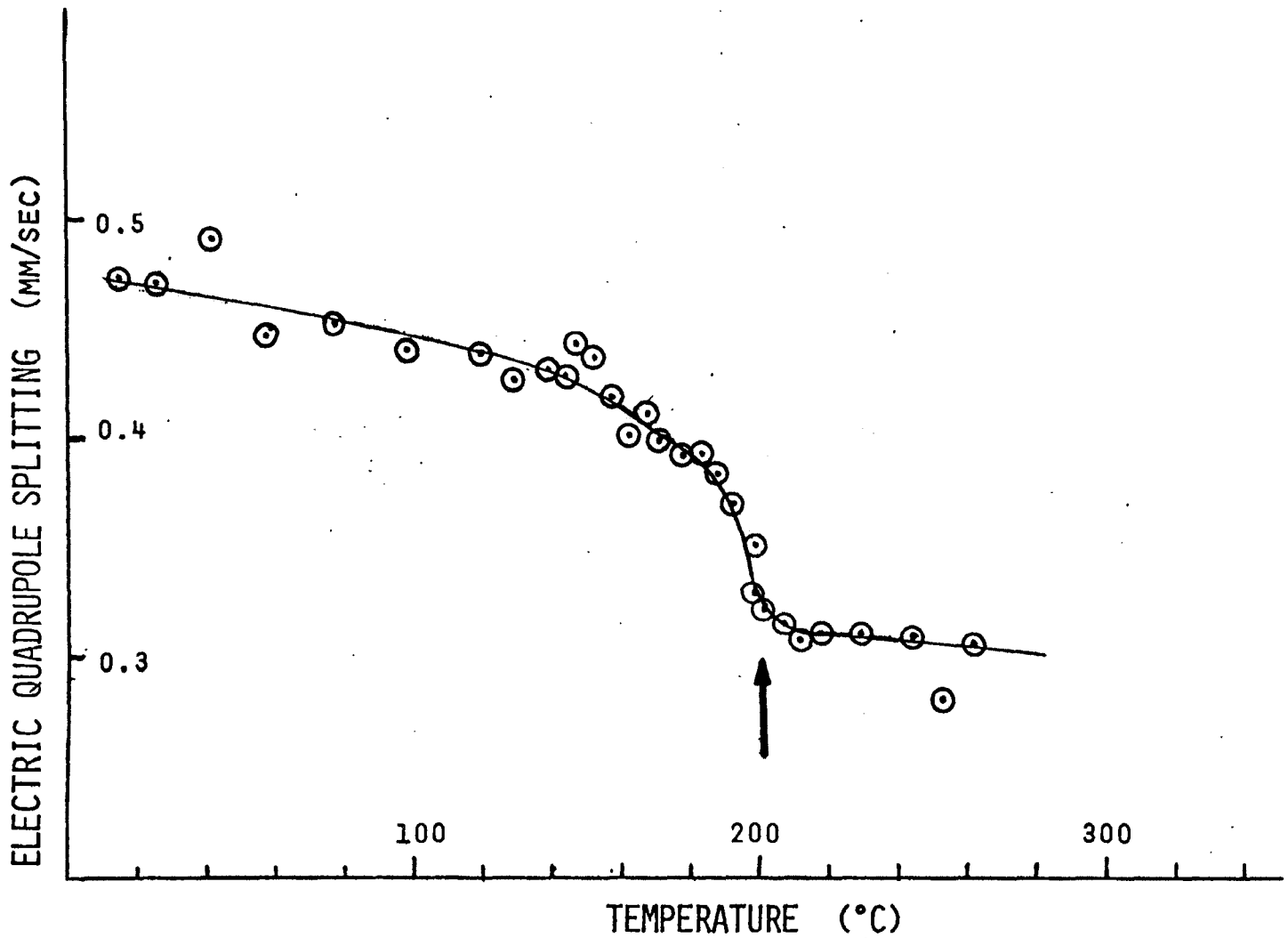

FIG. 32. Electric quadrupole splitting due to the electric field gradient as a function of temperature in Mossbauer studies of 95% $PbZrO_3$- 5% $BiFeO_3$.

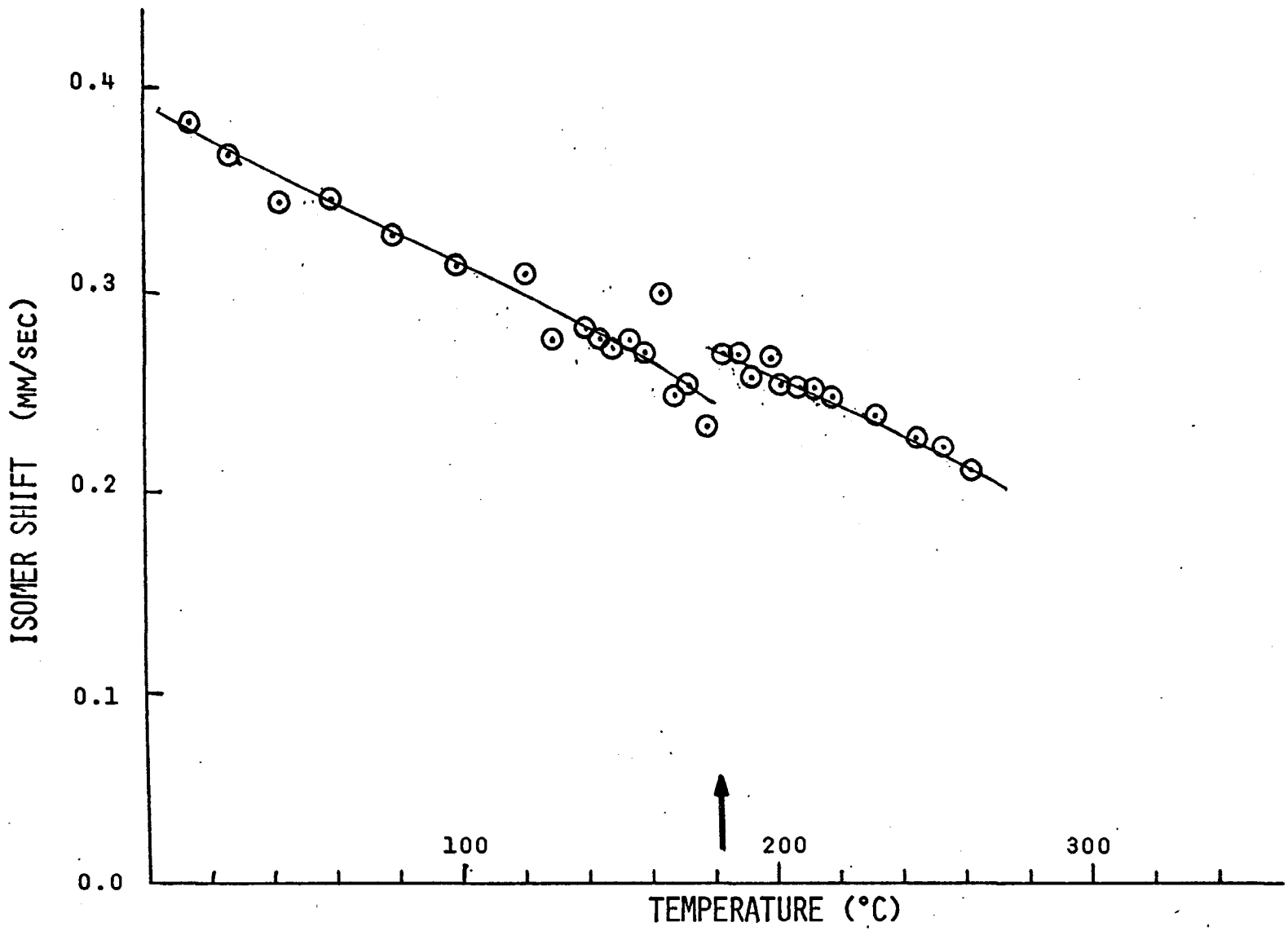

FIG. 33. Isomer shift as a function of temperature in Mossbauer studies of 95% $PbZrO_3$- 5% $BiFeO_3$.

related to the first order transition at 200°C. This was uncertain due to the scatter of the data points. The scatter was introduced by the poor resolution of the two peaks in the spectrum using the PARLORS program. The LORLSF program used above 200°C gave less scatter to the data. The slope above 200°C was about $2.15 \times 10^{-15}/°K$. This was in agreement with the Dulong-Petit limit of $2.41 \times 10^{-15}/°K$.

The "no impurity" data was not fitted to a four peak spectrum due to the obvious inequality (fig. 29) of the peaks. A model to fit this spectrum requires a knowledge of the angular dependence of f, so that the Karyagin effect can be estimated. A fit can probably be approximated using a fixed ratio of intensities for each pair and a fixed ratio of splitting between the two pairs. The pattern would have the makeup shown in fig. 34, which allows the observed asymmetry.

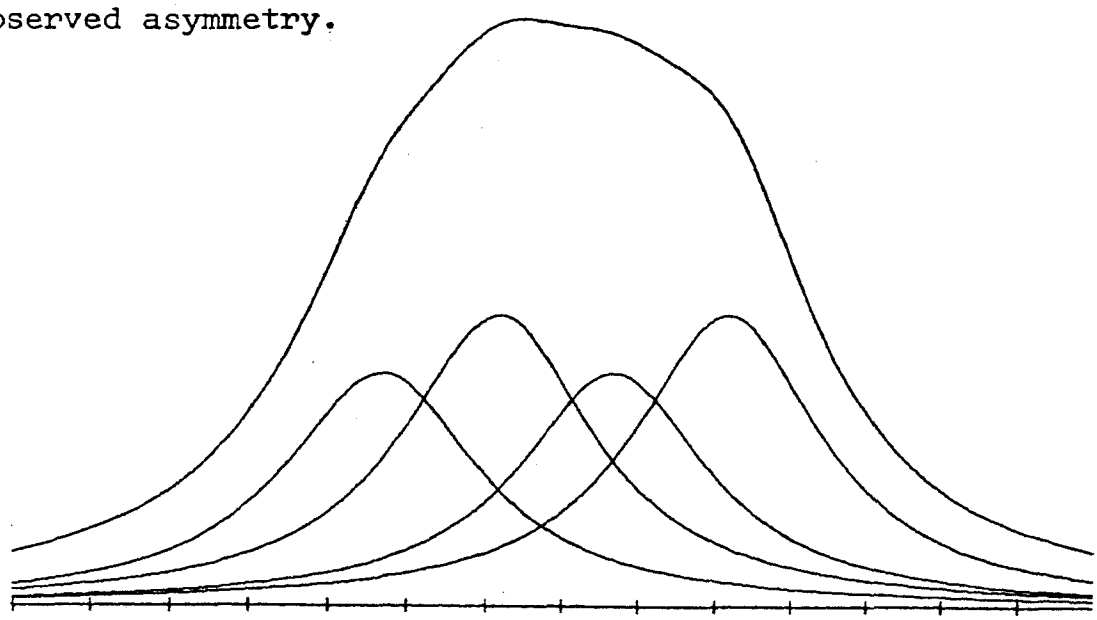

Fig.34. Model for asymmetric spectrum.

C. 95% (80% $PbZrO_3$-20% $PbTiO_3$)-5% $BiFeO_3$.

This sample was prepared by sintering 850°C for two hours and then air quenching. The same microtechniques of preparation and analysis were used as for the previous sample. The room temperature spectrum is shown in fig. 35. The splitting of the two peaks was more noticeable because of the reduced linewidth. The parameters of this spectrum are given in table VIII.

The f factor was 0.19 using measured linewidths (2.6 times the natural linewidth), and 0.64 assuming inhomogeneous broadening of the peak. The latter value was slightly less than that for the $PbZrO_3$ sample. The Debye temperature of this sample was about 300°K. The thickness was 0.00839 gm/cm^3 of sample. The iron used in preparation was 90.7% iron 57. This gave $n\sigma = 1.61$ for iron 57 in the sample. (See Appendix III).

The isomer shift was about equal to that of $PbZrO_3$ and corresponded to an ionicity of 56%. The electric field gradient was 2.6×10^{15} V/cm^3, larger than that of $PbZrO_3$, probably because of the larger ferroelectric polarization of this system. The higher distortion of the system, as indicated by the higher Curie point, should also result in a higher electric field gradient.

The peak area versus temperature is given in fig. 36. Three dips, which can be related to observed phase transitions in the material, can be seen at 100°C, 230°C

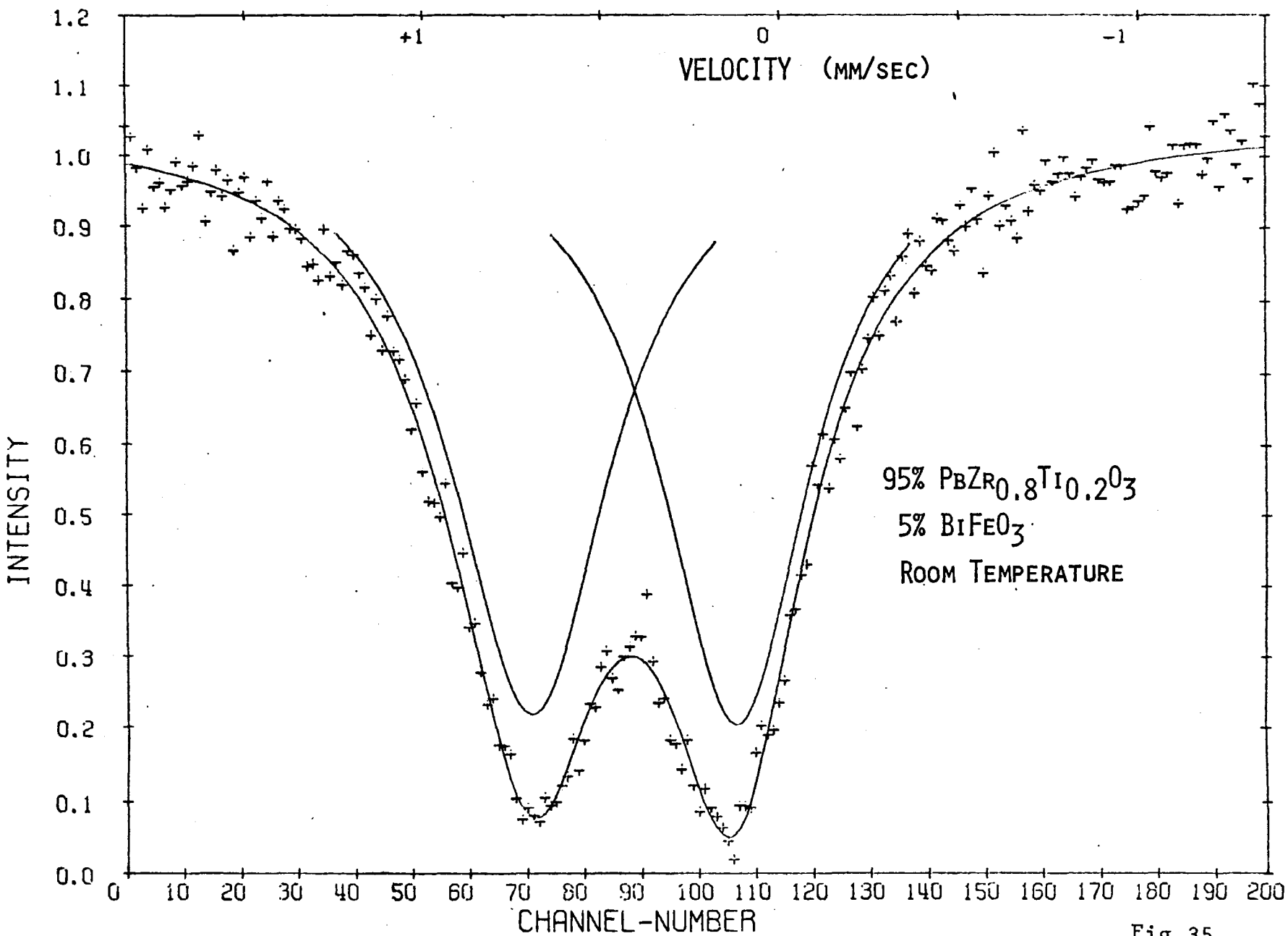
VELOCITY (MM/SEC)
+1
0
-1
INTENSITY
CHANNEL-NUMBER
95% PbZr0.8Ti0.2O3
5% BiFeO3
Room Temperature

Fig.35.

and 330°C. The lowest phase transition was observed by Cook[76] using electrical measurements. Neutron diffraction studies made at room temperature by Achenbach[66] showed that this system has a multiple-cell structure. Michel and Moreau[72] have since reduced the structure data and shown that they corresponded to the space group R3c. At higher temperature, there may be another phase, not confirmed yet, but thought to be an intermediate phase, still R3c, but in which the oxygen's occupy special positions rather than the general positions allowed by R3c. The third ferroelectric phase is known to belong to the space group R3m and to be single-cell. Finally the material becomes cubic, Pm3m. The dips in fig. 36 are quite broad and indicate the possible influence of high temperature electric conductivity on the relaxation time in the lattice. The dip at 230°C is not well determined by this data, so the intermediate phase is uncertain.

The electric quadrupole splitting (fig. 37) changes with temperature, but seems only slightly sensitive to the phase transitions at 120° and 270°C. The 330°C phase transition is not outstanding, possibly because the inhomogeneous broadening may mask out the splitting before it reaches this temperature. The PARLORS program was able to resolve the peaks well above the transition temperature. The large fluctuations in the data above 300°C may be due to changes in the number of oxygen defects during the phase

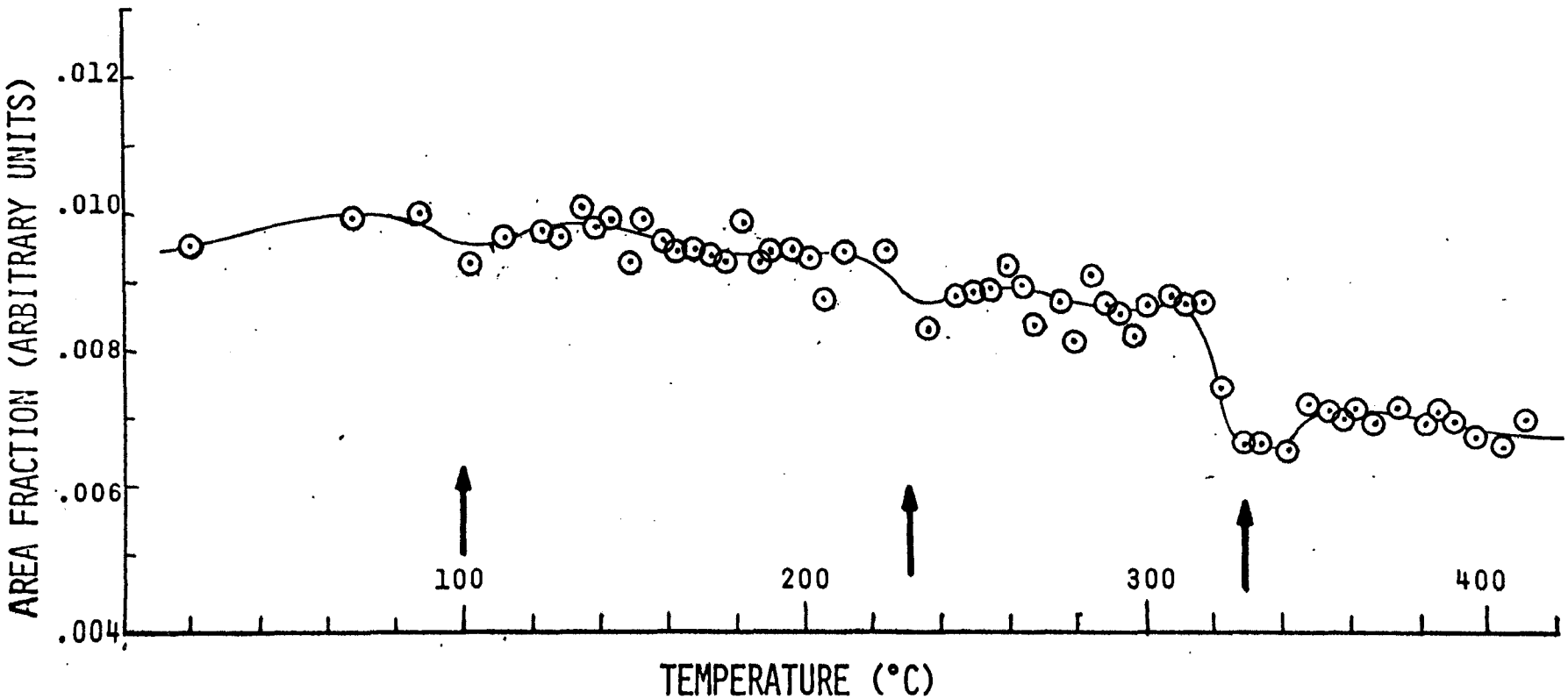

FIG. 36. Area fraction as a function of temperature in Mossbauer studies of 95% $(PbZr_{0.8}Ti_{0.2}O_3)$- 5% $BiFeO_3$.

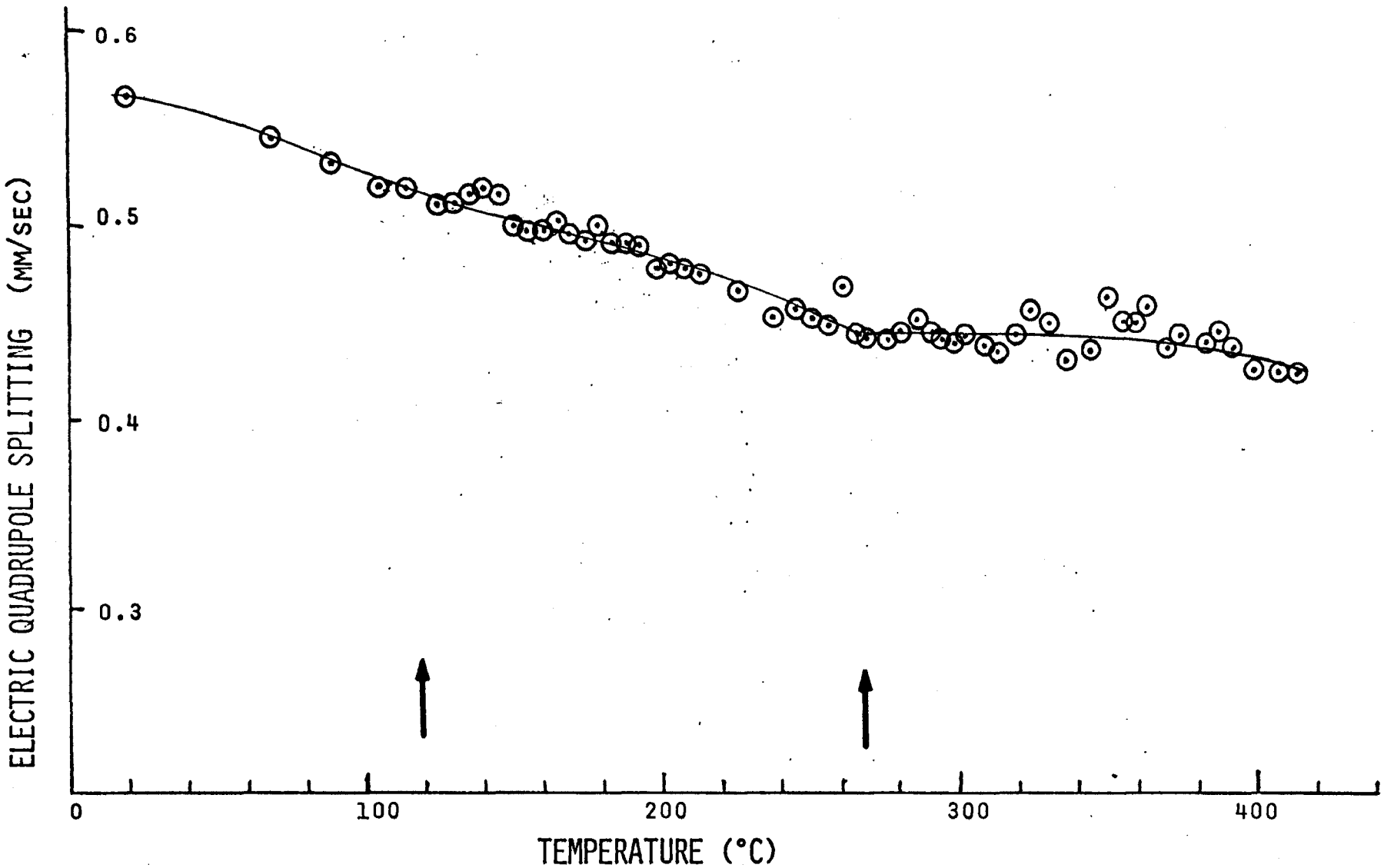

FIG. 37. Electric quadrupole splitting due to electric field gradient as a function of temperature in Mossbauer studies of 95% ($PbZr_{0.8}Ti_{0.2}O_3$)- 5% $BiFeO_3$.

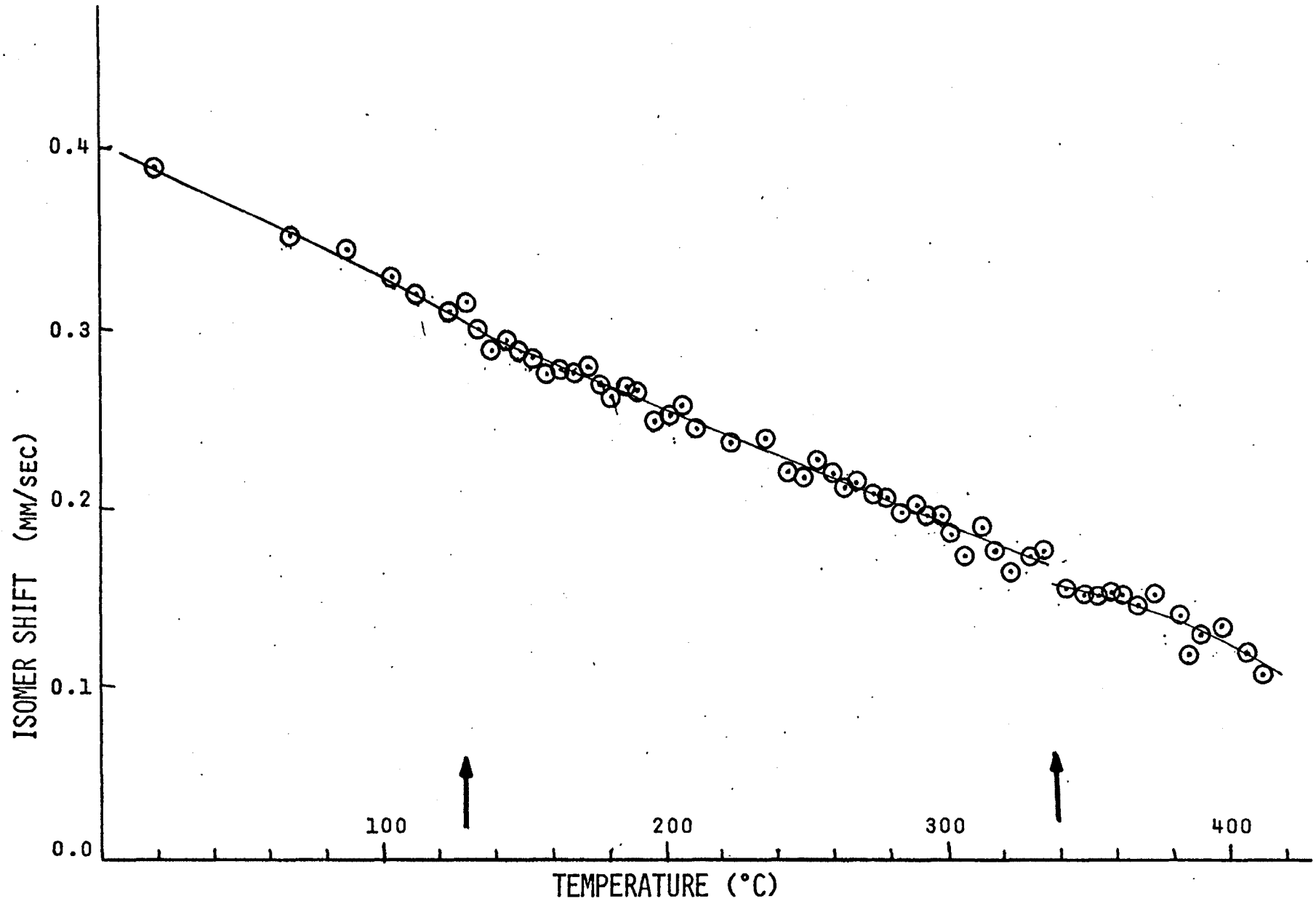

FIG. 38. Isomer shift as a function of temperature in Mossbauer studies of 95% ($PbZr_{0.8}Ti_{0.2}O_3$) - 5% $BiFeO_3$.

transition.

The isomer shift versus temperature curve (fig. 38) shows some slight irregularities in the slope near the phase transition points at 130° and 340°C. These are not well determined in terms of the error in the data, so exact temperatures cannot be obtained. The slope of this curve at high temperatures is about $2.2 \times 10^{-15}/°K$, as compared to the theoretical $2.41 \times 10^{-15}/°K$.

D. 95% (70% $PbZrO_3$- 30% $PbTiO_3$)-5% $BiFeO_3$.

This sample was sintered at 850°C for two hours and air quenched, using the microtechniques described earlier. The room temperature spectrum is given in fig. 39. It is very similar to the previous sample and was intended as a check on the results obtained on the 80/20 sample. The parameters of the spectrum are given in table VIII.

The thickness was 0.00456 gm/cm^3 of sample (see Appendix III). The iron in the sample was 90.7% iron 57, which gave $n\sigma = 0.877$. The area fraction, f, was 0.136, using measured linewidths (2.6 times the natural linewidth). If inhomogeneous broadening was assumed, then f = 0.42. This gave a Debye temperature of about 210°K, somewhat less than that for either the 80/20 or $PbZrO_3$ samples. The fact that the sample was half as thick may mean that the signal to noise ratio was higher than normal.

The isomer shift was just slightly less than that of the 80/20 sample and gave an ionicity of 54%. The electric

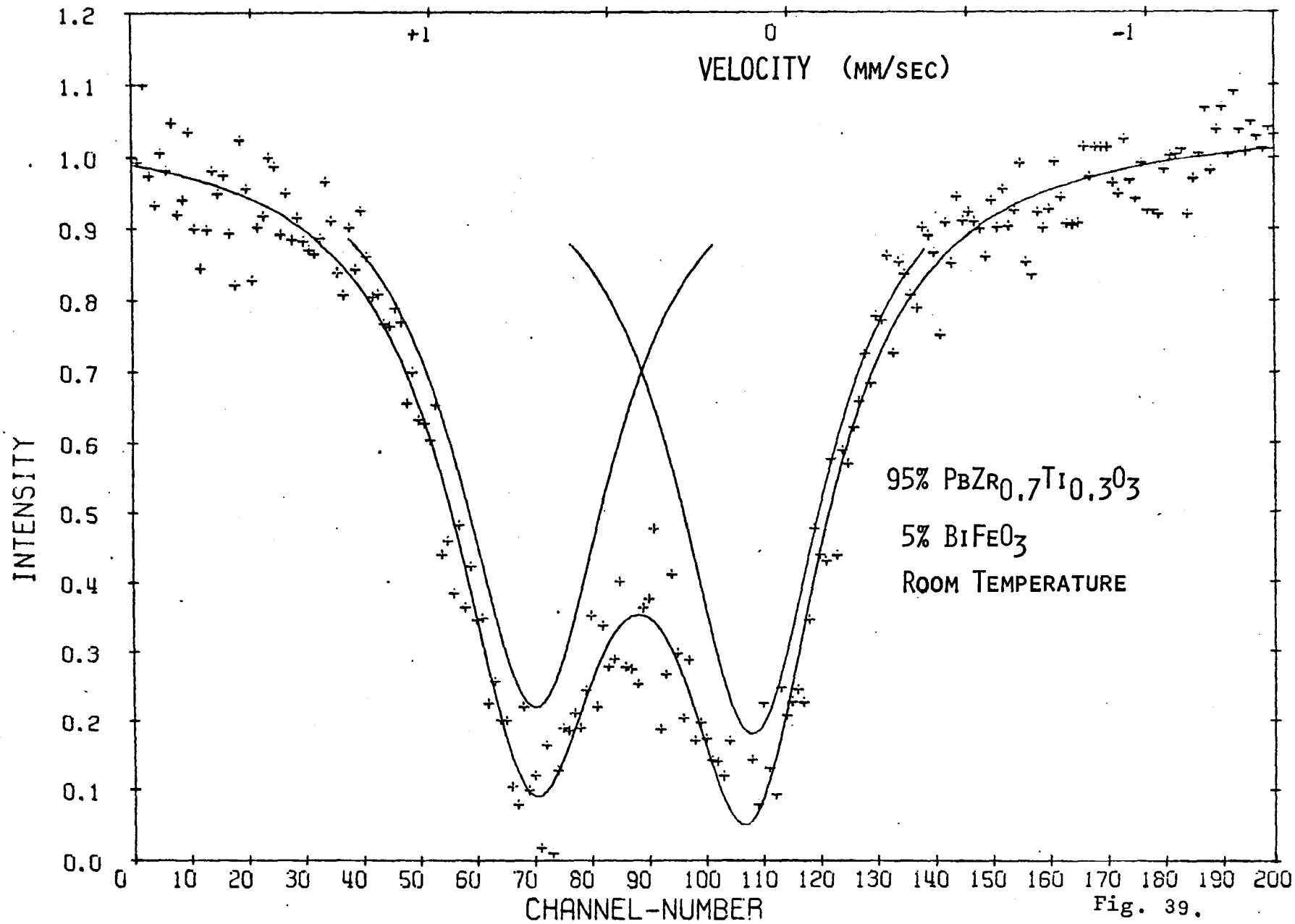
VELOCITY (MM/SEC)
+1
0
-1
INTENSITY
CHANNEL-NUMBER
95% PbZr0.7Ti0.3O3
5% BiFeO3
Room Temperature

Fig. 39.

field gradient was slightly larger, and was 2.72×10^{16} V/cm. This indicated the slightly higher distortion and higher Curie point of the 70/30 sample.

The peak area versus temperature curve in fig. 40 did not show any sharp transitions, but changes in the slope were present at 300°C and about 100°C. The same sequence of phase transitions was expected to occur here as in the 80/20 sample, though the lower two transitions should be lowered and the upper one increased in temperature. This was hard to determine from these data.

The electric quadrupole splitting as a function of temperature given in fig. 41, also showed slight breaks near these temperatures, again with a scatter problem above 300°C. A large splitting due to charge differences and oxygen defects remained above the expected ferroelectric transition at 330°C.

The isomer shift (fig. 42) showed a kink at 70°C, but was essentially a straight line until above 340°C where the slope appears to decrease. The slope was about 1.8×10^{-15}/°K above 340°C, but data were not obtained far enough above this point to insure that the slope was not affected by the specific heat of transition. The slope below 340°C was 2.51×10^{-15}/°K.

E. SUMMARY

The data show the presence of phase transitions, and suggest some of the mechanisms involved. They also show the effect of the thermodynamical parameters of phase

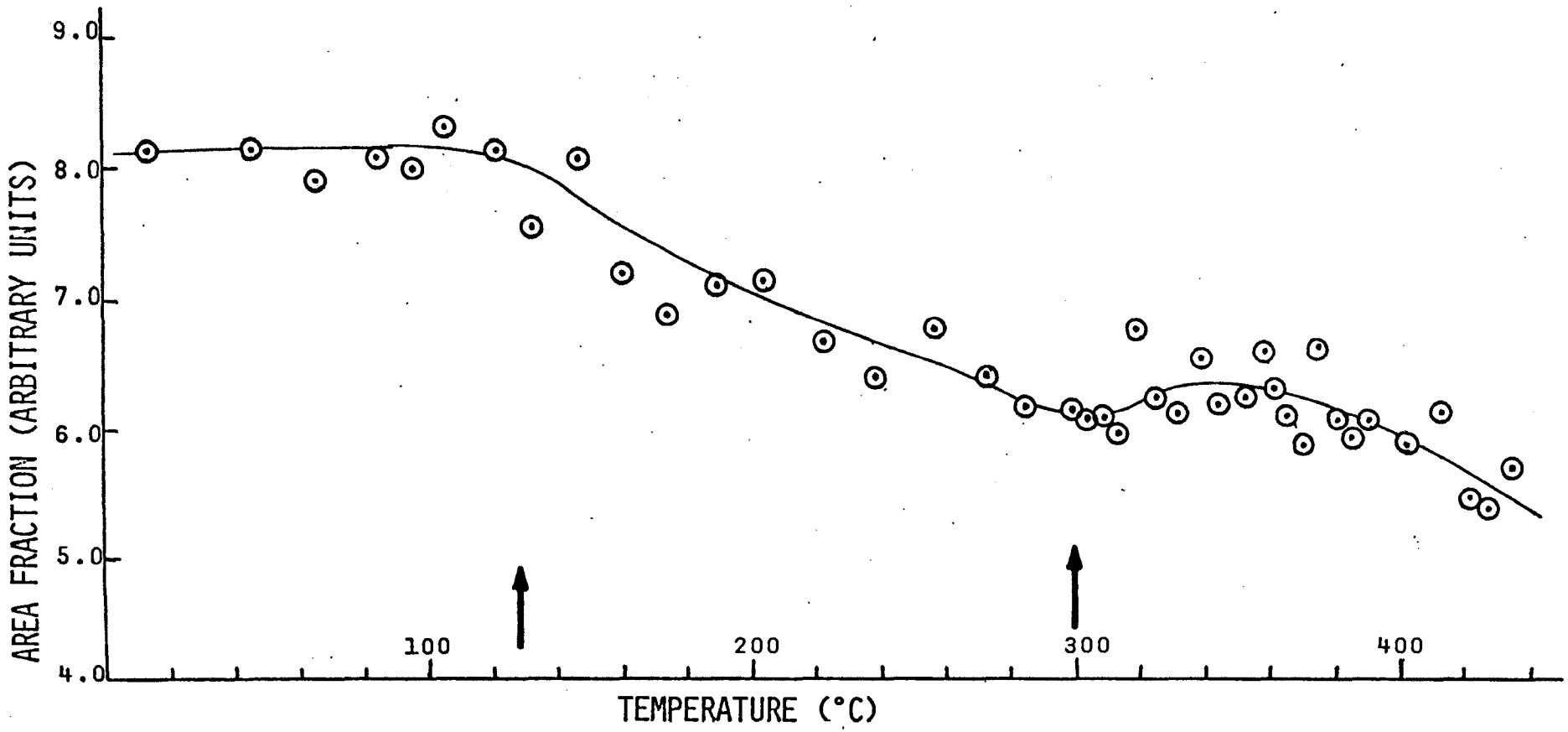

FIG. 40. Area fraction as a function of temperature in Mossbauer studies of 95% $(PbZr_{0.7}Ti_{0.3}O_3)$- 5% $BiFeO_3$.

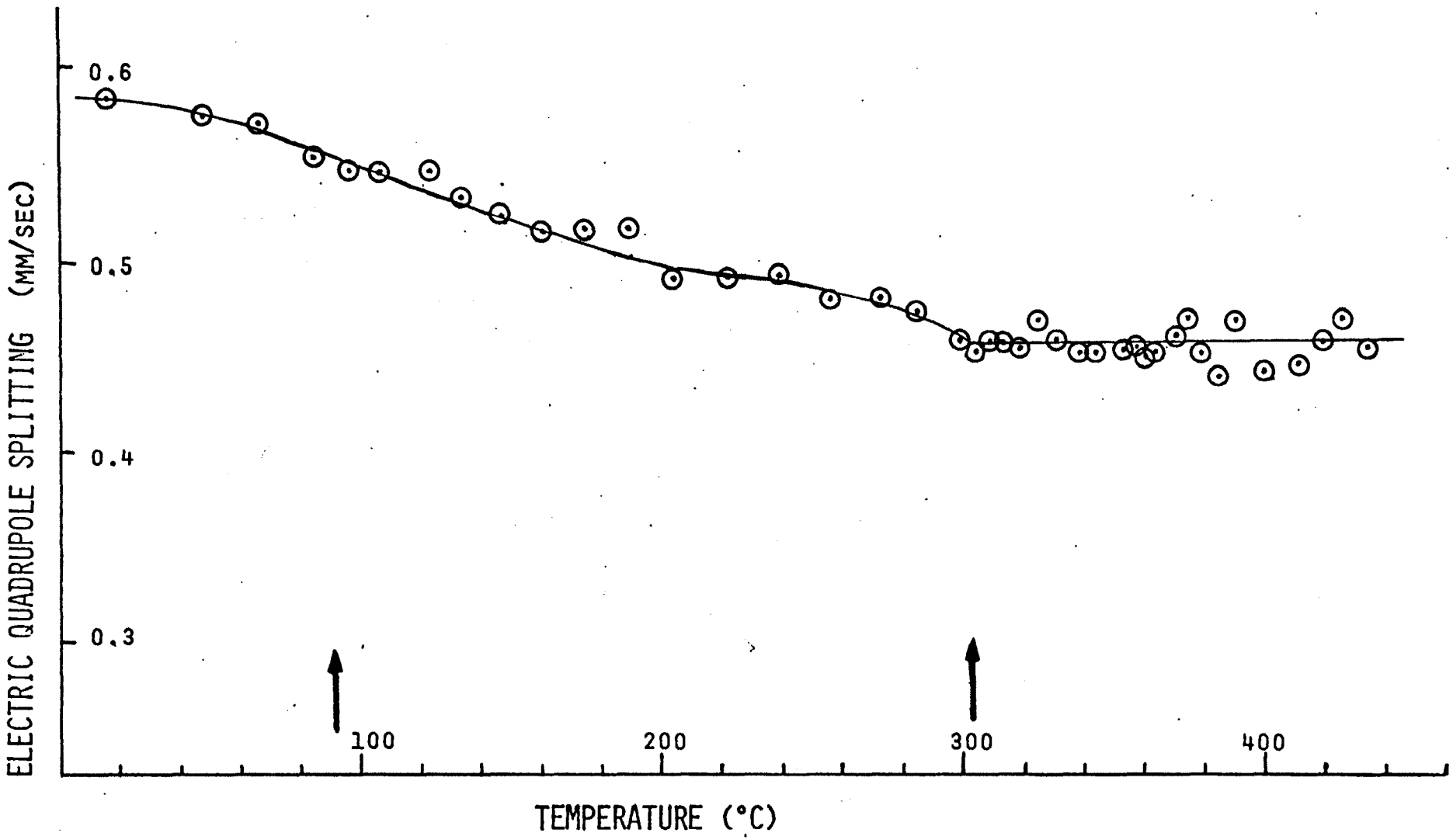

FIG. 41. Electric quadrupole splitting due to electric field gradient in Mossbauer studies of 95% ($PbZr_{0.7}Ti_{0.3}O_3$)- 5% $BiFeO_3$.

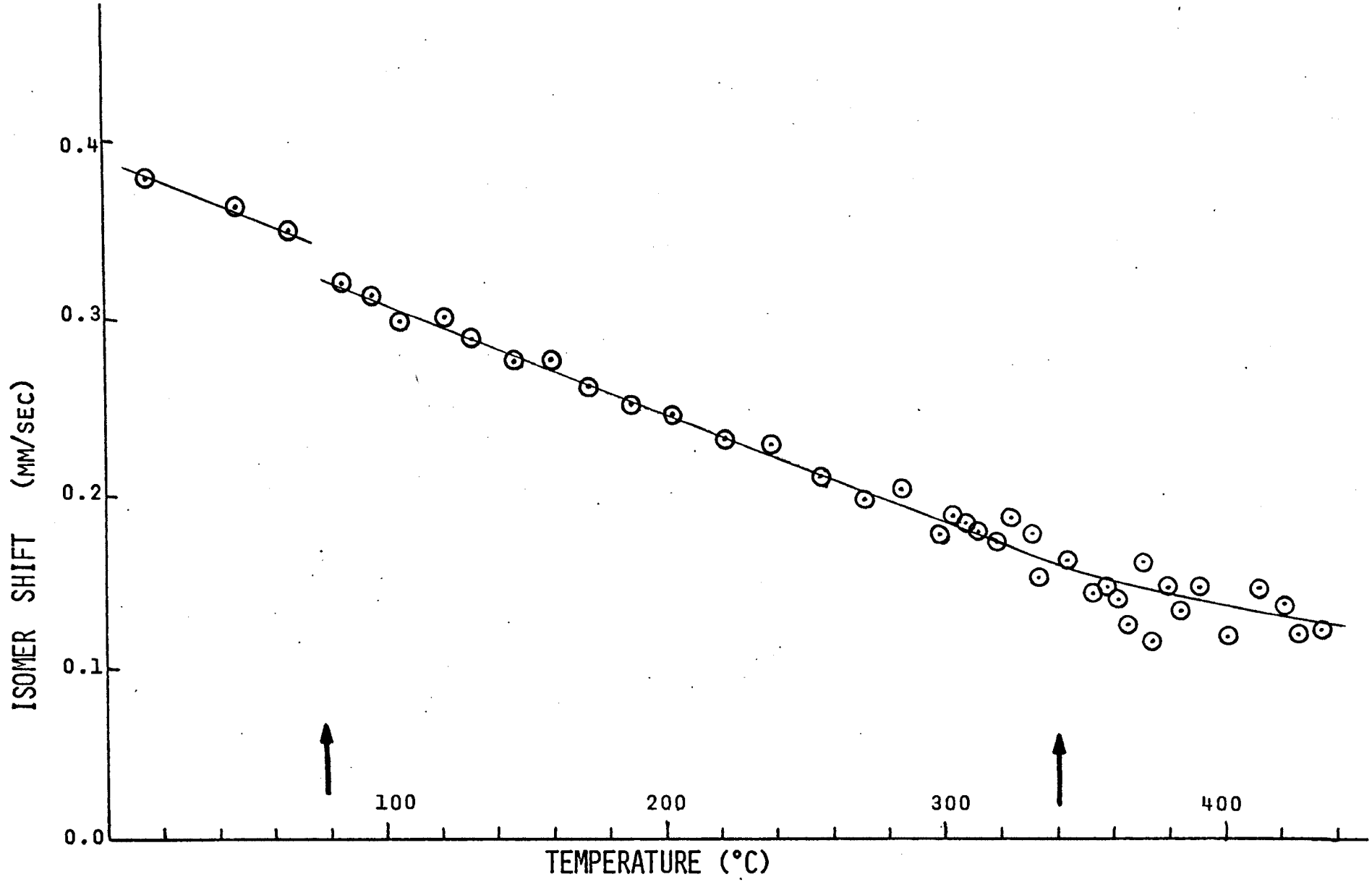

FIG. 42. Isomer shift as a function of temperature in Mossbauer studies of 95% ($PbZr_{0.7}Ti_{0.3}O_3$)- 5% $BiFeO_3$.

transitions. Table IX gives some of the special fraction observations for these three samples. The dip in area at the highest transition in all three samples was about 10% ± 3%. The areas of the dips varied widely due to nearby transitions and/or broad phase transitions. Since the dips were not well defined, no attempt was made to relate areas to lattice mode intensities.

TABLE IX.

SUMMARY OF DATA

SAMPLE		TRANSITION TEMPERATURES	IONICITY	ELECTRIC FIELD GRADIENT (V/cm^2)	DEBYE TEMPERATURE f	Θ_D ($\delta v/c$)	Θ_D (W)
95% $PbZrO_3$ 5% $BiFeO_3$	I.	200°C, 165-175°C	48%	2.12×10^{16}	.66	291°K	284°K
				(3:1) 1.08×10^{16}	.44	---	198°K
	II.		69%	2.10×10^{16}	.40	207°k	189°K
95%$PbZr_{.8}Ti_{.2}O_3$ 5%$BiFeO_3$		330°C, 230°C,100°C	56%	2.57×10^{16}	.64	304°K	273°K
95%$PbZr_{.7}Ti_{.3}O_3$ 5%$BiFeO_3$		310°C, 170°C, 70°C	54%	2.72×10^{16}	.42	188°K	194°K

V. DISCUSSION OF RESULTS

The samples measured show about the same qualitative behaviour near phase transitions, despite the differences in the structures and lattice mode spectra. The suggestion of Dvorak,[106] that antiferroelectric phase transitions should reduce the Mossbauer effect more drastically than ferroelectric phase transitions, was not confirmed by this experiment. Rather, the results indicated that phase transitions from cubic to antiferroelectric and to ferroelectric are quite similar. Recent measurements[81,83,84] on temperature dependent zone boundary lattice modes do not show that the mode depends on temperature over the whole zone as suggested by Silverman[57] and hence it appears that Dvorak's conclusion was incorrect.

In the ferroelectric phase transitions investigated here, the dielectric constant - temperature curves do not have very sharp peaks, thus indicating diffuse phase transitions. This has been observed also in both dielectric and Mossbauer area fraction data on the rhombohedral phase transition in $BaTiO_3$.[94]

The phase transition in lead zirconate may be split into two parts when impurities are added.[77] The sequence of phases is from cubic, Pm3m, to a ferroelectric phase (possibly rhombohedral R3m), and then to the antiferroelectric phase which is orthorhombic, multiple cell, and has space group Pba2. The intermediate phase is usually quite narrow

in temperature range, and determined mainly by means of hysteresis loops, rather than by x-ray diffraction.

The phase transition for the rhombohedral ferroelectrics 80/20 and 70/30 is probably in the following sequence:

I. Room Temperature to 100°C. This structure is rhombohedral double-cell, R3c. The oxygen, besides being displaced along a face diagonal, are displaced slightly off the diagonal. The A and B ions are displaced along [111] to give the ferroelectric dipole moment.

II. 100°C to 200°C. This structure results from the oxygen returning to the face diagonal. The oxygen are now centrosymmetric, but the A and B ions are still noncentrosymmetric. The structure is double-cell rhombohedral, R3c.

III. 200°C to 300°C. The oxygen displace to reduce the structure to single-cell rhombohedral R3m. This places the oxygen in noncentrosymmetric positions displaced perpendicular to the face of the perovskite cell. By this time the A and B ions have become less shifted along [111], so the polarization is reduced.

IV. Above 300°C. The ideal cubic perovskite structure, Pm3m is found, and the material is paraelectric.

The temperatures are only typical for the $PbZrO_3$-$PbTiO_3$ system. The phase transitions may be of second order because of the small changes of symmetry in the

crystal, but classification is difficult.

The area versus temperature measurements suggest that there are intermediate transitions I-II and II-III which may be due to zone edge lattice modes, since dielectric measurements do not show these transitions. The group-theoretical analysis of Cochran and Zia arrives at the same conclusion.

Lead zirconate shows a dielectric anomaly due to a k = 0 lattice mode, with a Curie point of 150°C, but the transition takes place at about 200°C, because of a mode at the zone boundary, which also becomes unstable. The suggestion of an intermediate ferroelectric phase is based on the rise in the dissipation factor and the broad irregular dip in area fraction obtained near the transition temperature. This may be a two phase region or simply an electrically imposed transition which occurs quite readily in the broad, soft region indicated by our measurements.

The f values determined from this data indicate that $PbZrO_3$ is the most rigid lattice, as do the isomer shift predictions of ionicity, which make it more covalent than the ferroelectric compounds. This indicates that the strongly distorted structure has more bonding overlap or covalency. The two ferroelectric compounds show quite different f values and Debye temperatures, while the ionicity is about the same. This may be due entirely to the change in transition temperature of the I-II phase

which indicates a softer lattice, and hence a lower f, for the 70/30 sample.

The electric field gradients of the different samples are in accordance of their expected polarizations. The decrease of the electric field gradient with increasing temperature seems to be directly connected to the polarization of the lattice, except for the splitting caused by the charge differences at the B sites and possible oxygen defects. The values of the electric field gradient are about those obtained for $BiFeO_3$,[126] but about twice as large as that for $BaTiO_3$.[91]

The electric field gradient for $PbZrO_3$ is complicated by the existence of two zirconium sites in the lattice which have different electric field gradients. These gradients seem to be due to the polarization along the z-axis and hence not related to the antiferroelectric structure in the xy plane. There is a possibility of a small contribution from the apparent phase transition near 170°C due to antiferroelectricity. Recent attempts have finally succeeded in fitting the spectrum to four peaks. Problems still exist in fitting the asymmetry in the peaks, so no estimates of the Karyagin effect are available. For the other samples the peaks are very symmetric.

The inhomogeneous broadening in this experiment is due to the charge inequality of the A ions (Pb^{2+}, Bi^{3+}) and the B ions (Zr^{4+}, Ti^{4+}, Fe^{3+}). The random array of these ions

in forming the compositional solid solution introduce at least four different local electric field gradients on the Fe^{3+} ion, as given by Bell.[101]

The calculation of the electric field gradients thus becomes very difficult, since exact bonding strengths, atomic positions, and knowledge of oxygen defects are needed to reproduce the effect of the broadening. A good measurement of the structural electric field gradient is not possible, because the two effects interact to give only an average effect which may be larger or smaller than the actual effect, depending upon the probability of the different states. If we assume the same effect for all the samples, then intercomparison can be made.

It appears, since the splitting of the peaks above the expected transition temperature increases with addition of $PbTiO_3$, that part of the effect is due to the size difference of the Zr^{4+} and Ti^{4+} ions. Thus the splitting is due to a combination of the charge differences of Fe^{3+} and Zr^{4+} (and Bi^{3+} and Pb^{2+}) and the size differences of Zr and Ti. The contribution of each may be roughly equal. Data run with 95% $PbTiO_3$-5% $BiFeO_3$ showed a much reduced splitting above the transition temperature, so that Ti is probably a more compatible ion than Zr with Fe in the lattice. This is in accordance with the ionic sizes given previously.

The computer programs used in analyzing the data

could perhaps be improved, and this might result in reduced scatter of data points. There are now available non-linear regression programs, which give rapid convergence and valid minimum tests for the least squares fit of the data. The PARLORS program could only test the error between interations, while the LORLSF program is slowly convergent with no test on the least square errors. It appears very unlikely, however, that a change of programs would result in appreciably different conclusions.

VI. SUMMARY OF RESULTS

The significant new results obtained in this experiment were as follows:

1. The similarity of antiferroelectric and ferroelectric transitions in perovskites with respect to the Mossbauer effect data has been established.
2. The lattice mode behavior with temperature appear to be similar for antiferroelectrics and ferroelectrics.
3. The polarization of the antiferroelectric lattice is evident in the electric quadrupole splitting data. This is mostly due to displacements along the c-axis of the zirconium ion.
4. The linewidths for the antiferroelectric were much wider than for the ferroelectric. This is explained by the two non-equivalent sites for zirconium in $PbZrO_3$, which give two different electric field gradients. A fit has been obtained using four peaks which give linewidths nearly as narrow as for the other samples. There is still a problem in fitting the asymmetry of the peaks in $PbZrO_3$. Single crystal measurements as a function of incident angle and applied field are required to separate the anharmonic contributions to the f- factor from the electric field gradient.

Bibliography

(1) Mossbauer, R. L., Z. Physik, 151, 124 (1958).

(2) Mossbauer, R. L., Naturwissenschaften, 45, 538 (1958) (English translation).

(3) Lamb, W. E., Phys. Rev., 55, 190 (1939).

(4) Metzger, F. R., Progress in Nuclear Physics, 7, 53 (1959).

(5) Lipkin, H. J., Ann. Phys., 9, 332 (1960).

(6) Ziman, J. M., Principles of the Theory of Solids, (Cambridge Press, Cambridge, 1964) P.60

(7) Handbook of Mathematical Functions, ed. by M. Abramowitz, and I. Stegun, (Dover Publ., New York, 1965) p. 998.

(8) Abragam, A., L'effet Mossbauer et ses Applications a l'etude des Champs internes, (Gordon and Breach, (New York, 1964).

(9) Boyle, A. J. F., and H. E. Hall, "The Mossbauer Effect", Repts. Prog. Phys., 25, 441 (1962).

(10) Danon, J., Lectures on the Mossbauer Effect, (Gordon and Breach, New York, 1968).

(11) Pound, R. V., and G. A. Rebka, Jr., Phys. Rev. Letters, 4, 337 (1960).

(12) Hamill, D. W., and G. R. Hoy, Phys. Rev. Letters, 21, 724 (1968).

(13) Gonser, U., "Applications of the Mossbauer Effect in Materials Science", Materials Science and Engineering, 3, 1 (1968/1969).

(14) Sawyer, C. B. and C. H. Tower, Phys. Rev., 35, 269 (1930).

(15) Kittel, C., Introduction to Solid State Physics, (J. C. Wiley, New York, 1966) Third Edition, p. 382.

(16) Devonshire, A. F., Phil. Mag., 40,1040 (1949).

(17) Devonshire, A. F., Phil. Mag., 42, 1065 (1951).

(18) Devonshire, A. F., Adv. In Phys., 3, 85 (1954).

(19) Cochran, W., Adv. in Phys., 9, 387 (1960).

(20) Anderson, P. W., in Fizika Dielektrikov, edited by G. I. Skanavi (Akademiia Nauk SSSR, Moscow, 1960).

(21) Lyddane, R. H., R. G. Sachs, and E. Teller, Phys. Rev., 59, 673 (1960).

(22) Barker, A. S., Notes from Delft Summer School (1968) to be published.

(23) Ginzburg, V. L., Zhur. Eksp. i Teor. Fiz., 19, 36 (1949); and Usp. Fiz. Nauk, 38, 490 (1949).

(24) Ginzburg, V. L., Soviet Phys.-Solid State, 2, 1824, (1960).

(25) Landau, L. D., and L.M. Liftshitz, Statistical Physics, (Addison-Wesley, Reading Mass., 1958), ch. 14.

(26) Vaks, V. G., V. M. Galitskii, and A. I. Larkin, Soviet Physics-JETP, 24, 1071 (1967).

(27) Vaks, V. G., Soviet Phys.-JETP, 27, 486 (1968).

(28) Kwok, P. C., and P. B. Miller, Phys. Rev., 151, 387 (1966).

(29) Cowley, R. A., Adv. in Phys., 12, 421 (1964).

(30) Cowley, R. A., Phil. Mag., 11, 673 (1965).

(31) Silverman, B. D., Phys. Rev., 135, A1596 (1964).

(32) Doniach, S., Proc. of the International Conf. on Lattice Dynamics, ed. by R. F. Wallis, (Pergamon Press, London, 1965).

(33) Lines, M. E., Phys. Rev., 177, 797 (1969).

(34) Lines, M. E., Phys. Rev., 177, 812 (1969).

(35) Lines, M. E., Phys. Rev., 177, 819 (1969).

(36) Brout, R., K.A. Muller and H. Thomas, Solid State Comm 4, 507 (1966).

(37) Jahn, H. A., and E. Teller, Proc. Royal Soc., A161, 220 (1937).

(38) Fridkin, V. M., JETP Letters, 3, 161 (1966).

(39) Sinha, K. P., and A.P. B. Sinha, Indian J. Pure and Appl. Phys., 2, 91 (1964).

(40) Shukla, G. C. and K. P. Sinha, J. Phys. Chem. Solids, 27, 1837 (1966).

(41) Bersucker, I. B., Physics Letters (Neth.), 20, 589 (1966).

(42) Jones, H. C., "A Study of Bismuth Ferrate and Bismuth Manganate in solid solution with Lead Titanate", Thesis for Masters of Science in Physics, University of Missouri-Rolla, 1968.

(43) Birman, J. L., in Proc. of Symposium on Ferroelectricity, ed. by E. F. Weller, (Elsevier, Amsterdam, 1967), p.55.

(44) Anderson, P. W., and E. I. Blount, Phys. Rev. Letters, 14, 217 (1965).

(45) Yamada, Y., G. Shirane and A. Linz, Phys. Rev., 177, 848 (1969).

(46) Haas, C., Phys. Rev., 140, A863 (1965).

(47) Goldrich, F. E., and J. L. Birman, Phys. Rev., 167, 528 (1968).

(48) Cochran, W., and A. Zia, Phys. Stat. Sol., 25, 273, (1968).

(49) Cowley, R. A., Phys. Rev., 134, A981 (1964).

(50) Barker, A. S., and J. J. Hopfield, Phys., 135, A1732, (1964).

(51) Barker, A. S., Phys. Rev., 145, 391 (1966).

(52) Barker, A. S., and R. Loudon, Phys. Rev., 158, 433, (1967).

(53) Murzin, V. N., R. E. Pasynkov, and S. P. Solov'ev, Soviet Phys.-USPEKHI, 10, 453 (1968).

(54) Kittel, C., Phys. Rev., 82, 729 (1951).

(55) Cross, L. E., Phil. Mag. (Serial 8), 1, 76 (1956).

(56) Slater, J. C., Phys. Rev., 78, 748 (1950).

(57) Silverman, B. D., Phys. Rev., 128 638 (1962).

(58) Miller, P. B. and P. C. Kwok, Solid State Comm., 5, 57 (1967).

(59) Goldschmidt, V. M., Skrift Norske Vidensk. Akad., nos. 2 and 8, (1926).

(60) Kanzig, W., Ferroelectrics and Antiferroelectrics, in Solid State Physics, vol. 4, pp. 1-197, (Academic Press, New York, 1957).

(61) Jona, F., and G. Shirane, Ferroelectric Crystals, (Pergamon Press, New York, 1962).

(62) Megaw, H. G., Ferroelectricity in Crystals, (Methuen, London, 1957).

(63) Chou, Pen-chu, "An X-ray Study of the Lead Zirconate-Bismuth Ferrate System", Thesis for Masters of Science in Chemistry, University of Missouri at Rolla (1965).

(64) Gerson, R., P. Chou, and W. J. James, J. Appl. Phys., 38, 55 (1967).

(65) Clarida, D. R., "A Crystallographic Study of the $PbZrO_3$-$PbTiO_3$-$BiFeO_3$. Ternary System.", Thesis for Masters of Science in Chemical Engineering, University of Missouri-Rolla (1966).

(66) Achenbach, G. D., "A Structural Investigation of Bismuth Ferrate and the $BiFeO_3$-$PbTiO_3$ Ternary System.", Thesis for Ph. D. in Chemical Engineering, University of Missouri-Rolla, (1967).

(67) Smith, R. T., "High Frequency Ferroelectric Properties of the $BiFeO_3$-$PbTiO_3$-$PbZrO_3$ Ternary System.", Thesis for Ph.D. in Physics, University of Missouri-Rolla. (1967).

(68) Smith, R. T., G. D. Achenbach, R. Gerson, and W. J. James, J. Appl. Phys., 39, 70 (1968).

(69) Latham, J. I., "Magnetic Properties of the $BiFeO_3$-$PbTiO_3$-$PbZrO_3$ Ternary System.", Thesis for Ph.D. in Physics, University of Missouri-Rolla, (1967).

(70) Michel, C., "Ferroelectric Properties of Bismuth Ferrate and Related Materials.", Progress Report COO-1368-9, University of Missouri-Rolla (1969).

(71) Michel, C., J. M. Moreau, G. D. Achenbach, R. Gerson, and W. J. James, "The Atomic Structure of $BiFeO_3$." Accepted for publication in Solid State Comm.

(72) Michel, C., J. M. Moreau, G. D. Achenbach, R. Gerson, and W. J. James, "Atomic Structure of Two Rhombohedral Ferroelectric Phases in the $Pb(Zr,Ti)O_3$ Solid Solution System.", Accepted for Publication in Solid State Comm.

(73) Megaw, H. D., Acta Cryst., A24, 583 (1968).

(74) Abrahams, S. C., H. J. Levinstein, and J. M. Reddy, J. Phys. Chem. Solids, 27, 1019 (1966).

(75) Abrahams, S. C., S.K. Kurtz, and P. B. Jamieson, Phys. Rev., 172, 551 (1968).

(76) Jona, F. G. Shirane, F. Mazzi, and R. Pepinsky, Phys. Rev., 105, 349 (1957).

(77) Shirane, G. and S. Hoshino, Acta Cryst. 7, 203, (1954).

(78) Cook. W. R., Jr., "Research for Switching in Ferroelectric Crystals", Tech, Rept, AFAL-TR-66-209, Clevite Corp,110 P., (1966).

(79) Benguigui, L., Can. J. Phys., 46, 1627 (1968).

(80) Unoki, H., and T. Sakudo, J. Phys. Soc. Japan, 23, 546 (1967).

(81) Shirane, G., and Y. Yamada, Phys. Rev., 177, 858 (1969).

(82) Yamada, Y., and G. Shirane, J. Phys. Soc. Japan, 26, 396 (1969).

(83) Cowley, R. A., W. J. L. Buyers, and G. Dolling, Solid State Comm., 7, 181, (1969).

(84) Axe, J. D., G. Shirane, and K. A. Mueller, Bull, Am. Phys. Soc., 14, 60 (1969).

(85) Plakhty, V., and W. Cochran, Phys. Stat. Sol., 29, K81 (1968).

(86) Thomas, H., and K. A. Mueller, Phys. Rev. Letters, 21, 1256 (1968).

(87) Muzikar, C., V. Janovec, and V. Dvorak, Phys. Stat. Sol., 3, K9 (1963), also given in Proc. of the Dubna Conference on the Mossbauer Effect (1961), (Consultants Bureau, New York, 1963), p [illegible]-1.

(88) Schmidt, H., Phys. Rev., 156, 552 (1967).

(89) Pham Zuy Hien, A.S. Viskov, V.S. Shpinel', and Yu.N. Venevtsev, Soviet Phys.-JETP, 17, 1465 (1963).

(90) Mitrofanov, K.P., A.S. Viskov, G.Ya. Driker, M.V. Plotnikova, Pham Zuy Hien, Yu.N. Venevtsev, and V. S. Shpinel, Soviet Phys.-JETP, 19, 260 (1964).

(91) Bhide, V. G. and M.S. Multani, Phys. Rev., 139, A1983 (1965).

(92) Chekin, V.V., V.P. Romanov, B.I. Verkin, and V.A. Bokov, JETP Letters, 2, 117 (1965).

(93) Bokov, V.A., V.P. Romanov, and V.V. Chekin, Soviet Phys.-Solid State, 7, 1521 (1965).

(94) Belov, V.F., and I.Z. Zheludev, JETP Letters, 6, 287 (1967).

(95) Plotnikova, M.V., A.S. Viskov, K.P. Mitrofanov, V.S. Shpinel', and Yu.N. Venevtsev, Izv. AN SSSR, ser. fiz., (Bull. Acad. Science USSR, Physics Series) 31, 1129 (1967).

(96) Sklyarevskii, V.V., I.I. Lukashevich, V.P. Romanov, N.I. Filippov, Yu.N. Venevtsev, and A.S. Viskov, JETP Letters, 3, 135 (1966).

(97) Bhide, V. G., and M.S. Multani, Phys. Rev., 149, 289 (1966).

(98) Matthias, B.T., Science, 113, 591 (1951).

(99) Bhide, V.G., and H.C. Bhasin, Phys. Rev., 159, 586 (1967).

(100) Bhide, V.G. and H.C. Bhasin, Phys. Rev., 172, 290 (1968).

(101) Bell, R.O., J. Phys. Chem. Solids, 29, 1 (1968).

(102) Stoneham, A.M., Rev. Mod. Phys., 41, 82 (1969).

(103) Gallagher, P.K., J.B. MacChesney, and D.N.E. Buchanan, J. Chem. Phys., 41, 2429 (1964).

(104) Shimony, U., and J. M. Knudsen, Phys. Rev., 144, 361 (1966).

(105) Gallagher, P.K. and J. B. MacChesney, in Symposia of the Faraday Society, No. 1, p. 40, (1967).

(106) Dvorak, V., Phys. Stat. Sol., 14, K161 (1966).

(107) Multani, M. and K. A. Mueller, Helv. Phys. Acta, 41, 407, (1968).

(108) Dlouha, J., Czech. J. Phys., B14, 570 (1964) and B14, 580 (1964).

(109) Vaks, V.G., V.M. Galitskii, and A.I. Larkin, Soviet Phys. JETP, 27, 627 (1968).

(110) Spijkerman, J.J., F.C. Ruegg, and L. May, in Mossbauer Effect Methodology, Vol. 2, p. 85, (Plenum Press, New York, 1966).

(111) Walker, L. R., G. K. Wertheim, and V. Jaccarino, Phys. Rev. Letters, 6, 98 (1961).

(112) Danon, J., in Applications of the Mossbauer Effect in Chemistry and Solid State Physics, Tech. Rept. 50, (Intn'l Atomic Energy Agency, Vienna, 1966) p.89.

(113) Bhide, V. G., G.K. Shenoy, and M.S. Multani, Solid State Comm., 2, 221 (1964).

(114) Blokhin, M.A., and A. T. Shuvaev, Izv, AN SSSR, ser. fiz., (Bulletin Acad. Sci. USSR, Physics) 22, 1447 (1958).

(115) Shuvaev, A. T., Izv. AN SSSR, ser. fiz. (Bull. Acad. Sci. USSR, Physics), 23, 551 (1959).

(116) Erickson, N.E., "Mossbauer Spectroscopy of Iron Compounds", in The Mossbauer Effect and its Application to Chemistry, (American Chemical Society, (Washington D. C., 1967) pp 86-104.

(117) Sternheimer, R.M., Phys. Rev., 80, 102 (1950); 84, 244 (1951), 86, 316 (1952); 95, 736 (1954); 105, 158 (1957).

(118) Chappert, J., R.B. Frankel, A. Misetich, and N.A. Blum, Phys. Letters (Neth.), 28B, 406 (1969).

(119) Bersohn, R., J. Chem. Phys., 29, 326 (1958).

(120) Zhdanov, G.S., S.P. Solov'ev and Yu.N. Venevtsev, Soviet Phys. Cryst., 2, 630 (1959).

(121) Solov'ev. S.P., Yu.N. Venevtsev, and G.S. Zhdanov, Soviet Phys. Cryst., 5, 686 (1961).

(122) Lyubimov, V.N., Yu.N. Venevtsev, and G.S. Zhdanov, Soviet Phys. Cryst., 7, 178 (1962).

(123) Lyubimov, V.N., Yu.N. Venevtsev, Soviet Phys.-Solid State, 4, 993 (1962).

(124) Lyubimov, V.N., Yu.N. Venevtsev, and G.S. Zhdanov, Soviet Phys.-Solid State, 4, 1554 (1963),

(125) Lyubimov, V.N., Yu.N. Venevtsev, S.P. Solov'ev, G.S. Zhadanov, and A.B. Bakushinskii, Soviet Phys.-Solid State, 4, 2594 (1963).

(126) Tomashpol'skii, Yu.Ya., and Yu.N. Venevtsev, Soviet Phys.-Cryst., 12, 18 (1967).

(127) Preston, R.S., S.S. Hanna, and J. Heberle, Phys. Rev., 128, 2207 (1962).

(128) Havens, W.W., and L. J. Rainwater, Phys. Rev., 83, 1123 (1951).

(129) Shirley, D.A., M. Kaplan, and P. Axel, Phys. Rev., 123, 816 (1961).

(130) Lang, G., Nuclear Instrum. and Methods, 24, 425 (1963).

(131) Margulies, S., and J.R. Ehrman, Nuclear Instrum. and Methods, 12, 131 (1961).

(132) Bykov, G.A., and Pham Zuy Hien, in Proc. of the Dubna Conf. of the Mossbauer Effect, (Consultants Bureau, New York, 1963) p.2-1.

(133) Housley, R.M., N.E. Erikson, and J.G. Dash, Nuclear Instrum. and Methods, 27, 29 (1964).

(134) Fritsburg, V.Ya., Soviet Phys.-Solid State, 10, 304 (1968).

(135) Shur, M.S., Soviet Phys.-Solid State, 10, 2087 (1969).

(136) Karyagin, S.V., Dokl.Akad. Nauk, SSSR, 148, 1102-5, (1963), also Soviet Phys.-Solid State, 5, 1552, (1964).

(137) Goldanskii, V.I., S.V. Karyagin, E.F. Makarov, and V.V. Khrapov, in The Proc. of the Dubna Conf. of the Mossbauer Effect, (Consultants Bureau, New York, 1963), p. 24-1.

(138) Taylor, R.D., and P.P. Craig, Phys. Rev., 175, 782 (1968).

(139) Banks, B., "The Mossbauer Effect in Bismuth Ferrate.", Thesis for Masters of Science in Physics, University of Missouri-Rolla, (1966).

(140) May, L. and D.K. Snediker, Nuclear Instrum. and Methods, 55 183 (1967).

(141) Kistner, O.C., and J.B. Swan, in The Mossbauer Effect, Ed. by Compton and Schoen, (J.C. Wiley, New York, 1962) p. 270.

(142) Wertheim, G. K., Mossbauer Effect, (Academic Press, New York, 1964), p.22.

(143) Kankeleit, E., in Mossbauer Effect Methodology, vol. 1, (Plenum Press, New York, 1965) p. 47.

(144) Cohen, R.L., P. G. McMullen, and G. K. Werthein, Rev. Sci, Inst., 34, 671 (1963).

(145) Cohen, R. L., Rev. Sci. Inst., 37, 957 (1966).

(146) Spijkerman, J. J., NBS Tech Note # 276, 101 (1965).

(147) Rhodes, E., W. O'Neal and J.J. Spijkerman, NBS Tech Note #404, 108 (1966).

(148) Bell, R.O., "Ferroelectrics and the Mossbauer Effect", Thesis for Ph.D. in Physics, Boston University, (1968).

(149) Dash, J. G., R. D. Taylor, D. E. Nagle, P.P. Craig, and W. M. Visscher, Phys. Rev. 122, 1116 (1961).

(150) Steyert, W. A. and R. D. Taylor, Phys. Rev., 134, A716 (1964).

(151) Muir, A. H., Jr., K. J. Ando, and H. M. Coogan, "Mossbauer Effect Data Index". (J. C. Wiley, New York, 1966).

(152) Birks, L. S., Electron Probe Micronanalysis, (Interscience, New York, 1963). p. 201.

APPENDIX I.

PARLORS COMPUTER PROGRAM MODIFIED FOR IBM 360-50

This program[147] makes a least square fit of the data to as many as twenty-one Lorentzian line shapes and a background parabola. This parabola approximates the effects of nonlinearity in the drive or certain geometric effects due to the source moving with respect to the detector. The basic equation to be fitted is:

$$y(x) = \left(\sum_{1=1}^{n} \frac{A_i}{1 + h_i(x - p_i)^2}\right) + E + Fx + Gx^2 \qquad \text{(A-I-1)}$$

where A_i is the height of peak i,

p_i is the position of peak i,

h_i is the inverse square of the HWHM of peak i.

The peaks are fitted using the criterion that:

$$S = \sum_{j=1}^{n} [y_j(\text{obs.}) - y_j(\text{calc.})] \text{ be a minimum.} \qquad \text{(A-I-2)}$$

To make the calculation easier, the equation (A-I-1) is linearized by first setting:

$$h_i = H_i + \delta_i \text{ with } \delta_i \ll H_i, \text{ and}$$

$$p_i = P_i + \gamma_i \text{ with } \gamma_i \ll P_i.$$

The result is then expanded using the binomial theorem, and higher powers of γ_i and δ_i are neglected to give:

$$y_j = \sum_{1=1}^{n} \left[\frac{A_i}{Q_{ij}} + \frac{2A_i H_i (x_j - p_i)\gamma_i}{Q_{ij}^2} - \frac{A_i (x_j - p_i)^2 \delta_i}{Q_{ij}^2} \right] +$$

$$+ E + F\, x_j + G\, x_j^2 \qquad \text{(A-I-3)}$$

where: $Q_{ij} = (1 + H_i (x_j - p_i)^2)$.

This is then minimized according to equation (A-I-2) to form the matrix elements of the least square matrix equation.

The program calculates the parameters; A_i, E, F, G, γ_i, and δ_i, from which new values of P_i and H_i are calculated and the next iteration is begun. The program stops if the difference between iterations is less than the specified error or specified number of iterations, whichever comes first. The program also faults if the matrix is singular, because no unique inverse can be found for it. The program tries to make adjustment for large errors by altering the halfwidth until usable values are obtained.

The program prints out the parameters of the fit, error analysis, and plots of the data and fit. The error analysis is described in NBS technical note #404.[147] The program consists of the main control program and three subroutines; READLD, DPINVS, and PARLOR. The first reads in the data and prepares it for analysis. PARLOR does the main curve fitting and output control including the plotting and error analysis. DPINVS is a double precision matrix inversion routine used in solving the least square matrix.

The data cards are arranged in the following order:

I. NSETS is the number of data sets to be analyzed, Format (I2).

II. The following list of cards is to be placed in front of each data set, except as noted for channels 400-201 in one of the options of MO (4).

1. MO(1) = 0, Plots on Calcomp Plotter. (4I2)
   = 1, Plots on High Speed Printer.

2. MO(2) = 0, Does not plot Residuals on Printer.
   = 1, Plots Residuals on Printer.

   MO(3) = 0, Does not print out calc. and expt. data.
   = 1, Prints out calc. and expt. data and residuals.

   MO(4) = 0, Analyzes 400 data points.
   < 0, Folds 400 data points and analyzes as one set of 200 data points.
   > 0, Analyzes first 200 data points and the second 200 data points separately as two data fits.
   = 2, Subtracts Beryllium Impurity correction.
   = 1, No Beryllium correction.

2. IT is maximum number of iterations to be allowed.
   ER is the maximum error to be allowed. (I2,F14.4)

3. OV is number of overflows in 10^6 memory in data. (F4.0)

4. ALABL(I), I = 1,18; Data Label, first 48 characters
5. ALABL(I), I = 19,36; label plots, last 72 characters
6. ALABL(I), I = 37,54; label number of data points analyzed. (18A4).

7. FØ is background correction factor, (4F10.7)
   PØ is position of beryllium correction peak,
   HØ is the half width of Be correction peak,
   RØ is the relative height of Be correction peak.

8. J is the channel number of a bad channel (I3).
   Numbering is on basis of 1 - 400, or if analyzing data in 400 - 201 range, J = 400 - $J_{observed}$.
   Blank card terminates set of J.

9. R1 is position of peak in spectrum (guess) (3F7.4)
   R2 is half width of peak in spectrum
   ER1 is individual error limit for particular peak
   (ER1 = ER if not specified).
   One card per peak, terminated by blank card.

10. RW(J), J = 1,8; Data Cards (8(4x,F6.0))
    25 cards if MO(4) > 0 and 50 cards otherwise.

11. VEL is Velocity per channel in mm/sec (2F10.6,I2)
    XZERO is the channel having zero velocity
    NVEL = 0 No velocity scale on plot
    = 1 Velocity scale on plot
    = 2 Velocity scale and resolved Lorentzian peaks are plotted (Useful in case of overlapping peaks).

Several special features of the program, not discussed in the NBS notes,[147] are discussed here. They are the beryllium correction, background correction and the variable data input.

The beryllium correction was introduced when an impurity peak was observed in the spectrum and was thought to be due to iron in the beryllium foils used in the furnace and counter tube window. It has since been found that the fault was in an aluminum foil filter used to reduce the X-ray intensity. To use this feature which amounts to stripping the spectrum of a single Lorentzian having the parameters specified by PØ, HØ, RØ on data card number 7. To use the routine, MO(4) must have the absolute value of 2. If the beryllium correction is made, the output specifies the peak parameters and states that the correction has been made.

The background correction is used to get relative area fractions by subtraction of the non-14 kev radiation that

gets into the counter and discriminator window. The value of FØ gives the experimentally determined ratio of the background count rate to the total count rate. The total count is measured by using a scaler to count the events stored during one minute. The background count is measured by placing a .005 inch Brass filter between the Source and Detector, to eliminate the 14 kev radiation, and then observing the count rate for one minute again.

$$F\emptyset = \frac{\Sigma\, y_{background}}{\Sigma\, y_{observed}} \qquad \text{(A-I-5)}$$

where $\Sigma y_{observed} = A_{parabola} - A_{peaks}$. (A-I-6)

This gives the final correction as

$$F = \frac{y_{background}}{y_{maximum}} = F\emptyset \cdot (1 - \frac{A_{peak}}{A_{parabola}}) \qquad \text{(A-I-7)}$$

where A is area,

y is number of counts.

This gives the area fraction to be:

$$\text{AREA FRACTION} = \frac{A_{peaks}}{y_{maximum}(1 - F)} \qquad \text{(A-I-8)}$$

where $y_{maximum}$ is determined from the value of the parabola at the position of the peak having area A_{peak}.

The data input is arranged for use with both a triangle wave spectrum or a flyback spectrum. For the triangle wave, two mirror image spectrum are generated in channels 1-200 and 400 - 201 respectively. There are two options in

analyzing the data.

1. The data can be folded by adding the two halfs;

$$y(I) = y(I) + y(401 - I).$$

2. The data for each half can be analyzed separately.

The latter case is probably more useful since estimates of non-linearity and other errors can be obtained and corrected for. The folding routine is useful to subtract out the geometric background contribution present with large amplitudes of source motion. If the data is analyzed separately, only data cards II-6 on down have to be used for the second half of the spectrum.

For the flyback or sawtooth velocity waveform, the 0 - 400 channel data format is useful.

```
C       PARLORS--MOSSBAUER SPECTRA--FOLD-VEL-PRINT PLOT
C FIRST CARD (2I2)  NSETS=# OF CURVE FITS TO BE MADE
C  SECOND CARD (4I2) MO(1)=1 GIVES PRINT-PLOT, =0 GIVES PLOT-PLOT
C                    MO(2) = 1 GIVES RESIDUE PRINT-PLOT
C                    MO(3)=1 GIVES DATA, CALC,RESIDUE PRINT OUT
C       MO(4)=C 1-400 CHANNELS, .LT.0 FOLDS DATA,=2 CORRECTS FOR BE
C THIRD CARD (I2,F14.4) IT= NUMBER OF ITERATIONS TO BE MADE
C                       ER = CONVERGENCE CRITERION OF ITERATIONS
C  FOUPTH CARD (F4.0) OV= NUMBER OF OVERFLOWS IN MILLIONS
C CARDS 5,6,7 ARE LABEL CARDS FOR DATA SET (18A4)
C CARD 8 (4F10.6) FO = RATIO OF BACKGROUND TO TOTAL COUNTS
C         PO, HO, RO ARE POSITION, HALFWIDTH, AND RELATIVE HEIGHT OF BE
C NEXTCARDS ARE BAD CHANNELS, ONE PER CARD (I3) FOLLOWED BY A BLANK CARD
C THEN PEAK POSITION AND HALFWIDTH AND ERROR GUESSES, ONE PEAK PER CARD
C  PEAK GUESSES HAVE FORMAT (3F7.4), ARE FOLLOWED BY BLANK CARD
C DATA CARDS FOLLOW 8(4X,F6.0)
C IF NVEL .GT.0 AND MO(1)=0, CARD FOLLOWS DATA(2F10.6) VEL, XZERO
C   VEL = VELOCITY PER CHANNEL, XZERO= CHANNEL HAVING ZERO VELOCITY
C IF MO(4).GT.0, PLACE CARDS FROM 7 ON BEFOREDATA CARD STARTING WITH 200
C                    NVEL DECIDES IF PLOT INCLUDES VELOCITY SCALE
      NPLOT=C
      IDX=C
      READ (1,10) NSETS
10    FORMAT (I2)
      DO 20 I=1,NSETS
      CALL READLD(IDX)
```

```
0001              SUBROUTINE READLD(IDX)
0002              DOUBLE PRECISION A,B,C,H,H1,P,P1,AA,TEMP
0003              COMMON A(63,63),AA(63,63),B(63)
0004              COMMON Y(530),IG(530),P(21),H(21),ER1(21),IT,ER,EM,N1,N,
                 1ALABL(54),NL,IGN,MO(4),NDATA,FO
0005              DIMENSION RW(10)
0006              K=201
0007              IF (IDX.LT.0) GO TO 87
0008              READ (1,40) (MO(J),J=1,4)
0009        40    FORMAT (4I2)
0010              IDX=MO(4)
0011              K=0
0012              NDAT=25
0013              IF (MO(4).GE.1) GO TO 50
0014              NDAT = 2*NDAT
0015        50    READ (1,55) IT,ER
0016        55    FORMAT (I2,F14.4)
0017              NDATA = 8*NDAT
0018              READ (1,60) OV
0019        60    FORMAT (F4.0)
0020              IEXP=6.0
0021        930   READ (1,931) (ALABL(I),I=1,36)
0022        931   FORMAT (18A4)
0023        87    READ (1,931) (ALABL(I),I=37,54)
0024        118   WRITE (3,119)
0025        119   FORMAT(1H1)
0026        935   WRITE (3,121) (ALABL(I),I=1,54)
0027        121   FORMAT (1H ,18A4)
0028              FO=0.0
0029              READ (1,54) FO,PO,HO,RO
0030        54    FORMAT (4F10.6)
0031        65    DO 70 I=1,NDATA
0032        70    IG(I)=0
0033              DO 80 I=1,NDATA
0034              READ (1,75) J
0035        75    FORMAT (I3)
0036              IF(J.EQ.0) GO TO 86
0037              WRITE (3,76) J
0038        76    FORMAT(8X,15HBAD CHANNEL AT ,I3)
0039        80    IG(J)=1
0040        86    IGN=I-1
0041              DO 93 NL=1,21
0042              READ (1,94) R1,R2,ER1(NL)
0043              R4N(NL)=R1
```

```
0045              IF(ER1(NL).LT.1.0E-6) ER1(NL)=ER
0046              IF(P(NL).LT.1.0E-6) GO TO 95
0047        93    CONTINUE
0048        94    FORMAT (3F7.4)
0049        95    NL=NL-1
0050              DO 932 JK=1,NDATA
0051        932   Y(JK)=0.0
0052              DO 933 JK=1,NDAT
0053        9318  READ (1,934) (RW(J),J=1,8)
0054        9328  JKK=8*(JK-1)
0055        9338  DO 933 I=1,8
0056              IK=IABS(K-JKK-I)
0057        933   Y(IK)=RW(I)
0058              N1=1
0059              IF (MO(4).GE.0) GO TO 117
0060              DO 115 I=1,200
0061              IF (IG(401-I).NE.0) IG(I)=1
0062              IF (IG(I).NE.0) GO TO 115
0063              Y(I)=Y(I)+Y(401-I)
0064          115 CONTINUE
0065              NDATA=NDATA/2
0066        117   EM=0.0
0067        106   DO 111 N=1,NDATA
0068              IF(IG(N).NE.0) GO TO 111
0069        109   IF(Y(N).LT.1.0E-6) GO TO 112
0070              IF(Y(N).GT.EM) EM=Y(N)
0071        111   CONTINUE
0072              N=NDATA
0073              GO TO 113
0074        112   N=N-1
0075        934   FORMAT (8(4X,F6.0))
            C CORRECT FOR COUNT OVERFLOW,NORMALIZE Y, PRINT ALPHANUMERIC DATA
0076          113 EM=EM + OV*(10.**IEXP)
0077              DO 128 I=1,NDATA
0078        116   Y(I)=Y(I)+OV*(10.**IEXP)
0079        127   Y(I)=Y(I)/EM
0080        128   Y(I)=(Y(I)-FO)/(1.-FO)
            C Y = NORMALIZED COUNTS
0081              IDX=-IDX
0082              IF (IABS(IDX).EQ.2) GO TO 130
0083        122   RETURN
0084        130   DO 131 I=1,200
0085              C=I
0086              Z=RO/(1.0+((C-PO)/HO)**2)
0087              Y(I)=Y(I)+Z
0088        131   CONTINUE
0089              WRITE(3,133)
0090          133 FORMAT (35HOBERYLLIUM-IRON IMPURITY SUBTRACTED)
0091              WRITE (3,134) PO,HO,RO
0092        134   FORMAT(4X,15HPEAK POSITION =,F10.6,3X,11HHALFWIDTH =,F10.6,
                 13X,8HHEIGHT =,F10.6)
0093              GO TO 122
0094              END
```

```
0001          SUBROUTINE DPINVS(N,K,ISIG)
        C DOUBLE PRECISION MATRIX INVERSION AND EQUATION SOLVING WITH SELECTIVE
        C PIVOTING
        C A=ORIGINAL MATRIX, AINV = INVERSE, N = NUMBER OF ROWAS OF A. B = CON
        C STANTS OF SIMULTANEOUS EQUATIONS. SOLUTION REMAINS IN B
        C K OF -1,0, 1, INDICATES SOLVE EQUATIONS, INVERT A, BOTH, RESPECTIVELY
0002          DOUBLE PRECISION A,AINV,C,HOLD,B,X,Z,H,P
0003          COMMON A(63,63),AINV(63,63),B(63)
0004          COMMON Y(530),IG(530),P(21),H(21),ER1(21),IT,ER,EM,N1,NO,
             1ALABL(54),NL,IGN,MO(4),NDATA,FO
0005          ISIG=0
0006          IF(K.LT.0) GO TO 20
0007          DO 15 I=1,N
0008          DO 15 J=1,N
0009          IF(I.EQ.J)   GO TO 10
0010          AINV(I,J)=0.
0011          GO TO 15
0012    10    AINV(I,J)=1.
0013    15    CONTINUE
0014    20    DO 65 L=1,N
0015          C=0.
        C DETERMINE MAX ABS OF VARIABLE TO BE ELIMINATED
0016          DO 25 J=L,N
0017          X=DABS(A(J,L))
0018          IF (X.LE.C) GO TO 25
0019          C=X
0020          J1=J
0021    25    CONTINUE
        C J1 IS ROW HAVING GREATEST ABS,C IS THIS VALUE
0022    26    IF((C-1.0E-8).LE.0.) GO TO 120
        C INTERCHANGE ROWS L AND J1 IF THEY ARE NOT THE SAME
0023          IF(J1.EQ.L) GO TO 40
0024          DO 28 J=L,N
0025          HOLD=A(L,J)
0026          A(L,J)=A(J1,J)
0027    28    A(J1,J)=HOLD
0028          IF (K.LT.0) GO TO 35
0029          DO 32 J=1,N
0030          HOLD = AINV(L,J)
0031          AINV(L,J)=AINV(J1,J)
0032    32    AINV(J1,J) = HOLD
0033          IF (K.EQ.0) GO TO 40
0034    35    HOLD=B(L)
0035          B(L)=B(J1)
0036          B(J1)=HOLD
0037    40    CONTINUE
```

```
C ZERO ALL ELEMENTS IN THE LTH COLUMN BUT THE PIVOTAL ELEMENT
      DO 60 I=1,N
      IF(I.EQ.L) GO TO 60
      Z=A(I,L)/A(L,L)
      DO 45 J=L,N
45    A(I,J)=A(I,J) - Z*A(L,J)
      IF(K.LT.0) GO TO 55
      DO 50 J=1,N
50    AINV(I,J) = AINV(I,J) - Z*AINV(L,J)
      IF(K.EQ.0) GO TO 60

55    B(I)=B(I)-Z*B(L)
60    CONTINUE
65    CONTINUE
C DIVIDE BY DIAGONAL ELEMENTS
68    DO 95 L=1,N
      Z=A(L,L)
      DO 70 J=L,N
70    A(L,J) = A(L,J)/Z
      IF (K.LT.0) GO TO 80
      DO 75 J=1,N
75    AINV(L,J) = AINV(L,J)/Z
      IF(K.EQ.0) GO TO 95
80    B(L)=B(L)/Z
95    CONTINUE
      GO TO 150
120   ISIG=-1.
      WRITE (3,130)
130   FORMAT(///20X,42H MATRIX IS SINGULAR, NO INVERSE OBTAINABLE ///)
150   RETURN
      END
```

```
0001              SUBROUTINE PARLOR (NPLOT,IDX)
0002              DOUBLE PRECISION A,B,C,H,H1,P,P1,AA,TEMP
0003              COMMON A(63,63),AA(63,63),B(63)
0004              COMMON Y(530),IG(530),P(21),H(21),ER1(21),IT,ER,EM,N1,N,
                 1ALABL(54),NL,IGN,MO(4),NDATA,FO
0005              DIMENSION VARA(20),VARP(20),VARS(20),BASE(20),VARG(20),VARB(20)
0006              DIMENSION P1(20),R(20),H1(20),DA(20),S1(20),G(20),Y2(530),R1(530)
0007              DIMENSION IPP(6),IRP(16),PLOT(120)
0008              DIMENSION YA(400),YB(400),YD(400),XD(400)
0009              DIMENSION TARM(20),FARM(20)
0010              DATA PD/1H+/,STAR/1H*/,BLANK/1H /
0011              READ (1,1000) VEL,XZERO,NVEL
0012        1000  FORMAT (2F10.6,I2)
0013              L1=3*NL+3
0014              DO 157 I=1,NL
0015              H(I)=1.0/(H(I)*H(I))
0016        157   DA(I)=0.0
0017              LIM=0
0018              LIMO=0
0019              GO TO 170
0020        165   DO 167 I=1,NL
0021        167   DA(I)=R(I)
            C FILL LEAST SQUARES MATRIX
0022        170   DO 200 J=1,L1
0023              AA(J,1)=0.0
0024              DO 200 I=1,L1
0025              A(I,J)=0.0
0026        200   CONTINUE
0027              DO 301 K=N1,N
0028              IF(IG(K).NE.0) GO TO 301
0029              C=K
0030              DO 250 I=1,NL
0031              J=3*I
0032              B(J-2)=1./(1.+H(I)*(C-P(I))**2)
0033              B(J-1)=B(J-2)*B(J-2)*(C-P(I))
0034        250   B(J)=B(J-1)*(C-P(I))
0035              DO 260 I=1,3
0036              KKK=L1-3+I
0037        260   B(KKK)=C**(I-1)
0038              DO 300 J=1,L1
0039              AA(J,1)=AA(J,1) + B(J)*Y(K)
0040              DO 300 I=1,J
0041              A(I,J)=A(I,J)+B(I)*B(J)
0042        300   CONTINUE
0043        301   CONTINUE
```

```
0044            DO 310 I=1,L1
0045      310   B(I)=AA(I,1)
          C SOLVE LEAST SQUARES MATRIX
0046            DO 320 J=1,L1
0047            DO 320 I=1,J
0048            AA(I,J)=A(I,J)
0049            AA(J,I)=A(I,J)
0050      320   A(J,I)=A(I,J)
0051      350   CALL DRINVS (L1,-1,ISIG)
0052            IF(ISIG.NE.0) GO TO 980
          C CORRECT PEAK LOCATION AND HALF-WIDTH, IF OK PRINT RESULTS

0053            DO 400 IQ=1,NL
0054            JQ=3*IQ
0055            R(IQ)=B(JQ-2)
          C R IS NORMALIZED
0056            H1(IQ)=-B(JQ)/R(IQ)
0057            IF((H(IQ)+H1(IQ)).GT.0.) GO TO 400
0058            X2=H(IQ)+H1(IQ)
0059            LIMQ=LIMQ+1
0060            IF(LIMQ.GT.10) GO TO 375
0061            H(IQ)=1.1*H(IQ)
0062            GO TO 390
0063      375   IF(LIMQ.GT.20) GO TO 410
0064            IF(LIMQ.EQ.11) H(IQ)=H(IQ)/((1.1)**10)
0065            H(IQ)=H(IQ)/1.1
0066      390   X1=1./DSQRT(H(IQ))
0067            WRITE (3,405) IQ,X1,X2
0068      405   FORMAT(//10X,29HHALF-WIDTH CORRECTED FOR PEAK,I4,4H  TO,F7.2,25H,
               1   ATTEMPTED SOLUTION =,F9.3)
0069            GO TO 165
0070      400   CONTINUE
0071            GO TO 430
0072      410   WRITE (3,412) IQ
0073      412   FORMAT(//34H WRONG HALFWIDTH ESTIMATE FOR PEAK,I5)
0074            GO TO 980
0075      430   WRITE (3,435)
0076      435   FORMAT(//9X,4HPEAK,5X,12HNEW POSITION,7X,13HNEW HALFWIDTH,9X,10HNE
               1W HEIGHT,10X,8HNEW AREA)
0077            LIMQ=0
0078            DO 450 I=1,NL
0079            J=3*I
0080            P1(I)=B(J-1)/(2.*H(I)*R(I))
0081            P(I)=P(I)+P1(I)
0082            H(I)=H(I)+0.9*H1(I)
0083            S1(I)=1./DSQRT(H(I))
0084            R(I)=R(I)*EM*(1.-F0)
          C P IS NOW UNNORMALIZED. WILL REMAIN SO UNTIL NEXT ITERATION
```

```
      C(I)=S1(I)*R(I)*3.1415926
  450 WRITE (3,455) I,P(I),S1(I),P(I),C(I)
  455 FORMAT(8X,I3,4E20.8)
C TEST NUMBER OF ITERATIONS AND CONVERGENCE
      LIM=LIM+1
      IF(LIM.LE.IT) GO TO 457
      WRITE (3,456)
  456 FORMAT(//20X,53HCONVERGENCE NOT MET IN SPECIFIED NUMBER OF ITERATI
     1ONS,//)
      GO TO 980
  457 DO 460 I=1,NI
      IF(DABS(H1(I)/H(I)).GT.ER1(I)) GO TO 165
      IF(DABS(P1(I)/P(I)).GT.ER1(I)) GO TO 165
      IF(ABS((R(I)-OA(I))/R(I)).GT.ER1(I)) GO TO 165
C PRINT FIT AND DATA FOR EACH CHANNEL. FIND MAXIMUMS
  460 CONTINUE
      PARA0 = B(L1-2)*EM*(1.-FO)
      PARA1 = B(L1-1)*EM*(1.-FO)
      PARA2 = B(L1)*EM*(1.-FO)
      RM = PARA0 - PARA1*PARA1/(4.*PARA2)
      XO=-PARA1/(2*PARA2)
      YM=0.
      Y2M=0.
      RM=0.
      S=0.
      JRM=0
      PARM=0
      CARM=0.
      OARM=0.
      DO 500 K=N1,N
      IF(IG(K).NE.0) GO TO 500
      Y2(K)=0.
      C=K
      DO 480 I=1,NL
  480 Y2(K)=Y2(K)+R(I)/(1.0+H(I)*(C-P(I))**2)
      PAR=PARA0+C*PARA1+C*C*PARA2
      PARM=PARM+PAR
      Y(K)=Y(K)*EM*(1.-FO)-PAR
C Y NOW EQUALS UNNORMALIZED COUNTS-PARABOLA
      OARM=OARM+Y(K)
      CARM=CARM+Y2(K)
      R1(K)=Y(K)-Y2(K)
      IF(YM.GT.Y(K)) YM=Y(K)
      Z=ABS(R1(K))
      IF (RM.LT.Z) JRM=K
      IF (RM.LT.Z) RM=Z
      IF (Y2M.GT.Y2(K)) Y2M=Y2(K)
      S=S+R1(K)*R1(K)
  500 CONTINUE
```

```
      D=N-N1-IGN-L1
      D=SQRT(S/D)
      WRITE (3,510) D,RM,JRM
510   FORMAT(///8X,30HAVERAGE MEAN SQUARE RESIDUAL =,E18.8,//8X,18HMAXIM
     1UM RESIDUAL =,E18.8,3X,10HAT CHANNEL,I6,/)
      DRM=D/RM
      WRITE (3,515) DRM
515   FORMAT(8X,47HAVERAGE MEAN SQUARE RESIDUAL/MAXIMUM RESIDUAL =,E18.8
     1,/)
      WRITE (3,520) EM,Y2M
520   FORMAT(8X,26HMAXIMUM NUMBER OF COUNTS =,F10.0,8X,22HCALC. MAXIMUM
     1COUNTS =,F10.0/)
      SEM=SQRT(EM)
      SEMA=D/SEM
      WRITE (3,521) SEM,SEMA
521   FORMAT(8X,27HSQ RT OF MAX NO. OF COUNTS= ,E18.8,8X,42HAVG MEAN SQ
     1RESIDUAL/SQ RT MAX NO. COUNTS= , E18.8/)
      WRITE (3,523) PARA0,PARA1,PARA2
523   FORMAT(8X,11HPARABOLA =(,E15.8,5H) + (,E15.8,10H)*CHNL + (,E15.8,
     111H)*CHNL*CHNL,/)
      WRITE (3,524) RM,PARA2,XO
524   FORMAT(8X,12HPARABOLA = (,F12.2,5H) + (,F12.6,8H) * (X -,F12.8,4H)
     1**2/)
      WRITE (3,526)
      ARM=0.0
      TARMT=0.0
      FARMT=0.0

      ALARM=1./(1.+CARM/PARM)
      DO 525 I=1,NL
      BASE(I)=PARA0+PARA1*P(I)+PARA2*P(I)*P(I)
      TARM(I)=G(I)/BASE(I)
      FARM(I)=TARM(I)*ALARM
      TARMT=TARMT+TARM(I)
      FARMT=FARMT+FARM(I)
      WRITE (3,527) I,G(I),TARM(I),FARM(I)
525   ARM=ARM + G(I)
      AP2=CARM/RM
      AN2=AP2*ALARM
      AP3=DARM/RM
      AN3=AP3*ALARM
      WRITE (3,528) DARM,AP3,AN3
      WRITE (3,529) CARM,AP2,AN2
      WRITE (3,530) ARM,TARMT,FARMT
      WRITE (3,531) ALARM
```

```
0168        526   FORMAT (17X,15HLORENTZIAN AREA,10X,15HNORMALIZED AREA,5X,25HCORREC
                 1TED BACKGROUND AREA)
0169        527   FORMAT (5X,4HPEAK,I3,7X,F15.3,10X,F15.3,10X,F15.3)
0170        528   FORMAT(5X,4HEXPT,10X,F15.3,10X,F15.3,10X,F15.3)
0171        529   FORMAT(5X,4HCALC,10X,F15.3,10X,F15.3,10X,F15.3)
0172        530   FORMAT(5X,5HTOTAL,9X,F15.3,10X,F15.3,10X,F15.3)
0173        531   FORMAT(5X,30HBACKGROUND CORRECTION FACTOR =,F8.4)
              C CALCULATE SUBTRACT MATRIX AND PRINT
              C SUBTRACT MATRIX-LOWER TRIANGLE=AVERAGE POSITION OF THE TWO PEAKS
              C SUBTRACT MATRIX-UPPER TRIANGLE=DISTANCE BETWEEN THE TWO PEAKS
0174              IF(NL.GT.16) GO TO 730
0175              WRITE (3,705)
0176        705   FORMAT (1H1, 20X)
0177              DO 709 I=1,16
0178        709   IRP(I)=I
0179              WRITE (3,710) (ALABL(I),I=1,16),(IRP(I),I=1,NL)
0180        710   FORMAT (1X,16A4,///10X,16HSUBTRACT MATRIX ,///1X,4HPEAK,16I7)
0181              DO 715 I=1,NL
0182              DO 715 J=1,I
0183              A(J,I) = P(I) - P(J)
0184        715   A(I,J) =(P(I)+P(J))/2.
0185              DO 716 I=1,NL
0186              WRITE (3,720) I,(A(I,J),J=1,NL)
0187        716   CONTINUE
0188        720   FORMAT (/1X,I3,3X,16F7.2)
0189              WRITE (3,721) (IRP(I),I=1,NL)
0190        721   FORMAT(//29X,20HAREA FRACTION MATRIX,///1X,4HPEAK,16I7)
0191              DO 725 I=1,NL
0192              A(I,I)=G(I)/ARM
0193              I1=I+1
0194              DO 725 J=I1,NL
0195              A(I,J) = G(I)/G(J)
0196        725   A(J,I) = G(J)/G(I)
0197              DO 731 I=1,NL
0198        731   WRITE (3,720) I,(A(I,J),J=1,NL)
0199        730   CONTINUE
              C PRINT FINAL PARAMETERS, DO ERROR ANALYSIS, PRINT RESULTS
0200              WRITE (3,735)
0201        735   FORMAT(1H1,20X)

0202        741   WRITE (3,740) (ALABL(I),I=1,54)
0203        740   FORMAT(12X,18A4)
0204              WRITE (3,745)
0205        745   FORMAT(//24X, 10HFINAL DATA)
0206              WRITE (3,750)
0207        750   FORMAT(//16X,4HPEAK,3X,14HFINAL POSITION,3X,15HFINAL HALFWIDTH,7X,
                 112HFINAL HEIGHT,9X,10HFINAL AREA,10X,9HBASE-LINE)
```

```
      DO 770 I=1,NL
      WRITE (3,760) I,P(I),S1(I),R(I),G(I),BASE(I)
760   FORMAT(15X,I4,F14.3,F17.3,5X,3E20.8)
770   CONTINUE
      WRITE (3,772) ARM
772   FORMAT(75X,E20.8)
      WRITE (3,775) PARA0,PARA1,PARA2
775   FORMAT(//17X,4HA0 =,E18.8,/17X,4HA1 =,E18.8,/17X,4HA2 =,E18.8)
      WRITE (3,780)
780   FORMAT(//24X,14HERROR ANALYSIS,//16X,4HPEAK,3X,14HVAR.  POSITION,
     13X,15HVAR.  HALFWIDTH,7X,12HVAR.  HEIGHT,9X,10HVAR.  AREA,7X,15HVA
     2R.  BASE-LINE)
      DO 781 II=1,63
      DO 781 JJ=1,63
      TEMP=AA(II,JJ)
      AA(II,JJ)=A(II,JJ)
781   A(II,JJ)=TEMP
800   CALL DRINVS(L1,0,ISIG)
      IF(ISIG.NE.0) RETURN
      DO 782 II=1,63
      DO 782 JJ=1,63
      TEMP =AA(II,JJ)
      AA(II,JJ)=A(II,JJ)
782   A(II,JJ)=TEMP
      VRPR0=D*DSQRT(A(L1-2,L1-2))
      VRPR1=D*DSQRT(A(L1-1,L1-1))
      VRPR2=D*DSQRT(A(L1,L1))
      DO 825 I=1,NL
      VARA(I)=D*DSQRT(A(3*I-2,3*I-2))
      COVA = A(3*I-2,3*I-2)/(B(3*I-2)*B(3*I-2))
      COVE = A(3*I,3*I)/(B(3*I)*B(3*I))
      COVAE = A(3*I-2,3*I)/(B(3*I-2)*B(3*I))
      VARH = (COVA+COVE-2.0*COVAE)*H1(I)*H1(I)
      VARS(I)=D*S1(I)*SQRT(VARH)/(2.0*EM*H(I))
      COVD=A(3*I-1,3*I-1)/(B(3*I-1)*B(3*I-1))
      COVXH=4.0*H(I)*H(I)*A(3*I-2,3*I-2)-8.0*H(I)*A(3*I-2,3*I)
      COVXH=(COVXH+4.0*A(3*I,3*I))/(2.0*H(I)*B(3*I-2)-2.0*B(3*I))**2
      COVYXH=(2.0*H(I)*A(3*I-2,3*I-1)-2.0*A(3*I-1,3*I))
      COVYXH=COVYXH/(B(3*I-1)*(2.0*B(3*I-2)*H(I)-2.0*B(3*I)))
      VARP(I)=D/EM*SQRT(COVD+COVXH-2.0*COVYXH)*DABS(P1(I))
      VARG(I)=(ABS(VARS(I)/S1(I)) + ABS(VARA(I)/R(I)))*ABS(G(I))
      VARB(I)=VRPR0+VRPR1+VRPR2
      WRITE (3,820) I,VARP(I),VARS(I),VARA(I),VARG(I),VARB(I)
820   FORMAT(15X,I4,F14.3,F17.3,5X,3E20.8)
825   CONTINUE
      WRITE (3,830) VRPR0,VRPR1,VRPR2
830   FORMAT(//17X,9HVAR. A0 =,E18.8,/17X,9HVAR. A1 =,E18.8, /17X,9HVAR.
     1 A2 =,E18.8)
901   IF (M0(1)) 902,950,910
```

```
      902   IF(MO(2).EQ.1) GO TO 911
      903   IF(MO(3).EQ.1) GO TO 912
      905   RETURN
      910   DO 920 J=N1,N
            NP1=100.*Y(J)/Y2M + 6.
            NP2 = 100.*Y2(J)/Y2M + 6.
            DO 921 K=1,115
            PLOT(K)=BLANK
            IF(IG(J).NE.0) GO TO 921
            IF(K.EQ.NP2) PLOT(K)=PD
            IF(K.EQ.NP1) PLOT(K)=STAR
      921   CONTINUE
      920   WRITE (3,922) J,(PLOT(K),K=1,115)
      922   FORMAT (1H ,I3,1H.,115A1)
            GO TO 902
      911   NSEM=50.*SEM/RM
            DO 930 J=N1,N
            NP1=51. - 50.*R1(J)/RM
            DO 931 K=1,115
            PLOT(K)=BLANK
            IF(K.EQ.(51-NSEM)) PLOT(K)=PD
            IF(K.EQ.51) PLOT(K)=PD
            IF(K.EQ.(51+NSEM)) PLOT(K)=PD
            IF(IG(J).NE.0) GO TO 931
            IF(K.EQ.NP1) PLOT(K)=STAR
      931   CONTINUE
      930   WRITE (3,922) J,(PLOT(K),K=1,115)
            GO TO 903
      912   WRITE (3,940)
      940   FORMAT(1X,40H DATA LESS PARABOLA (FIRST LINE) AND FIT)
            NDA=NDATA/10
            DO 941 J=1,NDATA
            R1(J)=R1(J)/SEM
            Y(J)=Y(J)/Y2M
      941   Y2(J)=Y2(J)/Y2M
            DO 942 J=1,NDA
            DO 943 K=1,10
            KK=10*(J-1) + K
            IG(K)=KK
            R1(K)=R1(KK)
            Y2(K)=1.0-Y2(KK)
      943   Y(K)=1.0-Y(KK)
            WRITE (3,944) (IG(K),Y(K),K=1,10)
            WRITE (3,945) (IG(K),Y2(K),K=1,10)
      942   WRITE (3,946) (IG(K),R1(K),K=1,10)
      944   FORMAT (1H0,10(I4,1H ,F6.3))
      945   FORMAT (1H ,10(I4,1H*,F6.3))
      946   FORMAT (1H ,10(I4,1HR,F6.3))
            RETURN
```

```
C PLOTTER ROUTINE
950     IF (NPLOT.GT.0) GO TO 951
        CALL PENPOS ('CANNER,J.P.',11,1)
  951   CALL NEWPLT (10.0,2.0,10.5)
        DATA=NDATA
        CALL ORIGIN (DATA,0.0)
        CALL YSCALE (0.0,1.20,6.0)

        CALL YAXIS (0,1)
        IF (NVEL.LE.0) GO TO 961
        XMIN=-XZERO*VEL
        XMAX=(DATA-XZERO)*VEL
        DIN=DATA/200.0
        XOIN=2.0+0.04*XZERO/DIN
        CALL NEWPLT (XOIN,8.0,10.5)
        CALL ORIGIN (0.0,1.2)
        CALL XSCALE (XMIN,XMAX,8.0)
        CALL XAXIS (0,5)
        CALL YSCALE (0.0,1.20,6.0)
        IF (NVEL.EQ.1) GO TO 957
        DO 956 J=1,NL
        RAM=R(J)
        POS=P(J)
        BETA=S1(J)
        N3=POS-2.*BETA
        N4=POS+2.*BETA
        N5=N4-N3+1
        K=0
        DO 952 I=1,N5
        II=I-K
        C=N3+I-1
        XD(II)=(C-XZERO)*VEL
        YD(II)=1.05-RAM/((1.0+((C-POS)/BETA)**2)*Y2M)
        IF ((XMIN-XD(II)).GT.0) K=K+1
        IF ((XMAX-XD(II)).LT.0) GO TO 953
952     CONTINUE
        N2=N5-K
        GO TO 954
953     N2=I-K-1
954     CALL XYPLT (XD,YD,N2,1,-1)
956     CONTINUE
957     J=XMAX
        I=XMIN
  958   IF ((J-I).LT.0) GO TO 960
        X=I
        XIN=XSTOIN(X)-0.14
        CALL NUM (XIN,-0.20,0.105,X,0.0,-1)
```

```
      I=I+1
      GO TO 958
  960 CONTINUE
      XTIN=5.0-XOIN
      CALL SYM (XTIN,0.10,0.14,'VELOCITY (MM/SEC)',0.0,17)
  961 CALL NEWPLT (2.0,2.0,10.5)
      CALL ORIGIN (1.0,0.0)
      CALL YSCALE (0.0,1.20,6.0)
      CALL YAXIS (0.1)
      DO 962 L=1,13
      YC=(L-1)*0.5-0.07
      YON=0.0+(L-1)*0.1
      CALL NUM (-0.50,YC,0.105,YON,0.0,1)
  962 CONTINUE
      CALL SYM (-0.7,2.0,0.14,'INTENSITY',90.0,9)
      DO 955 I=1,NDATA
      YA(I)=1.05-Y2(I)/Y2M

      YB(I)=1.05-Y(I)/Y2M
  955 IF (IO(I).NE.0) YB(I)=YA(I)
  965 CALL TSCALE (1.0,DATA,8.0)
      CALL TAXIS (10.0)
      CALL TPLT (YA,NDATA,1,-1)
      CALL TPLT (YB,NDATA,2,3)
      DATON=DATA/20.0
      DO 968 L=1,21
      TD=(L-1)*0.4-0.14
      TON=(L-1)*DATON
      IF (MO(4)+IDX.LE.0) GO TO 967
      TON=400.0-TON
  967 CONTINUE
      CALL NUM (TD,-0.18,0.105,TON,0.0,-1)
  968 CONTINUE
  969 CALL SYM (2.75,-0.4,0.14,'CHANNEL-NUMBER',0.0,14)
  970 CONTINUE
      CALL SYM (1.0,6.3,0.14,ALABL,0.0,48)
      CALL ENDPLT
      NPLOT=NPLOT+1
      GO TO 902
  980 DO 981 I=N1,N
  981 Y(I)=Y(I)*FM
      WRITE (3,982)((I,Y(I)),I=N1,N)
  982 FORMAT (10(1X,I3,1X,F8.0))
      RETURN
      END
```

APPENDIX II.

LORLSF COMPUTER PROGRAM

This program obtained from Dr. R. O. Bell[148] was used at Boston University by Dr. Gilbert Hoy's group. This program was adapted to fit two peaks having equal heights and widths, in cases where resolution of the two peaks was impossible using the PARLORS program. The data is fitted to the following equation:

$$y = a_1 + a_2(x - 100.5)^2 + \tfrac{1}{2}a_3\left[\frac{1}{1 + a_5^2(x-a_6-a_4)^2} + \frac{1}{1 + a_5^2(x-a_6+a_4)^2}\right] \quad \text{(A-II-1)}$$

where: a_1, a_2 are parameters for the background parabola,

a_3 is twice the height of the individual peak,

a_4 is half the splitting of the two peaks,

a_5 is the inverse full width at half maximum

a_6 is the center of gravity of the two peaks.

The method used in this program is to make a Taylor series expansion of y in term of a_1, a_2, a_3, a_4, a_5, a_6, and then to make a least squares fit. Terms of higher order are not included in the expansion. The rms error is then calculated and a delta error is found for each parameter which is used to make a new guess for each parameter for the next iteration. The program goes through a fixed number of iterations since convergence is slow and depends strongly on initial guesses.

The input has been made to conform with the PARLORS format as much as possible. The required cards are:

I. NSETS is number of data sets to be analyzed. (2I3)

IDX = 0, Analyzes 400 data points,
= 1, Analyzes first 200 data points and then the second 200 data points separately as two data fits. Second data set starts with card #5.

II. These cards appear in each data set, except for second half if IDX = 1, when only cards 5 to 11 are needed.

1. MAX is Channel number of last data point, (3I4)
MIN is Channel number of first data point,
MPLOT = 0, Data is plotted on printer,
= 1, Data is plotted on plotter.

2. OV is number of overflows of 10^6 memory to be added to the data. (F4.0)

3. ALABL(I), I=1-18, Labels data, First 48 characters label plots
4. ALABL(I), I=19-36, Last 72 characters label each
5. ALABL(I), I=37-54, half of the spectrum separately. (18A4).

6. FØ is background correction parameter (4F10.4)
PØ is position of beryllium correction peak
HØ is the half width of Be correction peak,
RØ is the relative height of the Be correction

7. RW(J), J=1-8, Data cards, 25 cards for IDX=1,
50 cards for IDX=0
(8(4X,F6.0))

8. XZERO is channel having zero velocity (2F10.6, I2)
VEL is velocity per channel in mm/sec,
NVEL = 0, No velocity scale on plot,
= 1, Velocity scale on plot,
= 2, Velocity scale on plot and plots the two peaks separately.

9. A(1) is baseline normalized to about 1.03 (2F8.6)
A(2) is the parabolic contribution parameter, about zero,

10. A(3) is twice the height of the single peak
A(4) is half of the peak splitting

11. A(5) is the full width at half maximum
    A(6) is the center between the two peaks.

The program consists of three parts, the main least square analyais part, and two subroutines, DRAW which plots the data, and MATINV, which inverts the least squares matrix. The same program can be modified to fit any number of peaks having the same linewidth, or to fit other specified constraint equations by altering the Taylor Series coefficients.

```
                C LORLSF PROGRAM FOR MULTICHANNEL SCALING FOR A TRIANGLE DRIVE
                C     THIS PROGRAM MAKES A LEAST SQUARE FIT TO LORENTIZIAN MOSSBAUER DATA
                C     AND PLOTES THE RESULTS
                C     IN THE FIRST PART OF THE PROGRAM THE FOLLOWING SYMBOLS ARE USED
                C     X(N), CHANNEL NUMBER IN FLOTTING POINT FORM
                C     Y(N), RAW MOSSBAUER DATA
                C     A(L), VALUE OF PARAMETERS
                C     ETA(N,L), DETERMINED BY VALUES OF X(N) AND A(L)
                C     SM(L,M), MATRIX FORMED BY SUMMING ETA*ETA OVER N
                C     SZ(N), DEVIATION OF Y(N) FROM COMPUTED VALUES
                C     UZ(L), SUM OVER N OF SZ*ETA
                C     DLTA(L)  CORRECTION TO A(L) TO IMPROVE THE FIT
0001                  COMMON Y2(410),Y(410),A(20),ALABL(54),NPLOT,NVEL,
                     1XZERO,VEL,IDX,NDATA,Y2M
0002                  DIMENSION X(410),SZ(410),
                     1UZ(20),DLTA(20),SM(20,20),B(7),C(7),ETA(410,7),RW(10)
0003                  EQUIVALENCE (UZ,DLTA), (SUM,ARAT,XLP), (XMIN,RMSEX,ELL),
                     1     (XMUL, RMSME)
0004                  DATA  PLUS/1H+/,STAR/1H*/,BLANK/1H /
                C   THE FIRST PART OF THE PROGRAM READS AND NORMALIZES THR DATA
0005                  NPLOT=0
0006                  READ (1,9) NSETS,IDX
0007            9     FORMAT (2I3)
0008                  DO 210 KP=1,NSETS
0009                  K=201
0010                  IF (IDX.LT.0) GO TO 87
0011                  K=0
0012                  READ(1,100) MAX,MIN,MPLOT
0013            100   FORMAT(3I4)
                C   MAX IS THE HIGHEST CHANNEL USED
                C   MIN IS THE LOWEST CHANNEL USED
                C   ARAC IS THERATIO OF ACTUAL TO EXPECTED RMS ERROR
0014                  NDAT=25
0015                  IF (IDX.NE.0) GO TO 50
0016                  NDAT = 2*NDAT
0017            50    CONTINUE
0018                  NDATA = 8*NDAT
0019                  READ (1,60) OV
0020            60    FORMAT (F4.0)
0021                  IEXP=6.0
0022            930   READ (1,931) (ALABL(I),I=1,36)
0023            931   FORMAT (18A4)
0024            87    READ (1,931) (ALABL(I),I=37,54)
0025            89    WRITE (3,90)
0026            90    FORMAT(1H1)
0027            935   WRITE (3,91)  (ALABL(I),I=1,54)
```

```
0028        91     FORMAT (1H ,18A4)
0029               FO=0.0
0030               READ (1,54) FO,PO,HO,RO
0031        54     FORMAT (4F10.6)
0032               DO 932 JK=1,NDATA
0033        932    Y(JK)=0.C
0034               DO 933 JK=1,NDAT
0035        9318   READ (1,934) (RW(J),J=1,8)
0036        9328   JKK=8*(JK-1)
0037        9338   DO 933 I=1,8

0038               IK=IABS(K-JKK-I)
0039        933    Y(IK)=RW(I)
0040        934    FORMAT (8(4X,F6.0))
            C CORRECT FOR COUNT OVERFLOW,NORMALIZE  Y
0041               MAX1=MAX-1
0042               DO 103 N=2,MAX1
0043               IF(Y(N)-1000.0)1031,1031,103
0044         1031  Y(N)=(Y(N-1)+Y(N+1))/2
0045          103  CONTINUE
0046               NUM=MAX-MIN+1
0047               TOTAL=0.0
0048               DO102 N=1,NUM
0049               M=N+MIN-1
0050               Y(N)=Y(M)
0051               X(N)=M
0052          102  TOTAL=TOTAL+Y(N)
0053               XNUM=NUM
0054               TOTAL=TOTAL/XNUM
0055               TOTAL=TOTAL+OV*(10.**IEXP)
0056               RMSEX=(1/SQRT(TOTAL))*0.6745
0057               DO104 N=1,NUM
0058               Y(N)=Y(N)+OV*(10.**IEXP)
0059               Y(N)=Y(N)/TOTAL
0060        104    Y(N)=(Y(N)-FO)/(1.-FO)
            C Y = NORMALIZED COUNTS, BACKGROUND CORRECTED
0061               IDX=-IDX
0062               IF (IABS(IDX).NE.2) GO TO 99
0063          30   DO  31 I=1,NUM
0064               E=I+MIN-1
0065               Z=PO/(1.0+((E-PO)/HO)**2)
0066               Y(I)=Y(I)+Z
0067          31   CONTINUE
0068               WRITE(3,33)
0069        33     FORMAT (35HBERYLLIUM-IRON IMPURITY SUBTRACTED)
0070               WRITE (3, 34) PO,HO,RO
0071        34     FORMAT(4X,15HPEAK POSITION =,F10.6,3X,11HHALFWIDTH =,F10.6,
                  13X,8HHEIGHT =,F10.6)
0072        99     CONTINUE
```

```
0073          READ(1,1000) XZERO,VEL,NVEL
0074     1000 FORMAT(2F10.6,I2)
        CLP IS THE TOTAL NUMBER OF PARAMETERS TOBE DETERMINED
0075          LP=6
0076          WRITE(3,105) MAX, MIN, NUM, TOTAL, RMSEX
0077      105 FORMAT(10X,3I10,F20.0,F20.6)
0078          READ(1,106)(A(L),L=1,LP)
0079      106 FORMAT (2F8.6)
0080          A(5)=2./A(5)
0081          ITER=0
        C THE NEXT PART OF THE PROGRAM IS TO COMPUTE ETA(N,L)
0082          DO108 N=1,NUM
0083          ETA(N,1)=1.0
0084      108 ETA(N,2)=(X(N)-100.5)**2
0085      107 DO 111 N=1,NUM
0086          C(1)=X(N)-A(6)+A(4)
0087          C(2)=X(N)-A(6)-A(4)
0088      109 B(1)=1./(1.+(A(5)*C(1))**2)

0089          B(2)=1./(1.+(A(5)*C(2))**2)
0090          ETA(N,3)=(B(1)+B(2))/2
0091          ETA(N,4)=(C(1)*B(1)*B(1)-C(2)*B(2)*B(2))/2
0092          ETA(N,5)=((B(1)*C(1))**2+(B(2)*C(2))**2)/2
0093      110 ETA(N,6)=(B(1)*B(1)*C(1)+B(2)*B(2)*C(2))/2
0094          ETA(N,3)=-ETA(N,3)
0095          ETA(N,4)=A(3)*2.*A(5)*ETA(N,4)
0096          ETA(N,5)=+2.*A(5)*A(3)*ETA(N,5)
0097          ETA(N,6)=-2.*A(3)*A(5)*A(5)*ETA(N,6)
0098          SZ(N)=A(1)+A(2)*ETA(N,2)+A(3)*ETA(N,3)
0099      111 SZ(N)=Y(N)-SZ(N)
        C COMPUTATION OF SZ(N)
        C     COMPUTATION OF MATRIX
0100          DO 114 L=1,LP
0101          DO 114 M=1,L
0102          SM(L,M)=0.0
0103          DO 113 N=1,NUM
0104      113 SM(L,M)=SM(L,M)+(ETA(N,L))*(ETA(N,M))
0105      114 SM(M,L)=SM(L,M)
0106          DO 8 N=1,10
0107          NTEST=ITER-2*N
0108          IF (NTEST) 6,7,8
0109      7   WRITE (3,5)
0110      5   FORMAT (1H1)
0111      6   GO TO 115
0112      8   CONTINUE
0113      115 CONTINUE
```

```
0114          WRITE(3,135)RMSEX
0115     135  FORMAT (//15X,21HEXPECTED RMS ERROR = ,F9.6/)
         C COMPUTATION OF UZ(L)
0116          DO 116 L=1,LP
0117          UZ(L)=0.0
0118          DO 116 N=1,NUM
0119     116  UZ(L)=UZ(L)+(SZ(N))*(ETA(N,L))
         C COMPUTATION OF RMS ERROR
0120          ITER=ITER+1
0121          SUM=0.0
0122          DO 119 N=1,NUM
0123     119  SUM=SUM+(SZ(N)**2)
0124          RMSME=SQRT(SUM/XNUM)
0125          WRITE(3,120)RMSME
0126     120  FORMAT (15X, 21H  ACTUAL RMS ERROR  = ,F9.6/)
0127          ARAT=RMSME/RMSEX
0128          WRITE(3,117)ARAT
0129     117  FORMAT (15X, 45H THE RATIO OF ACTUAL TO EXPECTED RMS ERROR =
             1     , F9.4/)
         C AT THIS POINT THE SUBROUTIN FOR INVERTING A MATRIX SHOULD BE CALLED
0130          CALL MATINV (SM,LP,UZ,1)
0131          DO 121 L=1,LP
0132     121  WRITE(3,122)L,DLTA(L),L,A(L)
0133     122  FORMAT(5X,5HDLTA( , I2, 5H ) = ,E10.3,25X,3H A(, I2,4H ) = ,F10.4)
0134          WRITE(3,160)
0135     160  FORMAT(/)
0136          XLP=LP
0137          DO 123 L=1,LP
0138          A(L)=A(L)+DLTA(L)

0139          RMSDE=RMSME*SQRT(SM(L,L)*XNUM/(XNUM-XLP))*0.6745
0140     123  WRITE(3,124)L, A(L),RMSDE
0141     124  FORMAT (5X19HTHE NEW VALUE OF A(,I2,5H ) IS, F10.4,10X,5H RMS ,
             1     E10.3  )
0142          WRITE(3,125)ITER
0143     125  FORMAT (//5X,22HTHIS IS THE END OF THE,I2,1X,10HITERATION.)
0144          IF (ITER-10) 107,126,126
0145     126  CONTINUE
0146          WRITE(3,134)
0147     134  FORMAT(1H1, 50X, 18H CALCULATED CURVE //)
         C CALCULATION OF THE FINAL CURVE
0148          WRITE(3,161)
0149     161  FORMAT( 9X,10HCHANNEL NO ,3X,17HEXPERIMENTAL DATA ,2X,
             1        16HLEAST SQUARE FIT ,5X,15HNORMALIZED DATA ,
             2        4X,16HNORMALIZED LSFIT , 5X, 11H DIFFERENCE  //)
0150          TOTAL=0.0
```

```
0151          DO 128 N=1,NUM
0152          SUM=A(1)+A(2)*ETA(N,2)
0153          ETA(N,2)=Y(N)/SUM
0154          ETA(N,4)=0.0
0155          C(1)=X(N)-A(6)+A(4)
0156          C(2)=X(N)-A(6)-A(4)
0157          B(1)=1./(1.+(A(5)*C(1))**2)
0158          B(2)=1./(1.+(A(5)*C(2))**2)
0159      127 ETA(N,4)=(B(1)+B(2))/2
0160          ETA(N,4)=SUM-A(3)*ETA(N,4)
0161          ETA(N,1)=ETA(N,4)/SUM
0162          DIFF=ETA(N,2)-ETA(N,1)
0163          M=N+MIN-1
0164          WRITE(3,129)M,Y(N),ETA(N,4),ETA(N,2),ETA(N,1),DIFF
0165      129 FORMAT (5X,I10, 5F19.5)
0166          TOTAL= TOTAL+DIFF
0167      128 CONTINUE
0168          A(5)=2./A(5)
0169          WRITE(3,133) A(5)
0170      133CFORMAT(//10X,30HTHE LINEWIDTH OF ALL LINES IS
             1  ,F7.2, 10H CHANNELS  /)
0171          WRITE(3,172)TOTAL
0172      172 FORMAT ( 9X, 30H THE SUM OF THE DEVIATIONS IS  , F8.5)
0173          PARB=A(1)+A(2)*((A(6)-100.5)*(A(6)-100.5)+A(4)*A(4))
0174          AREA=3.14159*A(5)*A(3)/2*PARB
0175          WRITE (3,175) AREA
0176      175 FORMAT(/10X,10HTOTAL AREA,F10.5)
0177          A(4)=A(4)*2.
0178          WRITE (3,181) A(3)
0179          WRITE (3,180) A(4)
0180          WRITE (3,182) A(6)
0181      180 FORMAT (1H0,10X,15HPEAK SEPARATION,F9.4)
0182      181 FORMAT (1H0,10X,15HRELATIVE HEIGHT,F9.6)
0183      182 FORMAT (1H0,10X,13HPEAK POSITION,F9.4)
0184          WRITE(3,174)
0185      174 FORMAT (1H1, 40X, 34H PLOT OF THE MOSSBAUER ABSORPTION  /  )
        C THIS SECTION PLOTS THE RESULTS OF THE LEAST SQUARE FIT
        C THE FIRST THING IS TO FIND XMIN
0186          XMIN=1.0
0187          DO 201 N=1, NUM
```

```
0188          Y(N)=ETA(N,2)
0189          Y2(N)=ETA(N,1)
0190          DO 201 L=1,2
0191          IF (ETA(N,L)-XMIN) 200, 200, 201
0192      200 XMIN=ETA(N,L)
0193      201 CONTINUE
0194          Y2M=XMIN
0195          IF(MPLOT)1201,1201,300
0196     1201 XMUL=95./(1.-XMIN)
0197          DO 202 L=1, 10
0198          ELL=L
0199      202 A(L)=(ELL-1.)*10.
        C THE NEXT STEP PRINTS THE SCALE
0200          WRITE(3,203)(A(L),L=1,10)
0201      203 FORMAT (8H CHANNEL ,4X, 10(F5.1, 5X) , 7HCHANNEL     )
        C THE PLOT IS SCALED BETWEEN 0 AND 95
0202          DO 205 N=1,NUM
0203          ETA(N,1) = (1.0-ETA(N,1))*XMUL
0204          ETA(N,2) = (1.0-ETA(N,2))*XMUL
0205          IF(ETA(N,2)+4.0) 204, 204, 205
0206      204 ETA(N,2)=-4.0
0207      205 CONTINUE
0208          DO 15 L=1,NUM
0209          DO 10 N=1,101
0210       10 ETA(N,3)=BLANK
0211          DO 14 JX=1,2
0212          ETA(L,JX)=ETA(L,JX)+5.5
0213          N1=ETA(L,JX)
0214          GO TO (13, 12), JX
0215       12 ETA(N1,3)=PLUS
0216          GO TO 14
0217       13 ETA(N1,3)=STAR
0218       14 CONTINUE
0219          NPI=L+MIN-1
0220       15 WRITE(3,16)NPI,(ETA(N,3),N=1,101),NPI
0221       16 FORMAT (I8,2X,50A1, 51A1, I5)
        C THE NEXT STEP PRINTS THE SCALE AGAIN
0222          WRITE(3,203)(A(L),L=1,10)
0223          GO TO 210
0224      300 CALL DRAW
0225      210 CONTINUE
0226      212 IF(NPLOT.LE.0) GO TO 215
0227          CALL LSTPLT
0228      215 CALL EXIT
0229          END
```

```
0001              SUBROUTINE DRAW
0002              COMMON Y2(410),Y(410),A(20),ALABL(54),NPLOT,NVEL,
                 1XZERO,VEL,IDX,NDATA,Y2M
0003              DIMENSION YA(410),YB(410),XD(410),YD(410)
0004        950   IF (NPLOT.GT.0) GO TO 951
0005              CALL PENPOS (!CANNER,J.P.!,11,1)
0006          951 CALL NEWPLT (10.0,2.0,10.5)
0007              DATA=NDATA
0008              CALL ORIGIN (DATA,0.0)
0009              CALL YSCALE (0.0,1.20,6.0)
0010              CALL YAXIS (0.1)
0011              IF (NVEL.LE.0) GO TO 961
0012              XMIN=-XZERO*VEL
0013              XMAX=(DATA-XZERO)*VEL
0014              DIN=DATA/200.0
0015              XOIN=2.0+0.04*XZERO/DIN
0016              CALL NEWPLT (XOIN,8.0,10.5)
0017              CALL ORIGIN (0.0,1.2)
0018              CALL XSCALE (XMIN,XMAX,8.0)
0019              CALL XAXIS (0.5)
0020              CALL YSCALE (0.0,1.20,6.0)
0021              IF (NVEL.EQ.1) GO TO 957
0022              DO 956 J=1,2
0023              RAM=A(3)/2.0
0024              B=J
0025              POS=A(6)+(B-1.5)*A(4)
0026              BETA=A(5)/2.0
0027              N3=POS-2.*BETA
0028              N4=POS+2.*BETA
0029              N5=N4-N3+1
0030              K=0
0031              DO 952 I=1,N5
0032              II=I-K
0033              C=N3+I-1
0034              XD(II)=(C-XZERO)*VEL
0035              YD(II)=1.05-RAM/((1.0+((C-POS)/BETA)**2)*(1.0-Y2M))
0036              IF ((XMIN-XD(II)).GT.0) K=K+1
0037              IF ((XMAX-XD(II)).LT.0) GO TO 953
```

```
0046          958 IF ((J-I).LT.0) GO TO 960
0047              X=I
0048              XIN=XSTOIN(X)-0.14
0049              CALL NUM (XIN,-0.20,0.105,X,0.0,-1)
0050              I=I+1
0051              GO TO 958
0052          960 CONTINUE
0053              XTIN=5.0-XOIN
0054              CALL SYM (XTIN,0.10,0.14,'VELOCITY (MM/SEC)',0.0,17)
0055      961     CALL NEWPLT (2.0,2.0,10.5)

0056              CALL ORIGIN (1.0,0.0)
0057              CALL YSCALE (0.0,1.20,6.0)
0058              CALL YAXIS (0.1)
0059              DO 962 L=1,13
0060              YC=(L-1)*0.5-0.07
0061              YON=0.0+(L-1)*0.1
0062              CALL NUM (-0.50,YC,0.105,YON,0.0,1)
0063      962     CONTINUE
0064              CALL SYM (-0.7,2.0,0.14,'INTENSITY',90.0,9)
0065              DO 955 I=1,NDATA
0066              YA(I)=(Y2(I)-Y2M)/(1-Y2M)+0.05
0067          955 YB(I)=(Y(I)-Y2M)/(1-Y2M)+0.05
0068      965     CALL TSCALE (1.0,DATA,8.0)
0069              CALL TAXIS (10.0)
0070              CALL TPLT (YA,NDATA,1,-1)
0071              CALL TPLT (YB,NDATA,2,3)
0072              DATON=DATA/20.0
0073              DO 968 L=1,21
0074              TD=(L-1)*0.4-0.14
0075              TON=(L-1)*DATON
0076              IF (IDX.LE.0) GO TO 967
0077              TON=400.0-TON
0078      967     CONTINUE
0079              CALL NUM (TD,-0.18,0.105,TON,0.0,-1)
0080          968 CONTINUE
0081          969 CALL SYM (2.75,-0.4,0.14,'CHANNEL-NUMBER',0.0,14)
0082          970 CONTINUE
0083              CALL SYM (1.0,6.3,0.14,ALABL,0.0,48)
0084              CALL ENDPLT
0085              NPLOT=NPLOT+1
0086              RETURN
0087              END
```

```
0001          SUBROUTINE MATINV (A,N,B,M)
0002          DIMENSION A(20,20),B(20,1),INDEX(20,3)
0003          COMMON DETER
0004          EQUIVALENCE (IROW,JROW), (ICOLUM,JCOLUM), (AMAX,T,SWAP)
0005       10 DETER=1.0
0006       15 DO 20 J=1,N
0007       20 INDEX(J,3)=0
0008       30 DO 550 I=1,N
         C
         C    SEARCH FOR PIVOT ELEMENT
         C
0009       40 AMAX=0.
0010       45 DO 105 J=1,N
0011          IF (INDEX(J,3)-1) 60,105,60
0012       60 DO 100 K=1,N
0013          IF (INDEX(K,3)-1) 80,100,740
0014       80 IF(AMAX-ABS(A(J,K))) 85,100,100
0015       85 IROW=J
0016       90 ICOLUM=K
0017          AMAX=ABS(A(J,K))
0018      100 CONTINUE
0019      105 CONTINUE
0020          INDEX(ICOLUM,3)=INDEX(ICOLUM,3)+1
0021      260 INDEX(I,1)=IROW
0022      270 INDEX(I,2)=ICOLUM
         C
         C     INTERCHANGE ROW TO PUT PIVOT ELEM.IN DIAG.
         C
0023      130 IF(IROW-ICOLUM) 140,310,140
0024      140 DETER=-DETER
0025      150 DO 200 L=1,N
0026      160 SWAP=A(IROW,L)
0027      170 A(IROW,L)=A(ICOLUM,L)
0028      200 A(ICOLUM,L)=SWAP
0029          IF(M) 310,310,210
0030      210 DO 250 L=1,M
0031      220 SWAP=B(IROW,L)
0032      230 B(IROW,L)=B(ICOLUM,L)
0033      250 B(ICOLUM,L)=SWAP
         C
```

```
C       DIVIDE PIVOT ROW BY PIVOT ELEMENT
C
  310 PIVOT=A(ICOLUM,ICOLUM)
      DETER=DETER*PIVOT
  330 A(ICOLUM,ICOLUM)=1.0
  340 DO 350 L=1,N
  350 A(ICOLUM,L)=A(ICOLUM,L)/PIVOT
  355 IF (M) 380,380,360
  360 DO 370 L=1,M
  370 B(ICOLUM,L)=B(ICOLUM,L)/PIVOT
C
C       REDUCE NON PIVOTS ROWS'
C
  380 DO 550 L1=1,N
  390 IF(L1-ICOLUM) 400,550,400
  400 T=A(L1,ICOLUM)

  420 A(L1,ICOLUM)=0.
  430 DO 450 L=1,N
  450 A(L1,L)=A(L1,L)-A(ICOLUM,L)*T
  455 IF (M) 550,550,460
  460 DO 500 L=1,M
  500 B(L1,L)=B(L1,L)-B(ICOLUM,L)*T
  550 CONTINUE
C
C       INTERCHANGE COLUMNS
C
  600 DO 710 I=1,N
  610 L=N+1-I
  620 IF(INDEX(L,1)-INDEX(L,2)) 630,710,630
  630 JROW=INDEX(L,1)
  640 JCOLUM=INDEX(L,2)
  650 DO 705 K=1,N
  660 SWAP=A(K,JROW)
  670 A(K,JROW)=A(K,JCOLUM)
  700 A(K,JCOLUM)=SWAP
  705 CONTINUE
  710 CONTINUE
  740 RETURN
      END
```

APPENDIX III.

ABSORBER THICKNESS CALCULATION AND MEASUREMENT

The absorber thickness was optimized to give the maximum signal to noise ratio. The calculation was due to Banks,[139] with the result for solid solutions with $BiFeO_3$:

$$m_T = \frac{1}{\mu_4 k_4 c_1} \ln \left(1 + \frac{2\,\mu_4 k_4 c_1}{\mu_1 c_1 + \sum_j \mu_j c_j}\right) \qquad \text{(A-III-1)}$$

where m_T is the total mass of the sample (gm/cm^2),

c_1 is the concentration of $BiFeO_3$,

c_j is the concentration of the jth component,

μ_1 is the absorption coefficient for $BiFeO_3$ (cm^2/gm),

μ_j is the absorption coefficient for j^{th} component,

μ_4 is the resonance absorption coefficient for $BiFeO_3$,

k_4 is the concentration of Fe^{57} in $BiFeO_3$.

Using 80% enriched iron, values of m_T are approximately 20 mg/cm^2, corresponding to about 0.14 mg/cm^2 of Fe^{57}. The mass absorption coefficients and calculated values of m_T are included in table X.

The measurement of sample thickness was necessary for accurate determination of the f factor. The measurements were difficult to make mechanically, due to the geometry of the sample holder, and the difficulty of obtaining an even layer of sample on the Be foil. The samples were weighed before being placed in the sample holder, but estimated thicknesses failed to agree with gamma ray absorption

TABLE X.

MASS ABSORPTION FACTORS AND OPTIMUM THICKNESSES OF SAMPLES

SAMPLE	ATOMIC MASS	MASS ABSORPTION FACTOR $(\frac{cm^2}{gm})$	PERCENT IRON 57 IN IRON	OPTIMUM MASS $(\frac{gm}{cm^2})$	USED MASS $(\frac{gm}{cm^2})$	MEASURED MASS $(\frac{gm}{cm^2})$	$n\sigma_o$
Natural Iron	55.85	69.0	2.16	27.7	18.5	16.3	9.57
$BiFeO_3$	312.85	102.8	2.16 90.0	19.3 15.9	-- --	-- --	-- --
$PbZrO_3$	346.43	86.9	--	--	--	--	--
$PbTiO_3$	303.11	97.3	--	--	--	--	--
95% $PbZrO_3$ 5% $BiFeO_3$	344.75	87.7	81.5	22.5	34.1	8.5	1.49
95%$PbZr_{.8}Ti_{.2}O_3$ 5%$BiFeO_3$	336.52	89.6	90.0	22.0	25.3	8.4	1.61
95%$PbZr_{.7}Ti_{.3}O_3$ 5%$BiFeO_3$	332.40	90.6	90.0	21.8	39.5	4.5	0.88

measurements. The geometry of the furnace restricted the usable area of the sample holder to about 1/2 inch in diameter on a 3/4 inch diameter disc, reducing the area by a factor of two. The thickness was finally measured by comparing gamma-ray count rates for an .001 inch thick iron foil and for the sample. Using the calculated absorption factors,[152] the thickness of the sample was obtained from the equation:

$$\frac{I_{sample}}{I_{iron}} = \frac{\exp(-\mu_{sample}\, t)}{\exp(-\mu_{iron}\, t)} \qquad \text{(A-III-2)}$$

where I is the measured count rate,

μ is the mass absorption coefficient (cm^2/gm),

t is the thickness (gm/cm^2).

The ratio was used to eliminate the effects of the background and absorption due to the Be foils and counter tube. The thicknesses of the samples were found to correspond to less than half that expected from the amount of sample used. This was not entirely unexpected, since some of the sample seemed to pile up at the edges of the sample holder and even seep under the retaining ring.

The factor $n\sigma_o$, is the number of Fe^{57} nuclei per unit cross section of resonance absorption. It is calculated from the thickness using the following expression:

$$n\sigma_o = t\,\frac{c_{Fe^{57}} N_o}{A_{Fe^{57}}}\,\sigma_o \qquad \text{(A-III-3)}$$

where n is the number of Fe^{57} nuclei per cm^2,

σ_o is the resonance cross section for Fe^{57} ($2.26 \times 10^{-18} cm^2$),

t is the measured thickness (gm/cm^2),

$c_{Fe^{57}}$ is the concentration of Fe^{57} in the sample,

N_o is Avogadro's number (atoms or nuclei per mole),

$A_{Fe^{57}}$ is the atomic mass of Fe^{57} (gm/mole).

The result of these measurements and calculations are summarized in table X. Since the accuracy of the f determinations and the Debye temperature depend on these measurements, the results for the iron foil are also calculated and are found to correspond fairly well with expected results.

APPENDIX IV.

CALCULATION OF f FACTOR AND DEBYE TEMPERATURE

From equation 36 or 37, the value of f can be determined quite easily using the experimental data and the sample thickness. An iterative procedure, using Figure 14, starts out with the thickness correction factor, G or F, equal to one. A value of f is calculated from which a new G or F can be determined. This is repeated until f is obtained to sufficient precision. Since the graphs are quite hard to interpolate from, the precision is limited to the second decimal place in f.

The Debye temperature can be estimated from figure 1. Two methods of calculating θ_D more exactly are available. The equation $f = e^{-2W}$ relates θ and f thru a function $\Phi(\frac{\theta}{T})$. This function is numerically tabulated[7] since it is not easily solvable. A self-consistent solution for θ_D requires iteration using the equation:

$$x = \frac{1}{8C}\,[1+64CZ(x)]^{\frac{1}{2}} \qquad \text{(A-IV-1)}$$

where: $x = \frac{\theta_D}{T}$

$$C = -\frac{Mc^2kT}{3E_o^2}\,\ln f$$

$$Z(x) = \frac{1}{x}\Phi(x) = \frac{1}{x}\int_0^x \frac{t\,dt}{e^t-1}$$

and E_o is the γ-ray energy,

M is the mass of the emitting atom,

c is the velocity of light,

k is Boltzmann's constant,

f is the Mossbauer fraction,

T is temperature in degrees Kelvin.

The calculation proceeds with a guess for Z(x) from which x is calculated. This x determines a new value of Z(x). This is repeated until x and Z(x) are consistent to the desired precision.

The other method derived by Taylor and Craig[138] makes use of the dependence of f on $\langle x^2 \rangle$ and the second order Doppler shift $(\frac{\delta v}{c})$ on $\langle v^2 \rangle$ of the atom. The result is given in eqn. 38. They used the ratio of log $f/(\frac{\delta v}{c})$ to eliminate the troublesome integral $\Phi(x)$ and to give the Debye temperature directly. The determination of the isomer shift-temperature slope can be complicated by the effects of a nearby phase transition. The contribution of anharmonic effects to the f factor is not known, so that the Debye-Waller factor may be unsatisfactory in determining θ_D from f. The second method eliminates the need of knowing the anharmonic contribution to the Mossbauer effect, by dividing out the effect present in both f and $\frac{\delta v}{c}$. This method gives Debye temperatures consistent with specific heat measurements in the case of some diatomic alloys.[138] The anharmonic effects in our samples are apparently small, since the Debye temperatures differ by about 20°K from the straight harmonic approximation.

The effect of linewidth on f is another problem in

these experiments. The linewidths are 2.5 to 4 times larger than the natural linewidths, so that the cause for broadening must be considered. The factor of 4 can be reduced to 3, if four peaks are fitted to the antiferroelectric sample. The broadening is not strongly dependent on temperature even near phase transitions, so that it is probably not due to long relaxation times in the lattice. It was suggested by Bell[101] and Stoneham[102] that random distribution of differently charged atoms caused an inhomogeneous broad peak composed of many peaks, having natural linewidth, positioned close together. Assuming this to be true, f has been calculated using the linewidth obtained for iron foil. The increased value of f gave higher Debye temperatures. The values obtained are more reasonable in terms of the fairly rigid perovskite lattice.

APPENDIX V.

ELECTRIC FIELD GRADIENT APPROXIMATION FOR $PbZrO_3$.

A rough estimate of the electric field gradient in $PbZrO_3$ has been obtained using the structural data of Jona, et al.[76] and the internal electric field data of Lyubimov, et al.[125] A large polarization of about 25μC/cm² has been estimated by Jona, et al.[76] to fit the structure (see figs. 8 and 43). The displacements in the ab plane are anti-parallel giving the antiferroelectric effect. The polarization along z is apparently strongly bound so that no reversal can result at room temperature.

An examination of the electric fields calculated assuming the spontaneous polarization was zero gave the same conclusion. In the ab plane, the fields have alternating signs and are smaller than the fields along the c direction.

A linear chain model was used to estimate the electric field gradient for the two zirconium sites. The chain is actually puckered at angles of 10°. The chain is diagramed in fig. 44.

The electric field gradient was approximated by a finite differences equation for each ion in the lattice by:

$$\frac{\partial E}{\partial z} \simeq \frac{E(z+\Delta z) - E(z)}{\Delta z} \qquad \text{(A-V-1)}$$

where: E(z) is the electric field at z, directed along z,

Δz is the distance between ions.

The resulting sum equations are:

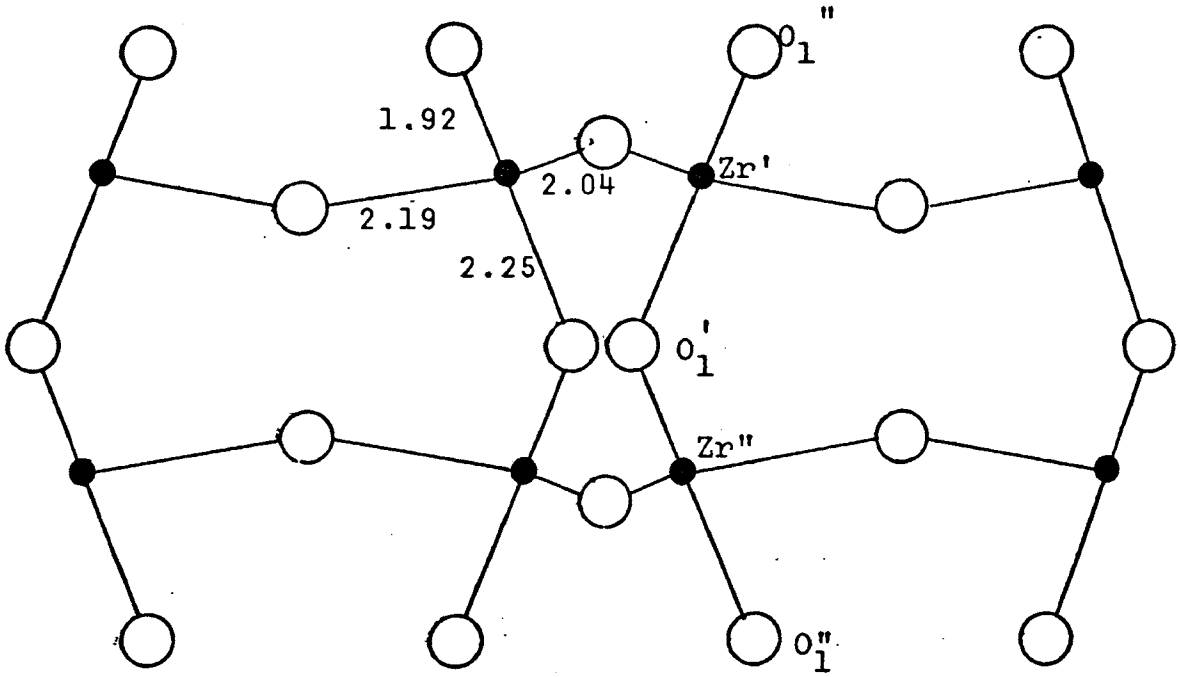

FIG. 43. Representation of the oxygen and zirconium displacements along the c-axis.

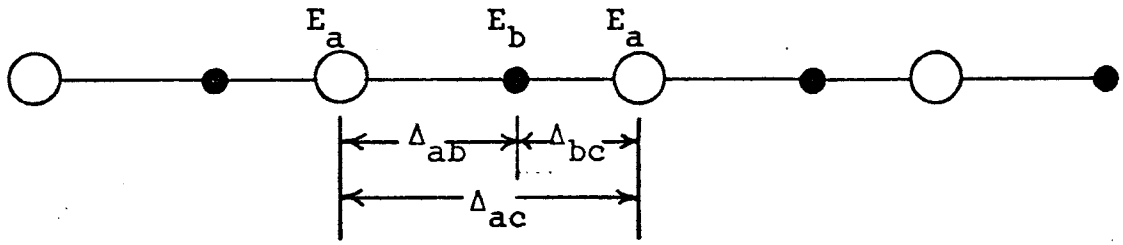

FIG. 44. Linear chain model used to calculate the electric field gradient due to the polarization of the zirconium atoms in the lattice.

$$\frac{\partial E'}{\partial z} = \sum_{n=-\ell}^{\ell} \frac{E_c - E_b}{\Delta_{bc} + 2n\Delta_{ac}} + \frac{E_a - E_b}{\Delta_{bc} + (2n-1)\Delta_{ac}} \qquad \text{(A-V-2)}$$

and

$$\frac{\partial E''}{\partial z} = \sum_{n=-\ell}^{\ell} \frac{E_a - E_b}{\Delta_{bc} + 2n\Delta_{ac}} + \frac{E_c - E_b}{\Delta_{bc} + (2n-1)\Delta_{ac}} \qquad \text{(A-V-3)}$$

where ℓ is the number of lattices in the sum.

The values of $E_a = E_{o.'}$

$E_b = E_{Zr'}$ or $E_{Zr''}$

$E_c = E_{o.''}$

$\Delta_{bc} = 1.92\text{Å}$

$\Delta_{ac} = 2.25\text{Å}$

$\Delta_{ab} = 4.17\text{Å}$

gave values of

$$\frac{\partial E'}{\partial z} = .367 \times 10^{16} \frac{v}{cm^2} \quad \text{and}$$

$$\frac{\partial E''}{\partial z} = -1.087 \times 10^{16} \frac{v}{cm^2}.$$

The effect of the opposite signs was to invert the energy levels of the excited state. The relative splitting was the ratio of the two electric field gradients. This ratio was $\frac{V_{zz''}}{V_{zz'}} = \frac{1.087}{.367} = 2.97$ or nearly three for $PbZrO_3$.

This ratio was used in modifying the LORLSF program to fit four Lorentzians at the positions $x_o \pm \Delta$, $x_o \pm 3\Delta$. The Lorentzians are constrained to have the same height and linewidth. A good fit was obtained for the $PbZrO_3$ data

TABLE XI.

LATTICE PARAMETERS AND ELECTRIC FIELDS FOR $PbZrO_3$.

ATOM	$\frac{x}{a}$	$\frac{y}{b}$	$\frac{z}{c}$	Δr (Å)	E_x	E_y	E_z	$\lvert E \rvert$
					Field times 10^8 volts/cm.			
Pb'	.706	.127	.000	.26Å	-2.091	-2.566	-3.046	4.498
Pb"	.706	.127	.500	.26	-4.957	5.392	-4.728	8.718
Zr'	.243	.124	.250	.04	1.059	-4.055	11.180	12.227
Zr"	.243	.124	.750	.04	-0.137	2.060	9.533	9.754
O_1'	.270	.150	.980	.35	-1.427	1.320	5.499	5.794
O_1"	.270	.100	.480	.35	-3.452	-4.120	7.571	9.285
O_2'	.040	.270	.300	.53	-5.135	-3.066	-4.604	7.548
O_2"	.040	.270	.750	.34	-1.112	-0.275	0.901	1.458
O_3'	.000	.500	.250	.00	0.00	0.00	2.515	2.515
O_3"	.000	.500	.800	.41	0.00	0.00	-3.215	3.215
O_4'	.000	.000	.250	.00	0.00	0.00	0.722	0.722
O_4"	.000	.000	.800	.41	0.00	0.00	-0.495	0.495

a = 5.884 Å b= 11.768 Å c = 8.220 Å

that required "beryllium" correction using $\Delta = 7.5$ channels. Attempts with $\Delta = 5.5$ and 10. gave larger errors. The data for $PbZrO_3$ which did not need the "beryllium" correction were definitely asymmetric. No attempt has been made to fit this with more than two peaks. The modification to LORLSF to fit unequal heights introduces at least one more parameter and convergence is less sure.

VITA

James Philip Canner was born in St. Paul, Minnesota on April 19, 1941. He was educated in the elementary and secondary schools of St. Paul, graduating from Monroe High School in 1959. He received a B.S. in Physics from the University of Minnesota in June of 1963, and a M.S. in Physics from the University of Missouri - Rolla in June of 1965. He had a teaching assistantship for one year, a National Aeronautics and Space Administration traineeship for three years, and a research fellowship sponsored by the Atomic Energy Commission for two years.